

AFRL-VA-WP-TR-2006-3205

**CRACK GROWTH AND STRESS
INTENSITY PREDICTION
TECHNIQUES**

**Delivery Order 0027-1: Mixed Mode Failure
Criteria**



**Professor Michael A. Sutton
Professor Xiaomin Deng
Dr. Anthony Reynolds**

**The University of South Carolina
Department of Mechanical Engineering
Columbia, SC 29208**

MARCH 2006

Final Report for 01 October 2000 – 31 December 2004

Approved for public release; distribution is unlimited.

STINFO COPY

**AIR VEHICLES DIRECTORATE
AIR FORCE MATERIEL COMMAND
AIR FORCE RESEARCH LABORATORY
WRIGHT-PATTERSON AIR FORCE BASE, OH 45433-7542**

NOTICE AND SIGNATURE PAGE

Using Government drawings, specifications, or other data included in this document for any purpose other than Government procurement does not in any way obligate the U.S. Government. The fact that the Government formulated or supplied the drawings, specifications, or other data does not license the holder or any other person or corporation; or convey any rights or permission to manufacture, use, or sell any patented invention that may relate to them.

This report was cleared for public release by the Air Force Research Laboratory Wright Site (AFRL/WS) Public Affairs Office and is available to the general public, including foreign nationals.

Copies may be obtained from the Defense Technical Information Center (DTIC)
(<http://www.dtic.mil>).

AFRL-VA-WP-TR-2006-3205 HAS BEEN REVIEWED AND IS APPROVED FOR PUBLICATION IN ACCORDANCE WITH ASSIGNED DISTRIBUTION STATEMENT.

*/Signature/

James A. Harter
Program Manager
Analytical Structural Mechanics Branch

//Signature//

Kristina Langer, Ph.D.
Branch Chief
Analytical Structural Mechanics Branch

//Signature//

David M. Pratt, Ph.D.
Technical Advisor
Structures Division
Air Vehicles Directorate

This report is published in the interest of scientific and technical information exchange, and its publication does not constitute the Government's approval or disapproval of its ideas or findings.

*Disseminated copies will show “//signature//” stamped or typed above the signature blocks.

REPORT DOCUMENTATION PAGE					Form Approved OMB No. 0704-0188	
<p>The public reporting burden for this collection of information is estimated to average 1 hour per response, including the time for reviewing instructions, searching existing data sources, gathering and maintaining the data needed, and completing and reviewing the collection of information. Send comments regarding this burden estimate or any other aspect of this collection of information, including suggestions for reducing this burden, to Department of Defense, Washington Headquarters Services, Directorate for Information Operations and Reports (0704-0188), 1215 Jefferson Davis Highway, Suite 1204, Arlington, VA 22202-4302. Respondents should be aware that notwithstanding any other provision of law, no person shall be subject to any penalty for failing to comply with a collection of information if it does not display a currently valid OMB control number. PLEASE DO NOT RETURN YOUR FORM TO THE ABOVE ADDRESS.</p>						
1. REPORT DATE (DD-MM-YY) March 2006		2. REPORT TYPE Final		3. DATES COVERED (From - To) 10/01/2000– 12/31/2004		
4. TITLE AND SUBTITLE CRACK GROWTH AND STRESS INTENSITY PREDICTION TECHNIQUES Delivery Order 0027-1: Mixed Mode Failure Criteria				5a. CONTRACT NUMBER F33615-98-D-3210-0027		
				5b. GRANT NUMBER		
				5c. PROGRAM ELEMENT NUMBER 0602201		
6. AUTHOR(S) Professor Michael A. Sutton Professor Xiaomin Deng Dr. Anthony Reynolds				5d. PROJECT NUMBER A02P		
				5e. TASK NUMBER		
				5f. WORK UNIT NUMBER OI		
7. PERFORMING ORGANIZATION NAME(S) AND ADDRESS(ES) The University of South Carolina Department of Mechanical Engineering Columbia, SC 29208				8. PERFORMING ORGANIZATION REPORT NUMBER		
9. SPONSORING/MONITORING AGENCY NAME(S) AND ADDRESS(ES) Air Vehicles Directorate Air Force Research Laboratory Air Force Materiel Command Wright-Patterson Air Force Base, OH 45433-7542				10. SPONSORING/MONITORING AGENCY ACRONYM(S) AFRL-VA-WP		
				11. SPONSORING/MONITORING AGENCY REPORT NUMBER(S) AFRL-VA-WP-TR-2006-3205		
12. DISTRIBUTION/AVAILABILITY STATEMENT Approved for public release; distribution is unlimited.						
13. SUPPLEMENTARY NOTES Report contains color. PAO Case Number: AFRL/WS 06-2188, 08 Sep 2006.						
14. ABSTRACT The challenges of designing modern aircraft continue to drive the development of more advanced analytical tools; often these more advanced analytical tools themselves require development of other enabling technologies such as powerful computers and associated software. The primary historical objective of this project was to develop the theoretical foundation for the development of a continuum-based, general stable crack extension criterion in ductile materials.						
15. SUBJECT TERMS mixed mode failure criteria, automatic remeshing, Arcan test specimen, CRACK3D						
16. SECURITY CLASSIFICATION OF:			17. LIMITATION OF ABSTRACT: SAR	18. NUMBER OF PAGES 130	19a. NAME OF RESPONSIBLE PERSON (Monitor) James A. Harter	
a. REPORT Unclassified	b. ABSTRACT Unclassified	c. THIS PAGE Unclassified			19b. TELEPHONE NUMBER (Include Area Code) N/A	

TABLE OF CONTENTS

LIST OF FIGURES.....	v
EXECUTIVE SUMMARY.....	1
I. INTRODUCTION.....	3
II. THEORETICAL DEVELOPMENTS.....	5
II.1.1 Background.....	5
II.1.2 Numerical Predictions for Crack-Tip Fields.....	6
II.1.3 Finite Element Models	8
II.1.4 Angular Variation of L^p and A_m	10
II.1.5 Radial variations along local mode I and mode II directions	11
II.1.6 Relationship between A_{ij} and A_m	15
II.1.7. The A_m -Family of Mixed Mode Crack Tip Fields	15
II.1.8. Concluding Remarks	17
II.2. THE BASIS OF COD FRACTURE CRITERIA FOR MIXED MODE I/II CRACK INITIATION AND GROWTH IN THIN SHEET MATERIALS [40]	18
II.2.1 Characteristic Crack Tip Parameters	18
II.2.2 Plane stress mixed mode I/II crack tip fields characterized by a characteristic length and stress triaxility parameter.....	18
II.2.3. Finite Element Studies	19
II.2.4 Radial Variations along Local Mode I and Mode II Directions.....	20
II.2.5 Relationship between A_{ij} and A_m	21
II.2.6 Implication for Development of Stable Tearing Criterion.....	22
II.2.6 Concluding Remarks	23
II.3. Basic studies of ductile failure processes and implications for fracture prediction	23
II.3.1. Background.....	23
II.3.2 A methodology for failure initiation study	25
II.3.3. A unit-cell model and numerical results	26
II.3.4 Concluding Remarks	30
II.4 Stress and Deformation fields Comparison between Flat and Slant Cracks under Remote Mode I Loading	31
II.4.1. Background.....	31
II.4.2. Mesh design for Arcan specimen and test fixture	32
II.4.3 Definition of Crack Opening Displacement	34
II.4.4 Results.....	35
II.4.5 Concluding Remarks	35
III. SIMULATION ALGORITHM DEVELOPMENT FOR THREE-DIMENSIONAL FRACTURE PREDICTIONS ALONG GENERAL FRACTURE SURFACES.....	36
III.1 General remarks	36
III.2 General Structure and Capabilities of CRACK3D	37
III.3 Data transfer between meshes after crack growth.....	37
III.4 Re-mesh for the 3D crack growth process	39
III.4.1 Local region re-mesh	39
III.4.2 General methods developed in our study	41
III.5 Re-meshing Process.....	43

III.6	Optimization of Mesh in Three-Dimensional Domain after Re-meshing.....	45
III.6.1	3-D surface mesh optimization	46
III.7	Recent Enhancements in CRACK3D Simulation Code.....	49
IV.	Experimental Studies.....	50
IV.1	Experimental Study of Crack Growth in Thin Sheet Material under Tension-Torsion Loading.....	50
IV.1.1	Background.....	50
IV.1.2	Specimen Configuration and Test Procedure	50
IV.1.3	Fracture Surface Measurements	52
IV.1.4	COD Measurements	53
IV.1.5	Crack Tunneling Measurements	53
IV.1.6	Concluding Remarks	54
IV.2	Small specimen tests for void growth measurements	55
IV.2.1	Notched cylindrical specimen tests	56
IV.2.2	Development of a shear specimen	57
V	Summary.....	57
VI.	REFERENCES	59
VII.	Appendix - List of Project-based Publications	65

LIST OF FIGURES

Figure 1: Crack-growth paths in Arcan specimens for various loading angles	69
Figure 2: (a) Schematic representation for L^p definition; (b) Mixed mode I/II crack tip plastic zone shape defined by $\sigma_e = \xi \sigma_0$; (c) A normalized mixed mode I/II crack tip plastic zone shape in Figure 2b.....	70
Figure 3: The hardening rules for AL-2024T3 and power-laws, $n=10$ and $n=3$	71
Figure 4: Finite element mesh for small scale yielding (SSY) model.....	71
Figure 5: Typical geometry and finite element meshes, (a) TPB, $c/w=0.5$, and (b) TB, $\beta=30^\circ$	72
Figure 6: Angular variations of L^p/R_K , von-Mises stress σ_e/σ_0 and shear stress $\sigma_{r\theta}/\sigma_0$ at $r/R_K=0.0865$, SSY model, (a) $T/\sigma_0=0$, $\chi=0^\circ$, (b) $T/\sigma_0=0$, $\chi=36.9^\circ$, (c) $T/\sigma_0=0$, $\chi=90^\circ$, (d) $T/\sigma_0=0.47$, $\chi=36.9^\circ$, and (e) $T/\sigma_0=-0.47$, $\chi=36.9^\circ$	73
Figure 7: L_{II}^p/L_I^p for SSY model, $n=10$	74
Figure 8: Angular variations of A_m , normal stresses σ_{rr}/σ_0 and $\sigma_{\theta\theta}/\sigma_0$ at $r/R_K=0.0865$, SSY model, (a) $T/\sigma_0=0$, $\chi=0^\circ$, (b) $T/\sigma_0=0$, $\chi=36.9^\circ$, (c) $T/\sigma_0=0$, $\chi=90^\circ$, (d) $T/\sigma_0=0.47$, $\chi=36.9^\circ$, and (e) $T/\sigma_0=-0.47$, $\chi=36.9^\circ$	75
Figure 9: Contained and uncontained yielding shapes of (a) TPB specimens, $c/w=0.5$ and (b) TB specimen, $\beta=30^\circ$	76
Figure 10: Angular variations of L^p/R_K , effective stress σ_e/σ_0 and shear stress $\sigma_{r\theta}/\sigma_0$ for (a) TB specimen, $\beta=30^\circ$, and (b) TPB specimens, $c/w=0.5$	76
Figure 11: Angular variations of A_m and normal stresses (σ_{rr}/σ_0 and $\sigma_{\theta\theta}/\sigma_0$) for (a) TB specimen, $\beta=30^\circ$, and (b) TPB specimens, $c/w=0.5$	77
Figure 12: The variation of $\Sigma_e = \sigma_e/\sigma_0$ with normalized distance, r/L^p , in (a) mode I and (b) mode II directions, respectively, for SSY model, power law material ($n=10$).	78
Figure 13: The variation of (a) $\Sigma_{rr} = \sigma_{rr}/A_{rr}\sigma_0$, (b) $\Sigma_{\theta\theta} = \sigma_{\theta\theta}/A_{\theta\theta}\sigma_0$ and (c) $\Sigma_m = \sigma_m/A_m\sigma_e$ with normalized distance, r/L^p , in mode I direction, respectively, for SSY model and power law material ($n=10$).	79
Figure 14: The variation of (a) $\Sigma_{rr} = \sigma_{rr}/A_{rr}\sigma_0$, (b) $\Sigma_{\theta\theta} = \sigma_{\theta\theta}/A_{\theta\theta}\sigma_0$, (c) $\Sigma_{r\theta} = \sigma_{r\theta}/A_{r\theta}\sigma_0$ and (c) $\Sigma_m = \sigma_m/A_m\sigma_e$ with normalized distance, r/L^p , in mode II direction, respectively, for SSY model, power law material ($n=10$).	80
Figure 15: The variation of $\Sigma_e = \sigma_e/\sigma_0$ with normalized distance, r/L^p , in (a) mode I and (b) mode II directions, respectively, for Al-2024T3 TB and TPB specimens	81
Figure 16: The Variation of (a) $\Sigma_{rr} = \sigma_{rr}/A_{rr}\sigma_0$, (b) $\Sigma_{\theta\theta} = \sigma_{\theta\theta}/A_{\theta\theta}\sigma_0$ and (c) $\Sigma_{mm} = \sigma_{mm}/A_{mm}\sigma_0$ with normalized distance, r/L^p , in Mode I direction, respectively, for Al-2024T3 TB and TPB specimens	81
Figure 17: The variation of (a) $\Sigma_{rr} = \sigma_{rr}/A_{rr}\sigma_0$, (b) $\Sigma_{\theta\theta} = \sigma_{\theta\theta}/A_{\theta\theta}\sigma_0$, (c) $\Sigma_{r\theta} = \sigma_{r\theta}/A_{r\theta}\sigma_0$ and (c) $\Sigma_m = \sigma_m/A_m\sigma_e$ with normalized distance, r/L^p , in mode II direction, respectively, for Al-2024T3 TB and TPB specimens	82
Figure 18: The variation of $\Sigma_e = \sigma_e/\sigma_0$ with normalized distance, r/L^p , in (a) mode I and (b) mode II directions, respectively, for TB and TPB specimens, power law material ($n=3$)	83
Figure 19: The variation of (a) $\Sigma_{rr} = \sigma_{rr}/A_{rr}\sigma_0$, (b) $\Sigma_{\theta\theta} = \sigma_{\theta\theta}/A_{\theta\theta}\sigma_0$ and (c) $\Sigma_m = \sigma_m/A_m\sigma_e$ with normalized distance, r/L^p , in mode I direction, respectively, for TB and TPB specimens, power law material ($n=3$)	84

Figure 20: The variation of (a) $\Sigma_{rr}=\sigma_{rr}/A_{rr}\sigma_0$, (b) $\Sigma_{\theta\theta}=\sigma_{\theta\theta}/A_{\theta\theta}\sigma_0$, (c) $\Sigma_{r\theta}=\sigma_{r\theta}/A_{r\theta}\sigma_0$, and (d) $\Sigma_m=\sigma_m/A_m\sigma_e$ with normalized distance, r/L^p , in mode II direction, respectively, for TB and TPB specimens, power law material ($n=3$)	85
Figure 21: The functions $A_{ij}(A_m)$ in mode I direction for SSY model, TP and TPB specimens, power law material ($n=10$) and Al-2024T3. (a) $A_{rr}(A_m)$ and (b) $A_{\theta\theta}(A_m)$	86
Figure 22: The functions $A_{ij}(A_m)$ in mode II direction for SSY model, TP and TPB specimens, power law material ($n=10$) and Al-2024T3. (a) $A_{rr}(A_m)$, (b) $A_{\theta\theta}(A_m)$, and $A_{r\theta}(A_m)$	87
Figure 23: The functions $A_{ij}(A_m)$ for TP and TPB specimens, power law material ($n=3$). (a) in mode I direction, (b) in mode II direction	88
Figure 24: Variation of $\Sigma_{\theta\theta}=\sigma_{\theta\theta}/\sigma_{\theta\theta}^A$ with normalized distance $r\sigma_0/J$ in mode I direction, for SSY mode, power law material ($n=10$)	88
Figure 25: Modified Arcan fixture-specimen system and finite element model	89
Figure 26: The variations of $\Sigma_e=\sigma_e/\sigma_0$ and Σ_m with normalized distance, r/L^p , in the mode I and mode II direction, Arcan specimen	90
Figure 27: The variation of $\Sigma_{ij}=\sigma_{ij}/(A_{ij}\sigma_0)$ with normalized distance, r/L^p_{II} , in mode II direction, Arcan specimen	91
Figure 28: A_{ij} as function of A_m in (a) mode I and (b) mode II directions, respectively ..	91
Figure 29: Correlation of COD to A_m and L^p in (a) mode I, and (a) mode II directions, respectively	92
Figure 30: Typical experimentally observed relationship between plastic strain and constraint	92
Figure 31: Curves of σ_e versus E_p under different stress constraint levels	93
Figure 32: Three-dimensional periodic array of spherical voids and unit cell model	93
Figure 33: Typical FE mesh for 3D simulations of void region utilizing symmetry boundary conditions	94
Figure 34: 3D Simulation results at void link-up for $f_0 = 0.005, 0.020$, and 0.080	95
Figure 35: 3D Simulation results for (σ_m, E_p) at void link-up for	96
Figure 36: Best fit results for (σ_m, σ_e) at void link-up for $0.001 < f_0 \leq 0.10$	96
Figure 37: Schematic of relationship between (σ_m, σ_e) and (E_{pc}, A_m) for a given f_0	97
Figure 38: Schematic of flat and slant crack geometries	97
Figure 39: Finite element meshes for the Arcan fixture-specimen system with	98
Figure 40: and global coordinate systems for slant crack	99
Figure 41: Finite element mesh for the Arcan fixture-specimen with a slant crack	99
Figure 42: COD variations at mid-plane and front surfaces for slant crack	100
Figure 43: Comparison of total COD for flat and slant cracks	101
Figure 44: Constraint radial comparison between the flat crack and the slant crack ...	101
Figure 45: Constraint angular comparison between the flat crack and the slant	102
Figure 46: Flow chart for 3D crack growth code, CRACK3D	103
Figure 47: Schematic of boundary lines and nodal points for description of selection process	104
Figure 48: Schematic of nodal points for description of crack surface selection	104
Figure 49: Example of 3D re-meshing results	105
Figure 50: Schematic of nodal points and elements for node identification and	106
Figure 51: Schematic of lines and elements for line identification and element modification during surface optimization	106

Figure 52: Schematic of nodal points and 3D elements for element condensation	107
Figure 53: Comparison of surface and volume meshes before and after mesh optimization	108
Figure 54: Tension torsion specimen with schematic of loading process	109
Figure 55: Close-up of crack tip region imaged during crack growth under tension-torsion loading	110
Figure 56: Profiles of fracture surface of 2024-T3 aluminum specimen for various combinations of tension and torsion loading	111
Figure 57: Evolution of slant crack growth angle during tension-torsion loading of 2.3 mm thick, 2024-T3 aluminum specimens	112
Figure 58: COD versus crack extension for various ratios of torsion and tension	113
Figure 59: Tunneling during slant crack growth under tension-torsion loading.....	114
Figure 60: Non-dimensional measure of tunneling during initial stages of crack.....	115
Figure 61: Notched cylindrical specimens (units in inches)	116
Figure 62: Optical microscope image near notch for specimen F (Light color is aluminum, dark particles are inter-metallic)	117
Figure 63: Shear specimen for void-growth studies (units in inches)	118

EXECUTIVE SUMMARY

The broad objectives of this project are to (a) develop the theoretical foundation for the development of a continuum-based, general stable crack extension criterion in ductile materials, (b) develop a computational methodology for implementing the criterion to predict stable tearing along a general path in three-dimensions, (c) develop an initial experimental data base for validation of the predictive methodology and (d) develop and validate a mixed mode fracture criterion using the initial experimental data base and completed computational methodology.

First, detailed theoretical and computational studies of void growth have been completed that show (a) for each initial void volume, a functional relationship exists between the mean stress σ_{mean} and effective stress σ_{eff} at the instant of void link-up and crack growth, demonstrating that a two-parameter fracture criterion is viable for predicting stable tearing and (b) the experimentally observed link between plastic strain and constraint (e.g., a parameter such as $A_m = \sigma_{\text{mean}}/\sigma_{\text{eff}}$) further indicates that there is the basis for obtaining a critical crack opening displacement (COD) as a function of a constraint parameter, that is, $\text{COD}(A_m)$. Here, the overall macroscopic direction of ductile stable tearing will be primarily a function of the local field quantities and not the details of the void nucleation site distribution within the material.

Second, a fully functional three-dimensional crack growth algorithm has been developed that is capable of predicting crack growth along a general, three-dimensional surface. The algorithm, designated CRACK3D, utilizes the pre- and post-processing capabilities of Ansys while performing all of the crack-front calculations internally. As part of the development process, (a) improved methods for crack tip re-meshing have been developed and implemented which only re-mesh a region around the current crack tip and (b) new approaches for volumetric and surface optimization have been developed and implemented. As part of the development process, detailed simulations have been performed to complete the debugging process.

Third, a set of controlled mode I, mixed mode I/II and mixed mode I/III experiments have been completed for aluminum 2024-T3. These experiments included (a) fatigue marking to identify the surface crack front, (b) three-dimensional non-

contacting measurements to quantify the shape of a complex, slanted fracture surface and (c) measurements of surface COD during stable tearing. In addition to these experiments, a set of experiments have been attempted to related the combination of stresses, σ_{mean} and σ_{eff} , in a region to the presence of actively growing voids. Here, the goal of the experiments is to provide quantitative evidence for defining a portion of the relationship between σ_{mean} and σ_{eff} for 2024-T3 aluminum.

Fourth, a series of computational analyses using measured surface crack shapes, crack fronts and load-surface crack extension data to develop a mixed mode fracture criterion that is capable of predicting both the direction and onset of stable tearing crack extension along a general three-dimensional path in thick and/or thin structural components.

I. INTRODUCTION

As noted by the National Materials Advisory Board [1], a critical limitation in the state-of-the-art for crack-growth simulation technology is the lack of an experimentally verifiable, general stable tearing criterion that can be applied to the whole spectrum of possible crack-tip loading conditions. This would include plane stress, plane strain and general, three-dimensional conditions.

To demonstrate the importance of a general stable tearing criterion, recent stable tearing test results [2-7] obtained on aluminum alloy specimens show a transition in crack growth mode from dominantly Mode I to dominantly Mode II at a critical loading mode mixity. This ductile crack growth phenomenon is demonstrated by inspection of the various crack paths shown in the figure below, obtained during monotonic loading of pre-cracked Arcan specimens made of 2024-T3 aluminum. The angles in Fig. 1 correspond to different loading mode mixity (ratios of Mode II to Mode I at the crack tip), where an angle $\Phi = 0^\circ$ corresponds to pure Mode I and an angle $\Phi = 90^\circ$ corresponds to pure Mode II. *What we observed repeatedly from these experiments is that when loading is predominantly mode II (e.g. when the loading angle is 75° - 90° for 2024-T3 aluminum) the immediate crack-growth path is of a mode II type.*

For ductile solids, it is well known that stable tearing criteria based on the J-integral and HRR-theory are valid only for problems involving short-range crack growth. The “local mode I” criterion and those based on G , K and/or $\sigma_{\theta\theta}$ (the crack-tip circumferential stress) have been used successfully to predict the direction of crack growth in brittle solids. *Furthermore, for crack growth in ductile solids, the G -criterion is not well defined and the local mode I criterion and the σ_θ -criterion fail to predict the experimentally observed transition in crack-growth mode (from mode I type to mode II type) as loading approaches mode II.* Since the assumption of local mode I behavior is not necessarily true for ductile materials, oftentimes leading to erroneous predictions for crack growth in many airframe materials (e.g. 2024-T3, 2524), it seems clear that basic studies which may lead to the development of an experimentally verifiable, general mixed mode fracture criterion for ductile materials is a critical need.

The idea of a CTOD-based fracture criterion dates back to the 1960s when it was first proposed by A. A. Wells to handle crack-growth problems involving dynamic fracture [8] and large-scale plasticity [9]. Additional variations in the COD criterion and studies supporting its usefulness were further demonstrated in [10-13] for theoretical analysis and for finite element-based simulations of stable crack growth in metals.

It was not until the 1980s that J. C. Newman Jr. et al. [14] published experimental results conclusively demonstrating the efficacy of a COD criterion. It was argued that crack growth occurs when the CTOD value at a fixed distance behind the crack tip reaches a critical value (which is equivalent to a crack-tip opening angle (CTOA) criterion defined at a fixed distance behind the crack tip). This criterion was then used in [13] to simulate stable crack growth and to predict a load-crack extension curve, and the prediction was found to agree well with test results.

The strongest evidence for the applicability and superiority of a COD-based criterion for mixed mode loading conditions came through recent collaborative efforts between our group and Dr. Newman who was at NASA Langley Research Center [2-7,15-23] at that time. Using experimentally measured COD values and uniaxial stress-strain curves, we were able to use finite element simulations with the COD fracture criteria to predict the load-crack extension curves that consistently match those measured experimentally. The direction of stable tearing in Arcan tests has been predicted using local mode I criteria (elastic prediction) and our mixed-mode COD criterion and compared to experimental measurements (see Figure 1), where COD predictions under small-scale yielding conditions with normalized T-stresses (given by B) are also given. The COD criterion correctly predicts the transition in crack growth direction when the mixed-mode loading angle is around 70° .

Since the measured critical COD values are located at the surface of the specimen, the effects of through-thickness variations in stress (oftentimes referred to as constraint effects) may result in a variation of critical COD values with stress state. Since the underlying mechanism for stable tearing is void growth, void sheeting and void coalescence, then the "stable tearing" process and critical COD will be related to the stress components that cause void growth. For example, in his recent article reviewing the status of stable tearing models and concepts, Thomason [24] notes that

(a) limit load between voids is a direct function of the mean stress and (b) coalescence of voids and thus crack growth occurs when the inter-void matrix reaches its limit load.

The broad objectives of this project are to (a) develop the theoretical foundation for the development of a continuum-based, general stable crack growth criterion in ductile materials, (b) develop a computational methodology for implementing the criterion to predict stable tearing along a general path in three-dimensions and (c) develop an initial experimental data base for validation of the predictive methodology.

In Section II., details of the theoretical work are discussed. In Section III, a summary of the work done to develop the computational algorithm CRACK3D is presented. In Section IV, an outline of the experimental work is given. In Section V, a summary of the work is provided.

II. THEORETICAL DEVELOPMENTS

II.1 Plane Strain Mixed Mode Crack-Tip Stress Fields Characterized by A Triaxial Stress Parameter and A Plastic Deformation Extent Based Characteristic Length **[25]**

II.1.1 Background

In an effort to determine whether mixed mode crack tip fields in ductile materials can be characterized by a minimum number of parameters, thereby simplifying the process of identifying candidate mixed mode fracture criteria, a series of detailed elastic-plastic finite element analyses were performed. Each model was subjected to mixed mode I/II loading and the crack tip fields were determined. A wide range of length scales (e.g., plastic zone size, specimen dimensions) and parameters that are a function of loading (e.g., J-integral, T-stress, mode mixity, mean stress) were investigated. Results from the finite element studies are presented, with emphasis on the effectiveness of a length scale, L^p , and a constraint parameter, $A_m = \sigma_m/\sigma_e$ (here σ_m and σ_e are the mean stresses and effective stresses, respectively, as defined in Eqs (1-3) in a forthcoming section) in characterizing the crack tip fields for all specimen geometry considered, even when large-scale yielding is presented. The self-similar

family of mixed mode crack tip fields obtained from the numerical studies is investigated in more detail.

II.1.2 Numerical Predictions for Crack-Tip Fields

Due to the large number of length scales and loading parameters that could be used to normalize crack-tip fields in ductile materials, a brief discussion of previous analytical work in this area is presented. Results from this work provided the framework for the authors to select optimal normalization parameters.

It is well known that the fracture of ductile solids has frequently been observed to be the result of the nucleation, growth and coalescence of voids, both in nominally uniform stress fields and ahead of an extending crack [26]. Since the pioneering study of McClintock [27], where he completed the analysis of the expansion of a long circular cylinder cavity in a non-hardening material, important relationships between the nucleation and growth of a void and the imposed stress and strain fields have been found [28-32]. Their work indicates that *stress triaxiality* (defined as a ratio of mean stress over effective stress) and *plastic strain* in the crack tip region play an important role in the process of ductile fracture, with different combinations of plastic strain and stress triaxiality resulting in different fracture process zones. Thus, their work suggests that two independent parameters are needed to characterize stress fields in the near-tip region, one related to stress triaxiality and the other to plastic deformation.

As shown graphically in Figures 2a and 2b, for a given angle θ (θ is the angle measured from the crack line with counter-clockwise as positive) then the length scale, L^p , based on the extent of crack-tip plastic deformation, is defined to be the radial distance from the crack tip to a point where $\sigma_e = \xi \sigma_0$, where σ_e is the von Mises effective stress, σ_0 is the initial yield stress, and ξ is a constant equal to or larger than 1.0. Note that ξ is conveniently chosen to address the potential for unconstrained yielding. That is, ξ is chosen so that (a) the length scale selected for scaling corresponds to a “contained” region (i.e., a region so defined that it does not extend to stress-free boundaries of the specimen) and (b) the size scale defined by the length parameter, $L^p(\theta)$, is expected to contain the fracture process zone. Thus, radial

variations in the crack tip stress field will be described in terms of the same normalized position within the plastic zone. Using the length scale r/L^p , a typical crack-tip plastic zone under mixed mode I/II loading (e.g., see Figure 2b) will be circular in shape (e.g., see Figure 2c), with locations having the same normalized position within the plastic zone being on nested concentric circles within the unit circle in an r/L^p coordinate system.

Based on previous work on ductile fracture, the magnitude of the quantity σ_m/σ_e in the near-tip region is a viable loading parameter for quantifying the level of constraint at any point in the crack tip field. Here, σ_e is the von Mises form for the effective stress defined by

$$\sigma_e^2 = \frac{3}{2} s_{ij} s_{ij} , \quad (1)$$

where s_{ij} represents the deviatoric stress components

$$s_{ij} = \sigma_{ij} - \frac{1}{3} \delta_{ij} \sigma_{kk} , \quad (2)$$

and δ_{ij} is the Kronecker delta. The mean stress, σ_m , is defined by the equation

$$\sigma_m = \frac{1}{3} \sigma_{kk} . \quad (3).$$

As such, the triaxial stress parameter, A_m , is defined in this paper as the near-tip value of the ratio σ_m/σ_e because numerical results in this paper shown that this ratio is basically independent of the radial distance r within the near-tip region.

It is expected that any useful description of mixed mode crack tip fields should accurately represent crack tip fields for arbitrary specimen geometry under both contained and general (uncontained) yielding conditions. This will be demonstrated by describing results obtained using the finite element method for (a) a small-scale yielding model and (b) full field, general yield solutions of edge-cracked tension specimens and bend specimens. In particular, the numerical results will show that the characteristic length scale, L^p , sets the size scale over which large stresses and strains develop and is an excellent normalizing factor for a unique set of radial variations for the crack-tip stress fields. At the same time, the constraint parameter A_m determines the magnitude

of the stress distribution while setting the level of constraint in the crack tip region due to crack geometry and loading conditions.

//.1.3 Finite Element Models

Three elastic-plastic materials will be considered in the finite element models: (a) an aluminum alloy, 2024-T3, that obeys the J_2 -flow theory of plasticity (theoretically equivalent to a non-linear elastic formulation in the absence of unloading), in which the effective stress-strain behavior is given by an experimentally measured uniaxial stress-strain curve; and (b) two materials with power hardening that obey the J_2 -deformation theory of plasticity and the uniaxial Ramberg-Osgood relationship

$$\frac{\varepsilon}{\varepsilon_0} = \frac{\sigma}{\sigma_0} + a \left(\frac{\sigma}{\sigma_0} \right)^n, \quad (4)$$

where n is the strain hardening exponent and takes the value of 3 in one case and 10 in the other, a is a material constant; $a = 1$ is selected in this study, and ε_0 is a reference strain given by σ_0/E , with σ_0 and E being the initial yield stress and Young's modulus, respectively. The stress-strain relations for these three materials are shown in Figure 3. In all three cases, $E = 71.2 \text{ GPa}$, Poisson's ratio $\nu = 0.3$ and $\sigma_0 = 344.5 \text{ MPa}$, which are consistent with values commonly used for Al2024-T3. It is noted that the model in Equation 4 includes a non-linear contribution throughout the stress-strain history, even for low stress values.

Computations were performed with small displacement theory implemented in the finite element code ABAQUS [33]. Considering the loss of hardening capacity with increasing deformation for Al2024-T3, convergence was studied for several elements including (a) a 4-node bilinear element with reduced integration, hourglass control and constant pressure capability and (b) an 8-node bi-quadratic element with reduced integration and linear pressure capability. For the finite element meshes used in this paper, converged finite element solutions were obtained from both elements. The results reported below are based on use of a 4-node finite element.

To account for the full range of mode mixity and constraint crack tip stress fields, the small-scale yielding (SSY) model with a modified boundary layer formulation (see

[34] for details) and (b) full-field solutions for TB and asymmetric TPB bars are analyzed in detail. The former provides an attractive means to study the effects of mode mixity, specimen geometry and loading on the near-tip fields without geometry specification. The latter produces full field, mixed mode crack-tip solutions associated with bending and tension loading, respectively.

The SSY model used in this work is shown in Figure 4. The crack is modeled with a focused mesh. The focused mesh contains 100 concentric circular rings. Each ring contains 72 elements concentric with the crack tip. The crack tip location contains 73 initially coincident nodes. Mesh refinement was such that elements adjacent to the crack tip had a radial length that was 1/9239 of the radial length of the outer elements. It is noted that the radial size of the smallest element is simply an artifact of the process used to ensure that the plastic zone was much smaller than the radial distance to the remote boundary, a requirement for the validity of a small scale yield model.

The remote boundaries of the SSY model at radius r_a are subjected to imposed displacements, u_x, u_y , corresponding to combined linear elastic mode I and II stress intensity factors K_I , K_{II} , and T-stress fields (for details, see Reference [34]). It is noted that the SSY model described herein is a standard method for applying selected terms in the Williams linear elastic solution to boundaries that are remote from the crack tip region.

$$\left. \begin{aligned} u_x &= R_K \left[k_1 \cos \frac{\theta}{2} \left(\frac{\kappa-1}{2} + \sin^2 \frac{\theta}{2} \right) + k_2 \sin \frac{\theta}{2} \left(\frac{\kappa+1}{2} + \cos^2 \frac{\theta}{2} \right) \right] + \frac{1+\kappa}{8} \frac{T}{\mu} r_a \cos \theta \\ u_y &= R_K \left[k_1 \sin \frac{\theta}{2} \left(\frac{\kappa+1}{2} - \cos^2 \frac{\theta}{2} \right) - k_2 \cos \frac{\theta}{2} \left(\frac{\kappa-1}{2} - \sin^2 \frac{\theta}{2} \right) \right] - \frac{3-\kappa}{8} \frac{T}{\mu} r_a \sin \theta \end{aligned} \right\}. \quad (5)$$

with

$$\left. \begin{aligned} R_K &= \sqrt{\frac{r_a}{2\pi}} \frac{\sqrt{K_I^2 + K_{II}^2}}{\mu} \\ k_1 &= \frac{1}{\sqrt{1+\omega^2}}, \quad k_2 = \frac{\omega}{\sqrt{1+\omega^2}} \\ \omega &= \frac{K_{II}}{K_I} \end{aligned} \right\}, \quad (6)$$

Here, μ is elastic shear modulus and $\kappa = 3 - 4\nu$. Let $\chi = \tan^{-1}(\omega)$, which is used as a measure of mode mixity for the SSY model. Thus, the crack tip stress fields in the SSY model depend on χ , the length parameter R_K , and T-stress, which is an in-plane measure of constraint level. In this work, increments of $K_{\text{eff}} = (K_I^2 + K_{II}^2)^{1/2}$ and T-stress were applied along the circular boundary and several combinations of T-stress ($T/\sigma_0 = 0.47$, 0.0, and -0.47) and K_{eff} (corresponding to $\chi = 0^\circ$, 36.9° , 71.2° , 90°) were used to obtain the SSY crack tip stress fields. The values of T/σ_0 presented in this work span a range that represents reasonable upper and lower bounds on the expected values for the T-stress term.

Full field, mixed mode crack-tip solutions were obtained for asymmetric three point bend (TPB) bars and slant cracked tension bars (TB). The geometry and finite element meshes for these specimens are illustrated in Figure 5. A wide range of mode mixity and constraint levels were modeled using (a) normalized values for the load eccentricity, c , corresponding to the range $0 \leq c/w \leq 1.5$ for TPB specimens and (b) values of $\beta = 0^\circ$, 15° , 30° , 60° , and 75° for TB specimens. For presentation of results, the polar coordinate system shown in Fig.1 is used, where the x-axis is along the crack direction and $+\theta$ is measured counter-clockwise. It is noted that previous researchers have tried unsuccessfully to use a J-T-mode mixity approach to characterize the maximum tension stress for the TB specimens [35].

II.1.4 Angular Variation of L^P and A_m

Since the stress variations obtained for all specimen geometries and material models exhibited nearly identical trends when using L^P and A_m to normalize the stress fields, typical finite element results are reported for the SSY model using a power law material with $n=10$.

Figure 6 highlights the angular variation of L^P for the small-scale yielding model with different mode mixity, χ , and T-stresses, where L^P is normalized by R_K given in Eq.(6). In this work, all numerical results for the definition of L^P are based on $\xi=1.2$, which corresponds to a plastic zone size determined by an equivalent plastic strain of $\varepsilon_p \approx 3\%$. Thus, a value of $\xi=1.2$ results in a fully “contained” plastic zone for the SSY

model that meets the requirement for $L_p \ll r_a$ so that the applied elastic fields dictate the conditions prevalent in the crack tip condition. As shown in Fig. 6, changes in either mode mixity or constraint level will modify the angular variation of L^p . In all cases, the maximum of L^p occurs in the same direction as the maxima of the shear stress, σ_e , and COD_{II} , that is, which is also the local mode II direction (for details about COD_I and COD_{II} , see Reference [36]). Figure 6 also indicates that, for a given T-stress, increasing the mode II component of loading will lead to an increase in the maximum value of L^p , designated as L^p_{II} . The angular variations of $\sigma_{\theta\theta}$ and σ_e are displayed in the figures for comparison.

In the direction where $\sigma_{\theta\theta}$, σ_m/σ_e and COD_I approach a maximum (i.e., a local mode I direction), L_p is a local minimum designated as L^p_I . For all cases considered here, $L^p_{II} \gg L^p_I$. Figure 7 shows variations in L^p_{II}/L^p_I as a function of mode mixity, χ , for the SSY model, where mostly $(L^p_{II}/L^p_I) > 10$. Though not shown here, similar results regarding the L^p distribution were obtained for both the TB and TPB specimens.

The angular variations of A_m , σ_{rr} and $\sigma_{\theta\theta}$ are shown in Figure 8. For all cases considered here, A_m takes its maximum value near the direction where the opening stress reaches its maximum; in this direction, the in-plane shear stress vanishes so that the stress state is locally tensile.

Trends in the angular distributions of L^p and A_m for both the TPB and TB specimen geometries are similar to those obtained for the SSY model, even though crack tip plastic deformation extends to the specimen surface in some cases. For example, as shown in Figure 9, for a typical TB specimen with $\beta=30^\circ$ and a TPB with $c/w=0.5$, as the loading increases, the crack tip region undergoes general yielding and the plastic zone extends to the specimen surfaces. For these cases, the angular distributions of L^p and A_m for both the TPB and TB specimen geometries are shown in Figures 10 and 11, respectively.

II.1.5 Radial variations along local mode I and mode II directions

In this section, the radial distribution of stresses in the crack tip region is presented for the SSY, TB and TPB models described in the previous section. Material

models considered in these studies included both (a) power law hardening with $n = 3, 10$ and (b) the measured uniaxial stress-strain data for Al2024-T3. Typical results are provided for (a) the SSY model with power law hardening ($n=10$) and (b) the TB and TPB specimens with power law hardening ($n=3$) and the measured Al2024-T3 data.

Since theoretical and experimental studies [36-38] have shown that crack initiation and stable crack extension under mixed mode I/II loading in nominally homogeneous material systems occur under either local mode I or mode II conditions, results in this section are limited to the mixed mode crack tip fields along the directions that correspond to a maximum in either local mode I or local mode II parameters. In all cases, it will be shown that the radial variation of the stress field along these directions is optimally represented as a function of the normalized distance, r/L^P , in that the normalized variations of each of the stress component collapse onto a single curve.

It is noted that, in heterogeneous material systems (e.g., welds, functionally graded materials), recent evidence suggests that flaws under nominally mode I/II loading may grow under conditions that result in a critical COD that has non-zero components for both the shear and opening displacement components. Further research will be required to determine whether this observation is due to changes in yield stress and/or local fracture toughness.

While presenting the results for the radial stress variation, it is noted that the fracture process zone for ductile materials is believed to be well within $r/L^P_I < 5$. Furthermore, results from this paper indicate that L^P_{II} / L^P_I is mostly larger than 10. As such, special attention should be directed to the radial distribution for stresses in the region $r/L^P_I < 5$ along the local mode I direction and $r / L^P_{II} < 0.50$ in the local mode II direction. It is noted that the limits for comparison given above were used since (a) conditions beyond this point are unlikely to affect fracture processes and (b) little change in trends was observed beyond this point.

First, the radial distribution of effective stress is analyzed when distance from crack tip is normalized by L^P in mode I and mode II directions, respectively. Figures 12a and 12b shows the radial variation of $\Sigma_e = \sigma_e / \sigma_0$ with normalized distance r/L^P along both the mode I and mode II directions, respectively. For all levels of mode mixity and T-stress, the data for Σ_e falls on a single curve with the amplitude, A_e (the value of Σ_e at

$r/L^p=1$), equivalent to a constant $\xi=1.2$ and independent of both T-stress and mode mixity. Clearly, within a distance of $r=5L^p_I$ in mode I direction or $r=2L^p_{II}$ in mode II direction, effective stress is uniquely normalized by L^p .

For stress components, σ_{rr} , $\sigma_{\theta\theta}$, $\sigma_{r\theta}$ and σ_m/σ_e , the radial distribution depends not only on normalized distance, r/L^p , but also on T-stress and mode mixity. To observe the radial variation of stress components using normalized distance, r/L^p , the stresses in the mode I direction and shear stress in mode II direction are scaled by their values at $r/L^p_I=1$. Normal stresses in the mode II direction are scaled by their values at $r/L^p_{II}=0.1$ since L^p has a smaller effective normalization zone for normal stress than for either shear stress or effective stress along the mode II direction. The scaled stress quantities are denoted in the figures by Σ with proper subscripts. To address this issue, we define a normalized stress Σ_{ij} along the mode I direction by

$$\Sigma_{ij} = \frac{1}{A_{ij}} \frac{\sigma_{ij}}{\sigma_0}, \text{ and } \Sigma_m = \frac{1}{A_m} \frac{\sigma_m}{\sigma_e} \quad (7)$$

for σ_{rr} , $\sigma_{\theta\theta}$ and σ_m/σ_e , respectively, where

$$A_{ij} = \frac{\sigma_{ij}}{\sigma_0} \bigg|_{r/L^p=1}, \text{ and } A_m = \frac{\sigma_m}{\sigma_e} \bigg|_{r/L^p=1} \quad (8)$$

Similarly, along the mode II direction, we define the normalized stress Σ_{ij} by

$$\Sigma_{ij} = \frac{\sigma_{ij}}{\sigma_{ij}^A}, \text{ and } \Sigma_m = \frac{1}{\sigma_m^A} \frac{\sigma_m}{\sigma_e} \quad (9)$$

for σ_{rr} , $\sigma_{\theta\theta}$ and σ_m/σ_e , respectively, where

$$\sigma_{ij}^A = \sigma_{ij} \bigg|_{r/L^p=0.1}, \text{ and } \sigma_m^A = \frac{\sigma_m}{\sigma_e} \bigg|_{r/L^p=0.1}. \quad (10)$$

The normalized shear stress component along mode II direction is defined by

$$\Sigma_{r\theta} = \frac{1}{A_{r\theta}} \frac{\sigma_{r\theta}}{\sigma_0}, \quad (11)$$

where

$$A_{r\theta} = \frac{\sigma_{r\theta}}{\sigma_0} \bigg|_{r/L^p=1}, \quad (12)$$

For all SSY model cases using power law hardening ($n=10$), the radial variation of normalized stress Σ_{ij} in the mode I direction is shown in Figures 13, where each stress component is normalized by the value at $r/L^p=1.0$. Along the mode II direction, Figure 14 presents the radial variation in Σ_{ij} for a SSY model using a power law hardening ($n=10$) material, with normal stress component normalized by the value at $r/L^p=0.10$, and shear stress component is normalized by the value at $r/L^p=1.0$. Results for the SSY model indicate that over a distance (a) $r=5L^p$ in mode I direction for all stresses, (b) $r=0.5L^p$ in mode II direction for the normal stresses and (c) over a larger distance for σ_{r0} in the mode II direction, normalized stresses for all cases are effectively collapsed onto a unique radial distribution.

Analyses were also completed for the TB and TPB specimens using a power law material ($n=10$). Though the specimens exhibited both contained and large scale yielding similar to that shown in Fig. 9, results indicate that the r -dependence of the stress components are similar to those shown in Figs 12 to 14 for the SSY model.

Using the Al2024-T3 material model, the r -dependence of stresses for the TB and TPB specimens is shown in Figures 15, 16 and 17. Comparison of these results to those shown in Fig. 12-14 indicates that near the crack-tip, the radial distribution of stresses deviates from those of a power law material; outside the small region, the radial distribution for each stress component is nearly the same, whether one uses an Al2024-T3 material or a power law material ($n=10$).

Finally, using a power law material ($n=3$) and normalizing by a distance L^p that is calculated using the same value $\xi=1.2$, the radial distributions for the normalized stress components were determined for both the TB and TPB specimens. Figures 18, 19 and 20 present the results for all stress components, demonstrating that the normalized stress components are adequately normalized for all material models.

II.1.6 Relationship between A_{ij} and A_m

The radial distribution results indicate that the mixed mode crack tip fields are self-similar when L^p is used to normalize radial distance from the crack tip. However, if L^p and A_m are to be used to characterize mixed mode I/II crack tip fields, the amplitude of the stress fields, A_{ij} , defined as value of σ_{ij}/σ_0 at $r=L^p$, must be a well-defined function of the stress triaxiality parameter A_m . Furthermore, at least along the directions corresponding to either local mode I or local mode II, the relationship $A_{ij}(A_m)$ must be independent of mode mixity, specimen geometry and loading (or T-stress for SSY model)

Using Eq (8) for A_{ij} and A_m in the local mode I direction, Eq (10) with

$$A_{ij} = \frac{\sigma_{ij}^A}{f(0.10)}, \quad f(0.10) = \text{value of } \Sigma_{r\theta} \text{ at } r = 0.10 L_{II}^p, \quad (13)$$

for A_{ij} and A_m in mode II direction and Eq (12) for $A_{r\theta}$ in mode II direction, the relationship $A_{ij}(A_m)$ for both mode I and mode II directions is presented in Figure 21 and Figure 22, respectively. Note that the location, r , in (13) used to determine $\Sigma_{r\theta}$ and normalize stresses along the local mode II direction is arbitrary and does not alter the results in any significant manner.

As shown in Eq (13), $f(0.10)$ is a value of a radial stress distribution function at $r/L_{II}^p=0.1$, and can be taken as the value of $\Sigma_{r\theta}$. In these figures, results for both Al2024-T3 and power law hardening with $n=10$ are shown. For a power law material with hardening exponent $n=3$, the amplitude of the stress components A_{ij} for the TB and TPB specimens are plotted against A_m in Figure 23. Results presented in Figs 21-23 clearly indicate that the relationship $A_{ij}(A_m)$ is geometry and loading independent, demonstrating that stress amplitudes can be uniquely characterized by A_m .

II.1.7. The A_m -Family of Mixed Mode Crack Tip Fields

As shown in the previous section, it is possible to describe mixed-mode I/II crack-tip stress fields for SSY, TB and TPB specimens when using a characteristic length parameter, r/L^p , and a constraint parameter, A_m . When used in this manner, normalized

crack-tip stresses at the same normalized position will have the same form. Furthermore, the level of constraint (e.g., magnitude of A_m) within the crack tip region defined by L^p determines the amplitude of the stress field.

The results provided previously strongly suggests that mixed mode I/II crack tip stress fields have the form

$$\frac{\sigma_{ij}}{\sigma_0} = A_{ij} f\left(\frac{L^p}{r}\right), \quad (14a)$$

with

$$A_{ij} = A_{ij}(A_m, \theta). \quad (14b)$$

With regard to the model proposed above, it is noted that previous studies for non-hardening and perfectly plastic materials [39] are supportive of the general concepts embodied in Eqs (14a) and (14b). Specifically, his work has shown that (a) the stress and deformation fields in the crack-tip region are strongly dependent on specimen geometry and (b) the crack-tip plastic zone shape and size are a function of loading conditions. The proposed model directly incorporates these concepts through the use of L^p for normalization of the length scale and A_m to characterize both loading and constraint effects.

In fact, both analytical results and our FEM data indicate that a viable form for the stress components is of the form;

$$\Sigma_e = \xi \left(\frac{L^p}{r}\right)^{\frac{1}{n+1}} \text{ and } \Sigma_{ij} = \Sigma_{ij}^A \left(\frac{L^p}{r}\right)^{\frac{1}{n+1}} \quad (15)$$

where (a) $\Sigma_{ij}^A = 1.0$ for normal stress σ_{rr} and $\sigma_{\theta\theta}$ in mode I direction and $\Sigma_{ij}^A = 1.0$ for $\sigma_{r\theta}$ in the mode II direction. Furthermore, $\Sigma_{ij}^A = (10)^{1/n+1}$ for σ_{rr} and $\sigma_{\theta\theta}$ in mode II direction. As shown in Figures 12-20, Eqs (15) are in very good agreement with results from finite element analysis when L_p normalizes distance. In particular, triaxial stress σ_m/σ_e for all cases is approximately independent of the normalized distance from crack tip, so that, $\sigma_m/\sigma_e \approx A_m$.

II.1.8. Concluding Remarks

Experimental observations and finite element simulations of stable crack growth in aluminum alloys under mixed-mode loading conditions have shown that ductile crack growth is along local mode I or mode II directions. Results from this study demonstrate that the crack-tip stress fields along these two directions can be scaled onto master curves that hold for a variety of cases studied that involve different loading mode mixity, material hardening behavior, geometry, and boundary conditions. The parameters used to scale the field variations are the stress triaxiality A_m , which is the ratio between the mean stress and the effective stress within near crack-tip region, and the length scale, L^p , which is based on the extent of crack tip plastic deformation. In particular, L^p scales the radial distance to the crack tip while A_m controls the amplitude of the stress component.

Furthermore, numerical evidence and analysis of the equilibrium equation suggest that the utility of A_m and L^p in scaling the crack-tip stress fields may be extended to the whole crack-tip region, within an extent that is much larger than the expected fracture process zone. Thus the two parameters proposed in this study, A_m and L^p , are functions of the angular position θ . Within the crack-tip zone in which L^p scales the fields in the radial direction, the relationship between the angular variations of the crack-tip stresses and $A_m(\theta)$ is found to be independent of the specifics of the problem, such as loading mixity, geometry, and boundary conditions, etc. This seems to suggest that the A_m -family of mixed mode crack-tip fields is totally defined by A_m and L^p .

In addition to being able to scale the crack tip fields, A_m and L^p are also shown by the finite element results of this study to play essential roles in determining the crack growth direction. For a range of problems studied, the finite element solutions of the crack-tip fields indicate that the local mode I direction coincides with the maximum direction of A_m and $\sigma_{\theta\theta}$, and the local mode II direction coincides with the maximum direction of L^p and σ_e . Thus A_m and L^p are equivalent to $\sigma_{\theta\theta}$ and σ_e , respectively, in predicting the direction of crack growth. Thus, these studies imply that high values for

σ_m/σ_e will promote the nucleation of microvoids from large particles; this will contribute to mode I dimpled fracture. Conversely, large values for L^p , which corresponds to high values for effective and shear stresses, is associated with void sheeting and the formation of an intense slip-band resulting in local shear fracture.

II.2. THE BASIS OF COD FRACTURE CRITERIA FOR MIXED MODE I/II CRACK INITIATION AND GROWTH IN THIN SHEET MATERIALS [40]

II.2.1 Characteristic Crack Tip Parameters

Following the process outlined in Section II.1 for plane strain, the crack tip fields are analyzed for plane stress problems with constraint conditions varying from small scale yielding to large scale yielding. Through both analytical and numerical studies, it is shown that the crack tip stress and plastic strain along mode I and mode II crack growth directions can be characterized by a characteristic length parameter, L^p , and crack tip region constraint parameter, σ_m/σ_e .

Furthermore, results indicate that σ_m/σ_e takes its maximum value along local mode I directions and L_p takes its maximum value along mode II directions. Finally, results indicate that the characteristic crack-tip parameters, L^p and σ_m/σ_e , can be correlated to parameters such as crack opening displacement (COD) measured at a fixed distance behind crack tip.

II.2.2 Plane stress mixed mode I/II crack tip fields characterized by a characteristic length and stress triaxility parameter

As in II.1, two characteristic parameters, L^p and A_m , are used to characterize the mixed mode I/II crack tip field variations along potential mode I and mode II crack growth directions for a specimen having plane stress conditions; see Figure 1 for graphical description.

As was noted in Section II.1.7, stresses in the crack-tip region are expected to be self-similar and follow the form noted in Eqs 14 and 15. If one substitutes Eq. (14) into stress-based equilibrium equations, it is easily shown that

$$f\left(\frac{L^p}{r}\right) = \left(\frac{L^p}{r}\right)^s, \quad (16)$$

where $s=1/n+1$ is material related constant. Furthermore, along the local mode I and mode II directions, one can use the presence of a maximum in the opening stress ($d\sigma_{\theta\theta}/d\theta = 0$), and shear stress ($A_{r\theta}=0$) to obtain

$$\left. \begin{aligned} A_{rr} &= \xi \left(\frac{3}{2} A_m - \frac{\sqrt{12 - 27 A_m^2}}{6} \right) \\ A_{\theta\theta} &= \xi \left(\frac{3}{2} A_m + \frac{\sqrt{12 - 27 A_m^2}}{6} \right) \end{aligned} \right\}, \quad (17)$$

in mode I direction, and the presence of a maximum in the shear stress to obtain

$$\left. \begin{aligned} A_{rr} &= \frac{2}{2-s} \xi A_m \\ A_{\theta\theta} &= \frac{2(1-s)}{2-s} \xi A_m \\ A_{r\theta} &= \xi \sqrt{\frac{1}{3} - \left(\frac{s}{2-s}\right)^2} A_m^2 \end{aligned} \right\}, \quad (18)$$

in mode II direction.

For plane stress problems, the ability of A_m and L^p to characterize the crack tip fields under mixed mode I/II conditions will be demonstrated by describing results obtained using the finite element method for (a) an Arcan-specimen and (b) a small-scale yielding model.

II.2.3. Finite Element Studies

Using the same material properties and procedures, as described in Section II.1.3, to analyze both a small scale yielding model (SSY) and the Arcan specimen geometry shown in Figure 25, computations were performed with small displacement theory implemented in the finite element code ABAQUS [33]. The results reported below are based on 4-node bilinear element with reduced integration, hourglass control and constant pressure capability.

With regard to the effects of large deformation and their impact on results presented here, it is noted that these effects will be localized to positions very near the crack tip for all cases presented herein. If specific information is required for position very close to the crack tip, then additional analyses would be required that focus on these regions to ascertain whether the fields vary significantly from trends identified in this work.

II.2.4 Radial Variations along Local Mode I and Mode II Directions

Studies of the angular variations of L^p and A_m for both the Arcan specimen and the SSY indicate that (a) the direction corresponding to a maximum L_p or σ_e represents a possible direction for shear type fracture, and (b) the direction along which A_m takes its maximum value corresponds close with the direction where the opening stress reaches its maximum tensile value, resulting in void nucleation in the area and mode I fracture.

First, the radial distribution of effective stress is analyzed at two loading levels, loading when crack initiation occurred in Arcan specimen and also the maximum loading. Figures 26 shows the radial variation of $\Sigma_e = \sigma_e / \sigma_0$ with normalized distance r/L^p along both the mode I and mode II directions, respectively, as well as the radial distribution for the mean stress $\Sigma_m = \sigma_m / \sigma_0$. For all loading angles ($\Phi = 0^\circ$ to 90°), the data for Σ_e falls on a single curve with amplitude, A_e , (the value of Σ_e at $r/L^p = 1$), equivalent to a constant $\xi = 1.2$, and independent of loading angle. The same conclusion was obtained by analyzing results from the SSY model.

Stress components, σ_{rr} , $\sigma_{\theta\theta}$ and $\sigma_{r\theta}$, depends not only on normalized distance, r/L^p , but also on constraint and mode mixity. To observe the radial variation of stress components, each stress component is normalized by its value at $r=L^p$, denoted by Σ_{ij} . The normalized stresses for all cases can be plotted with normalized distance r/L^p along the local mode I and mode II directions, respectively. Results from all cases, including the Arcan specimen and the SSY model, show that radial variations of each stress component along local mode I and mode II direction collapse onto a single master curve, provided that the radial distance is normalized by the length scale L^p .

Figure 27 displays radial variations of normal and mean stresses with normalized distance r/L^P in mode I direction for Arcan specimen at two loading levels. Along this direction, the shear stress is identically zero. The results clearly indicate that the normal stress data is collapsed onto a single curve when distance is normalized by L^P . Along the mode II direction, radial variations for both the shear stress and mean stress with normalized distance, $r/L^{P_{II}}$ are shown in Figure 27. Results in Figure 27 show that along the mode II direction, shear stress has the form of Eq. (14), and the mean stress is nearly a constant over a distance of $r=2L^{P_{II}}$. It is worth noting that the mean stresses shown Figure 27 are for Arcan specimen with $\Phi < 65^\circ$; for $\Phi > 70^\circ$, the normal stresses are close to zero.

II.2.5 Relationship between A_{ij} and A_m

Along either mode I or mode II directions, results in Figures 26 and 27 indicate that radial distances are adequately normalized by L^P . However, if L^P and A_m are to be used to characterize mixed mode I/II crack tip fields, the amplitude of the stress fields, A_{ij} , defined as value of σ_{ij}/σ_0 at $r=L^P$, must be a well-defined function of A_m . Furthermore, at least along the directions corresponding to either local mode I or local mode II, the relationship $A_{ij}(A_m)$ must be independent of mode mixity, specimen geometry and loading (or T-stress for SSY model). Finite element results for $A_{ij}(A_m)$ along both mode I and mode II directions for the Arcan specimen and SSY model are presented in Figure 28. Results clearly indicate that the relationship $A_{ij}(A_m)$ is geometry and loading independent, demonstrating that stress amplitudes can be uniquely characterized by A_m .

II.2.6 Implication for Development of Stable Tearing Criterion

In general, crack initiation and growth are assumed to occur when a combination of stress or strain components in either the mode I or mode II directions attain a critical value. For both plane stress and plane strain conditions, our results have shown that the fracture event can be characterized by crack tip field parameters, A_m and L^p , as

$$F(L^p, A_m) = \text{constant} . \quad (19)$$

As an example, the mixed mode COD fracture criterion can be explored through correlation of COD value to the characteristic crack tip stress field parameters, A_m and L^p . Defining COD as the magnitude of the crack opening displacement measured at 1mm behind crack tip for all models considered in this work, Figure 29 presents the numerically predicted COD/L^p is related to A_m for both the mode I and mode II directions, respectively. If mode I type fracture is the dominant fracture mechanism (Fig.29a, $\beta < 70^\circ$ for Arcan specimen), COD is a function of L^p and A_m ,

$$\frac{COD}{L^p} = g_I(A_m^I). \quad (20)$$

Thus, general form of COD fracture criteria for crack growth along the mode I direction is

$$F_I(COD, A_m^I) = C_I . \quad (21)$$

where C_I is material constant. The form of Eq. (20) depends on a special stress combination for crack growth in mode I direction.

It is noted that the prediction of the direction and onset of crack extension is relatively insensitive to the distance behind the crack tip. For example, the investigators have successfully used distances between 0.50mm and 1.50mm to predict experimental results; other distances may also be effective for predictions, though the investigators have not used other distances in their studies.

Along the Mode II direction, COD is a function of L^p and A_m parameters and has the form , i.e.

$$\frac{COD}{L_{II}^p} = g_{II}(A_m^{II}). \quad (22)$$

Thus, a general form for a COD fracture criteria for crack growth along the mode II direction is

$$F_{II}(COD, A_m^{II}) = C_{II}. \quad (23)$$

where C_{II} is material constant. The form of Eq. (22) depends upon the combination of crack tip field parameters in mode II direction. In particular, for mode II fracture observed in the Arcan specimen, which occurs when $\beta > 70^\circ$, A_m^{II} is close to zero. Thus, $g_{II}(A_m^{II})$ in Eq. (22) is nearly a constant (Fig.29b) and the general form for a plausible COD fracture criterion for crack growth in the mode II direction is,

$$COD = \text{constant}. \quad (24)$$

II.2.6 Concluding Remarks

Results from detailed finite element and theoretical analysis for the Arcan specimen and SSY model are in excellent agreement with FE stress distributions for models ranging from small scale yielding to large scale yielding. Specifically, the results indicate that along potential mode I and mode II crack growth directions, (a) the mixed mode I/II stress fields can be collapsed onto a single curve when L_p normalizes distance from crack tip and (b) the magnitude of the stress field depends solely on A_m . Thus, the characteristic length scale, L^p , sets the size scale over which large stresses and strains develop and A_m scales the magnitude of the crack tip stress components.

II.3. Basic studies of ductile failure processes and implications for fracture prediction

II.3.1. Background

Fracture of ductile materials has frequently been observed to result from the nucleation, growth and coalescence of microscopic voids. Experimental and analytical studies have shown that two parameters — **the stress constraint factor and the effective plastic strain** — play a significant role in the ductile failure process.

Experimental and theoretical results from previous sections as well as from other authors suggest that these two parameters are not independent of each other at failure initiation.

Hancock and Mackenzie [41] experimentally studied the mechanisms of ductile failure in high-strength steels subjected to multi-axial stress states and evaluated the effect of stress constraint factor on the average plastic strain to failure initiation by use of the Bridgman's equation. Subsequently, Walsh et al [42] investigated the ductile fracture of 2134 type Al alloys. Figure 30 shows a typical experimental relationship between plastic strain and constraint. As shown in Fig. 30, their results indicate that rupture ductility decreases monotonically with increasing levels of stress constraint. For a given stress state, the effective plastic strain at failure initiation should be specified uniquely by the relation of effective plastic strain at failure initiation to a measure of constraint. In this regard, numerical results also indicates the stress constraint plays a key role in the ductile-brittle transition in small scale yielding [43].

A recent comprehensive review paper on ductile fracture modeling by Thomason [24], which utilizes extensive experimental, theoretical and computational results obtained both by the author and recognized researchers throughout the world, provides a clear framework for ductile fracture modeling. In his work, Thomason provides convincing evidence that (a) crack extension during the void-coalescence process is by inter-void matrix failure at limit load, (b) theoretical formulations emphasizing volumetric dilation as the void coalescence criterion are inconsistent with a wealth of experimental evidence obtained from SEM and micro-structural observations of ductile fracture and (c) numerical simulations of the void coalescence process, where uniqueness issues may arise due to the plastic velocity field, may limit the applicability of typical finite element methods. Also, experimental evidence [24] indicates that the overall macroscopic direction of crack extension is a function of the local field quantities and not the details of the void nucleation site distribution.

Utilizing the experimental work noted above and by making use of a unit cell model, the enclosed work will show that two parameters—a *stress constraint factor* (σ_m/σ_e) and the *effective plastic strain* (ε_{pc}) — provide the basis for developing a framework to characterize the effect of stress constraint on ductile failure of materials.

This methodology is based on the experimental evidence that the effective plastic strain at failure initiation has a one-to-one relationship with the stress constraint. In Section II and the Appendix, it is shown that the relationship shown in Fig. 30 for σ_m/σ_e and ε_{pc} leads to a failure initiation model indicating that the effective stress reaches its maximum under constant constraint loading conditions. Section III shows detailed numerical analyses based on a three-dimensional unit-cell model to assess the viability of the proposed failure initiation model. Based on the numerical results, a stress constraint-based failure criterion has been developed.

II.3.2 A methodology for failure initiation study

As shown in Figure 30, the effective plastic strain at failure initiation, E_{pc} , is a function of stress constraint, where constraint is defined by A_m .

For ductile materials, suppose that f is the void volume fraction in the material, the definitions of average stress and strain are as follows [44]

$$\varepsilon_{ij} = \frac{1}{V} \int_A \frac{1}{2} (u_i n_j + u_j n_i) dA \quad (25)$$

$$\sigma_{ij} = \frac{\partial \dot{W}}{\partial \varepsilon_{ij}} \quad (26)$$

where V is the total volume of the cell model (matrix+void), A is the total area of outer surface of the model, and n_i is the unit outward normal on A , \dot{W} is the strain energy rate of the model. The corresponding effective stress and effective plastic strain σ_e and ε_p .

When $f=0$, the curve of σ_e versus E_{pc} will be independent of stress constraint A_m . In fact, taking into account the effect of impurities, inclusion separation in material, especially under finite deformation, the deformational behavior of porous material is a strong function of stress constraint; volumetric deformation is dominant under high stress constraint, while the shape change is dominant under lower stress constraint.

Because of micro-structural variation of material under different stress constraint, some of the material properties will not keep constant under different levels of stress constraint. For instance, σ_e versus E_{pc} will have different relationships for different levels of stress constraint. If the stress constraint A_m^i is constant throughout the loading history, then the relationship between effective stress and effective plastic strain is illustrated in Figure 31 for three different values of constraint.

For voided materials, the initial void volume fraction in the matrix is defined as f_0 . For voided materials, the macroscopic (some refer to these as mesoscopic) strains and stresses in the study of the cell model (matrix +void) are defined using terminology in previous work [44]. Numerical studies have shown that the relationship of macroscopic effective stress σ_e to macroscopic effective plastic strain E_p will be a function of constraint [45]. Furthermore, experimental results [41] for notched specimens for three low-alloy steels show that the critical effective plastic strain, E_{pc} , at failure initiation is a monotonically decreasing function of the level of constraint, as shown in Figure 30, where the constraint parameter is $A_m = \sigma_m/\sigma_e$.

II.3.3. A unit-cell model and numerical results

The unit-cell model of a porous ductile material to be studied here, as shown in Figure 32, is defined by a three-dimensional periodic array of spherical microvoids in an elastic, strain-hardening plastic matrix, described by Eq (27).

$$\varepsilon = \begin{cases} \frac{\sigma}{E} & \text{for } \sigma \leq \sigma_y \\ \frac{\sigma_y}{E} \left(\frac{\sigma}{\sigma_y} \right)^n & \text{for } \sigma > \sigma_y \end{cases} \quad (27)$$

where σ_y is the initial uniaxial yield stress, E is the Young's modulus and n is the strain hardening exponent for 2024-T3 aluminum.

Figure 33 shows a one-eighth, three-dimensional model for a unit cell, respectively. In this work, initial void volume fractions in the range $0.00125 < f_0 < 0.1000$ were modeled. All 3D analyses were performed using (a) the commercial code, ANSYS, Version 5.7, and (b) the large deformation formulation in ANSYS for both rotations and

strains. Detailed convergence studies were performed for all initial void volume fractions using four separate finite element models to determine the appropriate element size on the void boundary and throughout the volume. The convergence studies indicated that a total of 3740, ten-node tetrahedral elements with 6426 nodes were sufficient for the 3D analyses. Tolerances used in ANSYS to determine convergence of the solution during the loading process were set at 0.0001 for the ratio of the residual in total force (moment) to the total force (moment).

Boundary conditions for the analysis include (a) symmetry displacement conditions $u_{x1} = 0$ in plane of $x_1 = 0$, $u_{x2} = 0$ in plane of $x_2 = 0$, $u_{x3} = 0$ in plane of $x_3 = 0$) and (b) uniform displacement loading along remaining surfaces $u_{x1} = C_{x1}$ in plane of $x_1 = L_0$, $u_{x2} = C_{x2}$ in plane of $x_2 = L_0$, $u_{x3} = C_{x3}$ in plane of $x_3 = L_0$).

By varying the values for C_{x1} , C_{x2} and C_{x3} , the values of σ_m , σ_e and A_m applied to the unit cell are computed by (a) integrating the tractions on the surfaces $x_i = L_0$ to obtain the force vectors, (b) computing the average surface tractions using the surface areas and (c) using the resulting stresses to determine the average applied values for σ_m , σ_e and A_m . The values for the applied stresses varied over a wide range given by the inequalities

- $0 < \sigma_m < 1200\text{Mpa}$
- $50\text{Mpa} < \sigma_e < 590\text{Mpa}$
- $0 < A_m < 10$

Each finite element analysis is performed under displacement-control. The boundaries are displaced uniformly and monotonically throughout the loading process. In addition, all displacements are increased in the same proportion throughout the loading process, so that a proportional displacement loading process was used for all finite element analyses.

For all cases, the condition of link-up is defined as the instant when the effective plastic strain contour $\varepsilon_p = \varepsilon_p^c$ intersects both the void boundary and a symmetry boundary for a neighboring void. To determine when a contour having the pre-specified ε_{pc} continuously extends between the void boundary and the neighboring region, the solution at incremental displacement steps is stored and evaluated during post-processing. By symmetry, the contour will extend to each neighboring void also. Once

the appropriate loading step is determined, the average applied values for all stress components at incipient void link-up are computed, including σ_m , σ_e and A_m .

For cases approaching pure shear ($A_m \rightarrow 0$), it is noted that large distortions of the void occurred, resulting in collapse of the void during the loading process. In these cases, localization of effective plastic strain was observed along a well-defined direction and link-up was defined in the manner noted above. Since void boundary contact was not considered in our analyses, it is important to note that (a) void boundary contact only occurred for low constraint and (b) link-up occurred prior to void boundary contact for almost all of the low constraint cases ($A_m \geq 0.01$) considered. For those few cases where void contact occurred prior to link-up conditions, our studies indicate that using contact to define link-up would have negligible effect on the results.

For specific values of link-up plastic strains, ε_{pc}^i , and a range of applied displacement boundary conditions, Figure 34 show the values of (σ_m, σ_e) that were applied to the region at link-up for 3D conditions and $f_0 = 0.005, 0.020$ and 0.080 . The values were selected to span the range measured by the investigators in 2024-T3 aluminum ($f_0 = 0.035$) and 2524 aluminum ($f_0 = 0.014$).

As is apparent in the numerical results shown in Figure 34, for each ε_{pc} there are several values of (σ_m, σ_e) obtained by the simulations that result in link-up to the neighboring void. Since previous experimental evidence (e.g., see Fig. 30) suggests that a unique, monotonic relationship exists between A_m and ε_{pc} , an approach is needed to determine whether the simulations contain the requisite information for (a) predicting void link-up while simultaneously resulting in a monotonic A_m - ε_{pc} relationship.

Inspection of the data in Figures 34 suggests that the simulation results for each value of f_0 are bounded by an envelope function. In each case, the simulation results for each ε_{pc}^i construct the envelope function since they are individually tangent to the envelope. Conceptually, the envelope function provides a unique combination of stress values for each value of f_0 . Furthermore, by construction each value on the envelope is uniquely related to a specific effective plastic strain, ε_{pc} .

To investigate the relationship between constraint and ε_{pc} , for the (σ_m, σ_e) values represented by each envelope function the boundary displacement u_i in Equation (25) is

used to calculate the average effective plastic strain. The resulting relationship between average effective plastic strain ε_{pc} and constraint A_m for the 3D models is shown in Figure 35.

The results in Figures 34 and 35 demonstrate that each envelope function corresponds to a monotonic relationship between effective plastic strain and constraint A_m that is fully consistent with experimental evidence such as shown in Figure 30; ε_{pc} decreases with increasing constraint. Figure 36 presents the locus of envelope values (σ_m, σ_e) at void link-up for each f_0 .

The results in Figures 30-36 suggest that there are two interpretations of the proposed local void link-up criterion. First, for each void volume fraction f_0 , there exists a locus of values for (σ_m, σ_e) that correspond to local stress conditions resulting in void link-up, where the effective plastic strain at void link-up varies with the corresponding constraint, A_m .

Second, consistent with the discussion given above, it is shown that the locus of values for (σ_m, σ_e) is consistent with the achievement of a maximum in the effective stress under a constant level of constraint, A_m . Considering the effective plastic strain corresponding to the maximum effective stress as the plastic strain at the initiation of void link-up for each level of constraint, then the effective plastic strain at void link-up under different stress constraint will decrease monotonically with increasing constraint. These concepts can be formulated into a void link-up criterion:

Under a constant level of constraint, failure initiation occurs in a ductile material when the effective stress reaches its maximum in the loading history.

It is noted that this criterion is consistent with both experiment results [41,42] and numerical predictions [45].

Furthermore, as shown in Figure 37, it is possible to demonstrate that, if one assumes a one-to-one relationship $F(\varepsilon_{pc}, A_m, f_0)$ between the critical plastic strain in the remaining material and macroscopic stress constraint A_m such as shown in Figs 30, 31 and 35, then there exists a unique functional relationship $H(A_m, \sigma_e, f_0)$ at failure initiation.

Conversely, it can be shown that if one assumes there exists a unique functional relationship $H(A_m, \sigma_e, f_0)$ at failure initiation and a monotonic relationship between ε_p and σ_e for each void volume fraction and constraint. This implies a unique functional relationship $F(E_{pc}, A_m, f_0)$ that is similar to the form shown in Figure 1.

II.3.4 Concluding Remarks

Based on previous experimental and analytical results, a methodology for the prediction of three-dimensional ductile fracture in materials. Numerical analyses of a three-dimensional unit cell model were conducted to investigate the effect of stress constraint on failure initiation.

Since void growth is the established mechanism for crack extension in such material systems, and the initial volume fraction of impurities with weak interfaces is a reasonable estimate for f_0 , the void link-up relationship $H(A_m, \sigma_e, f_0)$ obtained through detailed numerical analyses demonstrates that $\sigma_e(A_m)$ at the onset of crack extension for a given f_0 . Furthermore, since the crack opening displacement, COD, at any position behind the crack tip is the integrated effect of the elastic-plastic crack tip strain fields and it has been shown that $\varepsilon_p(\sigma_e(A_m, f_0))$, then in regions where plastic deformation is dominant a viable COD fracture criterion that is consistent with the void link-up concepts outlined in this work is $COD(A_m; f_0)$. Here, it is expected that the critical value of COD will decrease with increasing constraint.

II.4 Stress and Deformation fields Comparison between Flat and Slant Cracks under Remote Mode I Loading

II.4.1. Background

A phenomenon observed in thin sheets of many ductile materials is the transition from an initially planar, flat crack in the L-T orientation into a through-thickness slant crack surface under Mode I loading.

Lloyd and Piascik [46] analyzed the stable tearing process in 2.3mm sheets of 2024-T3 aluminum alloy M(T) specimens using fracture surface micro-topography reconstruction techniques. Their results show that, the L-T orientation (i.e., the load was applied in the longitudinal or rolling direction and the crack was in the transverse direction) exhibit a high degree of slant fracture. Large shear lips form along both sides of the specimen and grow increasingly larger during the stable tearing process. The increase in the slant angle with increased crack length suggests the presence of a Mode III deformation component associated with large amounts of slant fracture [46].

In 1997, Manoharan [47] presented experimental data for a series of combined mode I-mode III fracture toughness tests conducted on a wide range of materials, including steels, aluminum alloys, metal matrix composites, ceramics and polymers. Choosing the J-integral as the most appropriate parameter to analyze the fracture of the more ductile materials, his results show that some ductile materials have reduced fracture toughness for a crack angle of 45°.

In an effort to understand this process, a detailed three-dimensional finite element analysis is performed, with emphasis on determining the CTOD variation, radial and angular variations of constraint, mean stress and effective stress at different through-thickness locations for both (a) a single edge flat crack and (b) a slant crack in an Arcan specimen. Figure 38 shows the geometries of both a flat and slant crack.

II.4.2. Mesh design for Arcan specimen and test fixture

The Arcan fixture and test specimen under investigation are shown in Figure 39. The fixture was modified for stable tearing tests to include a number of bolts and hardened drill rod inserts for stiffening and strengthening of the specimen-fixture connection.

The loading fixture shown in Fig. 39 consists of a pair of grips. It is made of 15-5PH stainless steel, with a thickness of 19mm (0.75in). The test specimen shown in Fig. 2(b) is made of 2024-T3 aluminum and has a thickness of 2.3mm (0.09in). In the fixture region, the steel has a Young's modulus, $E = 207\text{GPa}$ (30.012E6 psi), a Poisson's ratio, $\nu = 0.3$, an initial yield stress, $\sigma_0 = 1723.8\text{MPa}$ (250ksi). In the specimen region, the aluminum alloy has a Young's modulus, $E = 71.71\text{GPa}$ (10.35E6 psi), a Poisson's ratio, $\nu = 0.3$, and an initial yield stress, $\sigma_0 = 358.5\text{MPa}$ (52ksi). Both the 15-5PH steel and 2024-T3 aluminum exhibit strain hardening behavior and this is included in the simulations. In the finite element simulation both materials are modeled with an isotropic strain hardening behavior. However, the 15-5PH material did not yield during the analyses, so only the elastic response was required..

In all analyses, the X-axis represents the global x-direction (parallel to the flat crack growth direction). Y is the global y-direction which is perpendicular to the flat crack surface while Z is the global z-direction (parallel to the crack front of the flat case). It should be noted that for the flat crack, the global and local coordinate systems coincide.

It is noted that Deng and Newman [48] argued that since the fixture and pins in an Arcan test are relatively rigid compared to the specimen, the connection between the fixture and specimen can be approximated by a rigid and continuous joint. Thus in the finite element analysis, the specimen-fixture system is treated as one continuous solid with two regions of different thickness and material properties. Also due to the fixture rigidity, the effect of omitting the loading holes on the load transfer to the specimen is expected to be insignificant.

II.4.2.1 Flat Crack

Figure 39 shows both the overall Arcan specimen mesh and the focused crack tip mesh. For the flat crack case, only half of the geometry is modeled due to symmetry about the mid-plane. A range of mesh density values is used to assess convergence. Here, convergence was assumed when the stresses and strains varied by no more than 3% as the mesh was refined. In this work, the converged flat crack mesh (Fig. 46) consists of 37260 eight-node brick elements with a total of 42504 nodes. The eight-node brick element used has 3 degrees of freedom at each node, namely translations in x, y and z directions. 27660 elements are used in the specimen region and 9600 elements in the fixture region. The Arcan test specimen mesh consists of 10 through thickness layers. Smaller elements, on the order of 0.0218mm (0.00086in), are distributed on the first circular ring around the crack front. Further away from the crack front, coarser elements are used for the remaining 49 circular rings that make up the focused mesh.

Loading of the specimen is achieved by specifying a displacement loading in the y-direction ($U_y = 0.116\text{mm}$) at the upper loading nodes set. The upper loading nodes lie along the same through thickness line, representing an approximation for the Mode I loading hole location. The corresponding nodes at the bottom are fixed in all directions ($U_x = U_y = U_z = 0$). Symmetry about the mid-plane requires that all nodes lying on that plane to be fixed in the z-direction ($U_z = 0$). To eliminate rigid body rotation, a node is fixed in the x-direction. For convenience, the mid-plane node of the upper loading nodes set is chosen for that purpose.

II.4.2.2 Slant crack mesh

The slant crack configuration and associated coordinate systems is shown in Figure 40. For the slant case, X' is the local x-direction (parallel to the slant crack growth direction). Y' represents the local y-direction (perpendicular to the slant crack

surface). Z' is the local z-direction (parallel to the crack front of the slant case). The slant angle, $\alpha = 38^\circ$, is based on previous experimental data [49].

The finite element mesh for the slant crack case is shown in Figure 41. As with the flat crack, convergence studies were performed to verify that the field quantities were accurately estimated. The mesh used in this work is composed of 74520 eight-node brick elements with a total of 81516 nodes. A total of 55320 elements are used in the specimen region while 19200 elements are used in the fixture region. The Arcan test specimen mesh consists of 20 through thickness layers. The layer interfaces are located at distances of $Z = 0, 0.2635\text{mm}, 0.4727\text{mm}, 0.6387\text{mm}, 0.7704\text{mm}, 0.875\text{mm}, 0.958\text{mm}, 1.024\text{mm}, 1.076\text{mm}, 1.118\text{mm},$ and 1.15mm . For the slant crack case boundary conditions, the same displacement loading used for the flat crack case is applied at the upper loading nodes set while the corresponding nodes at the bottom are fixed in all directions. To eliminate any possible rigid body rotation, the mid-plane node of the upper loading nodes set is fixed in the x-direction. It should be noted that for the slant crack there is no symmetry condition about the mid-plane, in fact anti-symmetry conditions exist about that plane. Thus for the slant case the whole geometry is modeled.

II.4.3 Definition of Crack Opening Displacement

The crack opening displacement vector (CTOD or COD) is defined in this study as $\mathbf{v} = \delta_x \mathbf{e}_x + \delta_y \mathbf{e}_y + \delta_z \mathbf{e}_z$. In this work, all unit vectors are defined in the local coordinate system. Hence, δ_x is the COD local in-plane shearing or Mode II component, δ_y is the local opening or Mode I component and δ_z is the local tearing (out-of-plane shearing) or Mode III component. \mathbf{e}_x , \mathbf{e}_y and \mathbf{e}_z are the base vectors along the local x, y and z-directions respectively. δ_x is obtained by subtracting $U_x^+ - U_x^-$ while $\delta_y = U_y^+ - U_y^-$ and $\delta_z = U_z^+ - U_z^-$. Where U_x^+ , U_y^+ and U_z^+ are the displacements in the x, y and z directions at a certain distance behind the crack front at the crack top surface. U_x^- , U_y^- and U_z^- are the corresponding displacements at the crack bottom surface. The magnitude of the CTOD vector in this study is referred to as the total CTOD, δ_t , where $\delta_t = (\delta_x^2 + \delta_y^2 + \delta_z^2)^{1/2}$.

II.4.4 Results

Figure 42 presents the COD variations at both the mid-plane and front surfaces for slant crack specimen. Figure 43 presents a direct comparison of total COD for both flat and slant crack specimens. Figure 44 presents the radial distribution of constraint along an angle $\theta = 0^\circ$ with the crack front for both the flat crack and slant crack specimens. Figure 45 shows a comparison of the angular distributions in constraint for both the flat crack and the slant crack along a radial distance of $r = 0.272\text{mm}$ from the crack front. This figure shows that constraint values are higher at the mid-plane for a flat crack than for a slant crack of the same length. At the free surface, both flat and slant cracks have similar levels of constraint, where the surface constraint values are considerably lower than at the mid-plane.

II.4.5 Concluding Remarks

First, it is important to note that this study is directed towards understanding the crack tip fields for both flat and planar cracks under load. As such, the information obtained in this work is related to the "crack tip driving force", and not the functional form for a critical crack tip parameter.

Since it is generally believed that higher constraint suggests lower critical CTOD values, while lower constraint corresponds to higher critical CTOD values, the results of the current study show that

(a) for a slant crack loaded under pure Mode I remote loading, a significant local tearing COD component suggests that a slant crack promotes mixed mode I/III conditions.

(b) for a slant crack, the total CTOD is almost the same at the mid-plane and front and back surfaces. Actually, the total CTOD of the slant crack is slightly larger at the front and back surfaces than at the mid-plane, especially near the crack front.

(c) for a flat crack under pure Mode I remote loading, the total CTOD at the mid-plane is greater than at the front and back surfaces just behind the crack front,

(d) the mid-plane constraint is higher for a flat crack than for the slant crack, implying that flat cracks would tend to grow initially at the mid-plane, a phenomenon known as crack tunneling that is commonly observed in specimens undergoing planar fracture,

(e) a through-thickness variation of constraint exists for both flat and slant flaws, with the highest constraint at the mid-plane, providing the basis for the crack tunneling behavior observed in both flat and slant crack. For the slant crack, and since the through thickness variation is less than that of the flat crack, it is possible to say that tunneling would probably be less severe for the slant crack case,

(f) the increased effective stress, especially close to the crack front for the slant case, seems to suggest that for a slant crack, the effective stress might be considered as a driving force. The fact that the effective stress is almost the same at the specimen mid-plane and front and back surfaces for the slant crack suggests, that a shearing type of failure that is relatively uniform along the crack front is promoted

III. SIMULATION ALGORITHM DEVELOPMENT FOR THREE-DIMENSIONAL FRACTURE PREDICTIONS ALONG GENERAL FRACTURE SURFACES

III.1 General remarks

Based on the need to focus on the development of a fully three-dimensional fracture criterion along general surfaces, the following decisions were made.

1. A single program, ANSYS, was designated for PRE-processing of the input data and POST-processing of the output data.
2. the input/output procedure for ANSYS was completely re-written to correct numerous errors and a fully documented and verified interface written for ANSYS and the three-dimensional FE software package, CRACK3D
3. A USER MANUAL for CRACK3D with ANSYS has been written and we now are in the second draft of this manual.
4. A wide range of simple finite element analyses were performed with (a) CRACK3D and ANSYS and (b) ANSYS by itself. The results for all field

parameters were compared to document that the codes give nearly identical answers. Except for quantities near zero, all field variables were within 1%.

5. A methodology for using CRACK3D with ANSYS on a PC so that code can have up to 1.5 GB of RAM was developed, since ANSYS was unable to resolve problem.
6. A procedure for automatic re-meshing around flaws so that we can do full, 3D, unconstrained crack growth analyses, has been developed and is currently undergoing final testing.

III.2 General Structure and Capabilities of CRACK3D

An outline describing the structure of CRACK3D is shown in Figure 46. The CRACK3D code uses small or large deformation theory to model (a) elastic-plastic material response, (b) two or three-dimensional structures and (c) general three dimensional crack growth with user-defined crack growth criteria and tetrahedral elements.

III.3 Data transfer between meshes after crack growth

The transfer of history-dependent data from the old mesh to a new mesh includes two procedures. The first procedure is designated state variable smoothing. The second procedure is termed variable mapping. A least square smoothing method proposed by Hinton and Campbell [50] is used to perform state variable smoothing of variables such as stress and strain. In the smoothing scheme, nodal values are determined by minimizing the mean square difference between the interpolated values and the given elemental values. For the tetrahedral element with four nodes, we have

$$I = \sum_{j=1}^N \left(\int_{V_j} \left(\sum_{i=1}^4 \varphi_i \varepsilon_i - \eta_j \right)^2 dV \right) \quad (28)$$

where N is the total number of elements in the chosen region (local or global). φ_i is the shape function of an element. ε_i is the nodal value to be calculated and η_j is the value at the integrated point. The function, I , is minimized by taking the stationary value with respect to ε_i , i.e.

$$\frac{\partial I}{\partial \varepsilon_i} = 0 \quad \text{for } i=1, 2, 3, 4, \dots, n \quad (29)$$

where n is the total number of nodes in the chosen region. So, we have

$$\sum_{j=1}^N \left(\int_{V_j} \left(\sum_{i=1}^4 \varphi_i (\varphi_k \varepsilon_k - \eta_j) \right) dV \right) = 0 \quad (30)$$

ε_i can be calculated by solving the system of equations.

After determination of the state values at the current nodal locations, the values of the state variables are calculated at the integration points in the new mesh to complete the variable mapping process. Note that this process is required since the new mesh may have different element sizes and nodal locations, especially in the new crack tip region.

Suppose the coordinates of the new integration point is (x, y, z) . Then, the local coordinates (s, t, u) in the old element corresponding to the global coordinates (x, y, z) can be calculated according to the following equations.

$$\begin{cases} \sum_{i=1}^4 \varphi_i(s, t, u) x_i - x = 0 \\ \sum_{i=1}^4 \varphi_i(s, t, u) y_i - y = 0 \\ \sum_{i=1}^4 \varphi_i(s, t, u) z_i - z = 0 \end{cases} \quad (31)$$

So the state value ε of the new integration point is calculated as follows:

$$\varepsilon = \sum_{i=1}^4 \varphi_i(s, t, u) \varepsilon_i \quad (32)$$

III.4 Re-mesh for the 3D crack growth process

III.4.1 Local region re-mesh

To perform re-meshing, one is required to re-mesh both locally and globally. For local re-meshing, we first determine the geometric topology of region Ω on the base of initial mesh. Suppose S_Ω is the set of all boundary surfaces of Ω , L_Ω is the set of all boundary lines of all boundary surfaces of Ω

$$S_\Omega = \{S_i, S_i \in \Omega\}$$

$$L_\Omega = \{l_i, l_i \in \Omega\}$$

Ω_k ($k=1, 2, \dots, n$) is the sub-region around each crack front, whose size is controlled by the parameter R , where n is the total number of crack fronts in the structure.

Λ_R is the remnant of region Ω subtracted with Ω_k ($k=1, 2, \dots, n$), thus

$$\Omega = \Lambda_R \cup \Omega_1 \cup \Omega_2 \cup \dots \cup \Omega_n$$

Next, we determine the geometric topology of region Λ_R based on the initial mesh and the sets of L_Ω and S_Ω . Suppose S_Λ is the set of all boundary surfaces of Λ_R , L_Λ is the set of all boundary lines of all boundary surfaces of Λ_R

$$S_\Lambda = \{S_i, S_i \in \Lambda_R\}$$

$$L_\Lambda = \{l_i, l_i \in \Lambda_R\}$$

At this point, we investigate the relationship of sub-regions Ω_k ($k=1, 2, \dots, n$) and determine if any of the sub-regions intersects. If an intersection has occurred, we combine those sub-regions into a large sub-region.

After completing this process, we suppose there are m sub-regions \mathfrak{R}_k ($k=1, 2, \dots, m$) constructed after combination among the set of Ω_i ($i=1, 2, \dots, n$), accordingly

$$\Omega = \Lambda_R \cup \mathfrak{R}_1 \cup \mathfrak{R}_2 \cup \dots \cup \mathfrak{R}_m$$

We then determine the geometric topology of region \mathfrak{R}_k ($k=1, 2, \dots, m$) based on the initial mesh and the sets of L_Ω and S_Ω . Suppose $S_{\mathfrak{R}_k}$ is the set of all boundary surfaces of \mathfrak{R}_k , $L_{\mathfrak{R}_k}$ is the set of all boundary lines of all boundary surfaces of \mathfrak{R}_k , which are expressed mathematically

$$S_{\mathfrak{R}_k} = \{S_i, S_i \in \mathfrak{R}_k\} \quad (k=1, 2, \dots, m)$$

$$L_{\mathfrak{R}_k} = \{l_i, l_i \in \mathfrak{R}_k\} \quad (k=1, 2, \dots, m)$$

$\Theta_{\mathfrak{R}_k}$ is the set of all boundary surfaces of $S_{\mathfrak{R}_k}$, $\nabla_{\mathfrak{R}_k}$ is the set of all boundary lines of all boundary surfaces of $L_{\mathfrak{R}_k}$ ($k=1, 2, \dots, m$) which will be re-meshed

$$\Theta_{\mathfrak{R}_k} = S_{\mathfrak{R}_k} - S_{\mathfrak{R}_k} \cap S_\Lambda \quad (k=1, 2, \dots, m)$$

$$\nabla_{\mathfrak{R}_k} = L_{\mathfrak{R}_k} - L_{\mathfrak{R}_k} \cap L_\Lambda \quad (k=1, 2, \dots, m)$$

To perform the re-meshing, we propose to use a parametric transformation, mapping 3D physical surface into parametric plane (u, v), re-meshing in the parametric plane (u, v), and eventually doing the inverse transformation to map the surface from parametric plane to physical surface.

After all lines in $\nabla_{\mathfrak{R}_k}$ and all surfaces in $\Theta_{\mathfrak{R}_k}$ have been re-meshed, we then re-mesh the sub-region \mathfrak{R}_k ($k=1, 2, \dots, m$).

Next, we combine the new mesh in regions \mathfrak{R}_k ($k=1, 2, \dots, m$) and the old mesh in region Λ_R . Taking account of the old mesh in region Λ_R , renumber the new nodes

and elements created in regions \mathfrak{R}_k ($k=1, 2, \dots, m$). Both the old mesh in region Λ_R and the new mesh in regions \mathfrak{R}_k ($k=1, 2, \dots, m$) construct the current mesh.

Then, data transformation from old mesh to current mesh is performed as per section V.1.. Note that this process will be done only in the regions \mathfrak{R}_k ($k=1, 2, \dots, m$), with data in the region Λ_R unchanged. Finally, geometric topology of Ω is updated for use in the next re-meshing process.

III.4.2 General methods developed in our study

When generating a mesh along crack fronts, there will be two or more nodes with the same coordinates on crack surfaces. This problem has been discussed in literature [51]. Unfortunately, the method proposed in [51] is not a general method for nodes on boundary lines of crack surface. Based on our study, a more general method has been developed and implemented in CRACK3D.

Node selection on lines

Without loss of generality, suppose segment GH is on the current generating front, which requires connection to a companion node on another line. Suppose node A and node B have the same coordinates and are located on different boundary lines and node B lies on the same side of segment GH, as shown in Figure 47. Nodes C and D are the two neighbors of node A and nodes E and F are the two neighbors of node B.

The following procedure was developed to select a node from nodes A and B which will be connected to segment GH.

1. Define the following unit vectors originally from node A and node B

V_{A1} is unit vector from A to C

V_{A2} is unit vector from A to D

V_{B1} is unit vector from B to E

V_{B2} is unit vector from B to F

2. Perform the dot product between two unit vectors

$$V_{Ai} \bullet V_{Bj} \quad (i=1, 2. \quad j=1, 2)$$

3. Determine the vectors having maximum value for the dot product and suppose that $V_{AD} \bullet V_{BF} = \max \{V_{Ai} \bullet V_{Bj} \quad i=1, 2. \quad j=1, 2\}$
4. Establish outward-normal unit vectors V_A and V_B at node A and node B that are perpendicular to segments AD and BF, respectively.
5. Perform the dot products

$$V_{MB} \bullet V_A$$

$$V_{MB} \bullet V_B$$

where V_{MB} is unit vector from middle point of segment GH to node B (or node A)

6. Then, if $V_{MB} \bullet V_A > V_{MB} \bullet V_B$, node A is selected to connect to segment GH. However, if $V_{MB} \bullet V_A < V_{MB} \bullet V_B$, then node B is selected to connect to segment GH

Node selection on crack surfaces

Without loss of generality, suppose a facet CDE is on the current generating front which is looking for a node to be connected, suppose node A and node B have the same coordinates and on different crack surfaces and node B lies on the same side of facet CDE, as shown in Figure 48.

The following procedure was developed to select a node from nodes A and B which will be connected to facet CDE.

1. Define the element neighbor of node A on the boundary surface Ψ as each triangular element on surface Ψ connecting to node A
2. Suppose node A has N_A surface element neighbors, node B has N_B surface element neighbors.
3. Define unit vector V_{Aj} as the out-normal unit vector of boundary surface node A lies that is perpendicular to the j^{th} element neighbor of node A.
4. Define unit vector V_{Bj} as the out-normal unit vector of boundary surface node B lies on which is perpendicular to the j^{th} element neighbor of node B.
5. Perform the dot product between each two unit vectors

$$V_{Ai} \bullet V_{Bj} \quad (i=1, 2, \dots N_A. \quad j=1, 2, \dots N_B)$$

6. Determine the vectors having minimum value for the dot product and suppose

$$V_{Ak} \bullet V_{Bl} = \min \{ V_{Ai} \bullet V_{Bj} \quad i=1, 2, \dots, N_A, \quad j=1, 2, \dots, N_B \}$$

7. Performing the dot products and doing comparison

$$V_{MB} \bullet V_{Ak}$$

$$V_{MB} \bullet V_{Bl}$$

where V_{MB} is unit vector from center of facet CDE to node B (or node A)

8. Then, if $V_{MB} \bullet V_{Ak} > V_{MB} \bullet V_{Bl}$, node A is selected to connect to facet CDE
9. However, if $V_{MB} \bullet V_{Ak} < V_{MB} \bullet V_{Bl}$, then node B is selected to connect to facet CDE

III.5 Re-meshing Process

To perform the re-meshing outlined above, the following subroutines have been completed to make the process fully automatic for general 3D mesh regeneration. It is noted that the decision has been made to use tetrahedral elements throughout the re-meshing region.

1. software to collect topologic information of geometry for each sub-region based on the global structural topologic information of geometry, determining the property of each boundary surface and indicating which one needs to be re-meshed and which one does not need,
2. software to collect the surface triangular elements on each boundary surface of the sub-region under consideration,
3. software to determine the outer loop and the interior loops (if existing) on each boundary surface of the sub-region under consideration.
4. software to modify the loops on each boundary surface of the sub-region taking account of the change of topology due to crack propagation,
5. software to investigate the boundary lines each loop consists of, and determining the property of each boundary line. (e.g. the lines on the interface will not be remeshed)
6. software to re-mesh the loops on each boundary surface of the sub-region based on the properties of all boundary lines.

In addition to these subroutines, CRACK3D has been modified so that the following tasks will be automatically performed after each new loading increment is applied and the fracture criterion is satisfied so that the crack is required to propagate in a specific direction.

1. Determine the local region to be re-meshed around the new crack front
2. Investigate the feature of the local region (e.g. boundary surfaces, boundary lines, interface with the remainder)
3. Re-mesh the local region based on mesh density distribution and boundary features of the local region.
4. Convert the database from old mesh to new mesh.
5. Delete the old mesh in the local region, re-order the node number and element number and optimize the database.
6. Due to the errors induced in the process of data conversion and crack propagation, check the equilibrium equations and find out the current non-equilibrium nodal force. Invoke a local sub-iteration loop to eliminate the non-equilibrium nodal force.

It is noted that all the calculations will be fulfilled in the new mesh until the next re-mesh. Figure 49 shows the results of the process described above, where the crack tip region is identified, extracted, re-meshed and then re-inserted into the unaltered "far-field" mesh. It is noted that the outer boundary of the local region (i.e., the interface surface) is unaltered during the re-meshing so that the reinsertion process can be completed without any alterations to the "far-field" mesh.

III.6 Optimization of Mesh in Three-Dimensional Domain after Re-meshing

The goal of mesh optimization is to locally and globally improve the quality of the mesh by eliminating elements that have a poor aspect ratio or other dimensional defects. To investigate and evaluate mesh quality, an element quality factor is defined, and the overall objective function for mesh optimization is the element quality so that mesh irregularities can be identified and eliminated. To achieve this goal, each element in the mesh will be evaluated during the process of mesh optimization.

When generating tetrahedral elements in a three-dimensional domain using Advancing Front Techniques (AFT), the first step is discretization of the boundary surfaces using triangular elements. Next, all triangular elements on the boundary surfaces of the domain will define the initial front to be used to initiate volumetric mesh generation. Therefore, the qualities of surface elements will have a strong influence on the tetrahedral elements to be generated. For this reason, optimization of surface triangular elements will be performed prior to volume discretization.

In general, it has been shown by many investigators that 3-D surface mesh optimization is far more complicated than either 2-D mesh generation or 3-D volume mesh optimization. To demonstrate this, it is noted that during surface mesh generation, each node movement and element improvement must be performed in a local tangent plane and also globally constrained onto the original boundary surface. *In our work, a new method of 3-D surface mesh optimization has been developed and applied in our code.*

In surface mesh and volume mesh optimization, there is a general problem, which appears occasionally and results in invalid elements with negative areas and volumes in the process of node movement. An empirical method was suggested [62,63] to decrease the chances that this problem will occur. A major disadvantage of this approach is that it will significantly increase processing time. Another disadvantage of this approach is that it does not solve the problem, but only decreases the chances that the problem will occur. *We have developed a method for completely eliminating this possibility and have implemented it in the current version of the algorithm.* Some of the technical issues are outlined in the following sections.

III.6.1 3-D surface mesh optimization

Two definitions are used frequently in this note

Element neighbor of node A: If element E contains node A , then element E is called as an element neighbor of node A .

Node neighbor of node A: If element E contains node A , then all the nodes in element E except node A are called as the node neighbors of node A .

Using these definitions, there are several key steps in the 3D mesh optimization process that we have implemented. The first is to optimize the surface meshes on the surfaces of the volume to be discretized.

III.6.1.1 Surface mesh optimization for 3D volume

As note above, the first part of the process for optimizing a 3D mesh in a volume is to optimize the surface mesh. There are several key steps in the surface mesh optimization process that we have implemented. They are designated (a) node examination, (b) edge examination and (c) surface mesh smoothing.

Node examination

In this process, all of the nodes on the surface mesh are considered, one by one. Suppose A is an arbitrary node on the surface of the 3D region. Then, if $N_A = 3$ (the number of triangular element neighbors of node A on all boundary surfaces), node A will be deleted. This process is shown in Figure 50.

Edge examination

In this process, all of the edges on the surface mesh are considered, one by one. As shown in Figure 51, suppose edge AB is an arbitrary edge in surface mesh. If N_A , N_B , N_C and N_D are the numbers of triangular elements connecting to node A , node B , node C and node D , respectively, and $(N_A + N_B) - (N_C + N_D) > m$, then edge AB will be replaced by edge CD , where the parameter $m=4$ is used in our code.

Surface mesh smoothing

Here, a new 3-D surface mesh smoothing technique is proposed in our work. When performing mesh smoothing on a 3-D surface, each node movement must be constrained to remain on its corresponding spatial surface. That is, node movement must be constrained in a local tangent plane and its final location must also be on the original spatial surface.

Without loss of generality, suppose node A is an arbitrary node on a 3-D boundary surface, and there are m node neighbors for node A so that $\{N_i, i=1, 2, \dots, m\}$. Define

1. V_{Ai} as the location vector of the i^{th} node neighbor of node A in global coordinate system ($i=1, 2, \dots, m$)
2. V_A as the location vector of node A,
3. Φ_{Ai} is the weighted function at node N_i with respect to node A ($i=1, 2, \dots, m$), which is a function of mesh density at nodes N_i and A, where $\Phi_{Ai} = f(d_A, d_i)$ $i=1, 2, \dots, m$ and where d_A and d_i are the mesh density at nodes A and N_i , respectively,
4. N_A as the out-normal unit vector of the 3-D surface at node A, then one has

Then by defining the following vectors

$$S_{Ai} = \frac{(V_{Ai} - V_A) \times N_A}{\|(V_{Ai} - V_A) \times N_A\|} \quad i=1, 2, \dots, m$$

$$T_{Ai} = N_A \times S_{Ai} \quad i=1, 2, \dots, m$$

We have a new location vector V_A^{new} of node A that can be expressed as

$$V_A^{\text{new}} = V_A + \frac{\sum_{i=1}^m \Phi_{Ai} \|V_{Ai} - V_A\| T_{Ai}}{\sum_{i=1}^m \Phi_{Ai}}$$

To avoid introducing invalid elements with negative areas due to node movement, various methods and criteria for guaranteeing reasonable modification on 3-D surfaces have been implemented in our optimization code.

III.6.1.2 Volume mesh optimization

Processes that are similar to those used for surface mesh optimization are implemented. The technical issues for volume mesh optimization are listed as follows

Node examination

Sweeping all the nodes in the domain in turn. Suppose A is an arbitrary node, if $N_A = 4$, then node A will be deleted, where N_A is the number of tetrahedral element neighbors of node A. (Figure 52).

Edge examination

Procedures are nearly identical to ones used for surface mesh smoothing

Element facet examination

Procedures are nearly identical to ones used for surface mesh smoothing

Volume mesh smoothing

Visiting all the nodes in turn, and performing mesh smoothing for each reasonable node movement. The laplacian smoothing method is used here

$$V_A^{new} = V_A + \frac{\sum_{i=1}^m \Phi_{Ai} (V_{Ai} - V_A)}{\sum_{i=1}^m \Phi_{Ai}} \quad (5)$$

To avoid introducing invalid elements with negative areas due to node movement, some techniques and criteria for reasonable modification have been used in our optimization code instead of the method proposed in literature [51]. The numerical results show that it takes less CPU time in mesh smoothing by using our method than that proposed in [52].

Figure 53 shows two examples of the effect of smoothing on the overall quality of both (a) a surface mesh and (b) a volumetric mesh.

III.7 Recent Enhancements in CRACK3D Simulation Code

Considering the application of CRACK3D in real-life structural analyses, some work has been done to speed up the code. Additionally, more options and special data output make the code more powerful and more convenient for users to use.

1. Enhance the capacity of User-Controlled update of [K]
2. Add a frequency parameter for controlling writing results to third-party software (e.g., ANSYS)
3. Provide two approaches for handling the plastic strain effect in the global equilibrium equations.
4. Enhance the capacity that a crack front can evolve by two different ways, one is to evolve node by node; the other is to evolve with the entire crack front simultaneously. This option can apply to ANY CASE.
5. Stop automatically at a specified external load number given by user for ANY CASE.
6. Stop automatically when total crack growth increment at specified master node position is equal to or just greater than a specified crack increment for ANY CASE.
7. Stop automatically when any one of crack fronts touches the specified node on the crack path for the case of NODE RELEASE.
8. Display reaction force using ANSYS.
9. Output crack front shape at each loading step.
10. Output load-versus-crack increment at each loading step (conditionally)
11. Output load-versus-displacement at a specified node position.
12. Text file "CRACKFR.TXT" records the crack front shape and the corresponding loads at some special loading steps just before the next crack growth
13. Text file "CRACKGR.TXT" records the total crack growth increment at master node position and the corresponding loads at some special loading steps just before the next crack growth

14. Text file "CRACKLD.TXT" records the displacement and the corresponding loads at a specified node at some special loading steps just before the next crack growth.

IV. Experimental Studies

IV.1 Experimental Study of Crack Growth in Thin Sheet Material under Tension-Torsion Loading

IV.1.1 Background

To validate computational models and assess the viability of using a critical COD stable tearing criterion for flaws in 2024-T3 aluminum experiencing tension stresses (S_p) and torsion stresses (S_T), a complete set of experimental measurements for (a) critical COD during crack growth under nominal tension-torsion loading, (b) the evolution of crack path with crack growth and (c) crack surface shape as a function of loading have been obtained. Data from this work will provide an important experimental database for use in assessing the predictive capability of advanced, three-dimensional, crack growth simulation tools.

IV.1.2 Specimen Configuration and Test Procedure

Figure 54 provides a schematic of typical specimen geometry. The specimens were machined from 2024-T3 aluminum and fatigue pre-cracked in the LT orientation so that the initial $a/w = 0.0833$. All tests were performed on a 50 Kip MTS test frame using an MTS Testar system with PID controller and user-generated control programs. To perform each experiment, the following procedure was employed. First, axial displacement was used to control load application to the specimen. During the loading process, output from the axial load cell was input to the torsion actuator to generate a proportional, applied torque. Finally, torsional rotation is increased until the required torque was attained.

Since three channels of input were used to control the test process, it was necessary to set appropriate tuning factors for all three channels of input to ensure stability of the system for the type of specimen being tested. In this regard, it is noted that the control process described above was slightly unstable at low levels of applied loading, being fully stable for loads greater than 400 N. Defining representative global elastic stresses in thin rectangular sheets under torsion and tension by $S_T = 3T (t^2 w)^{-1}$ and $S_P = P (t w)^{-1}$, respectively, where t is the specimen thickness and w is the specimen width, experiments were performed at five levels of S_T/S_P in the range $0.0 \leq S_T/S_P \leq 6.64$. In this work, complete results are reported for $S_T/S_P = 0, 1.66$ and 6.64 and partial results are provided for $S_T/S_P = 3.32$ and 4.98 .

To accurately quantify COD in the region 1mm behind the crack tip, the process of three-dimensional digital image correlation (DIC-3D) [53-56] was used to obtain stereo images of a region around the moving crack tip that is approximately 4mm by 4mm in size (see Figure 55). Due to both the high magnification required and the need to follow the moving crack tip, special considerations were used when setting up the two-camera system. In particular, (a) both cameras were mounted to a cross member that was specifically designed for maximum rigidity to minimize relative motion between the two cameras during the experiment, (b) digitally-controlled stepper motors were used to move the rigid cross member, thereby reducing the potential for inducing relative motion between the cameras during camera translation, (c) specially design lens mounts were used to reduce lens motion during the experiment and (d) special care was used to align the sensor plane of the camera so that is was perpendicular to the direction of translation stage motion for calibration.

Achieving approximate perpendicularity of the sensor plane required that an iterative process be performed. First, shims were applied between the camera mount and the translation stage to rotate the sensor plane. Secondly, images were acquired before and after translation along the optical axis. Thirdly, using the resulting displacement fields as an indicator of alignment (the presence of a pure dilation field indicates alignment), shim locations were altered until acceptable alignment was achieved. Calibration of the system demonstrated that the overall accuracy of the system was approximately 1 micron in each component of displacement.

After completing the alignment process, image data was acquired as follows. First, the DIC-3D system was calibrated using procedures described previously [53-56]. Secondly, after calibration, a series of overlapping images of 4mm by 4mm areas located approximately 38 mm ahead of the initial crack position are acquired prior to loading. To obtain this series of images, the entire camera system was physically moved to the appropriate location along the anticipated crack path using an x-y-z translation stage.

Once initial images were obtained, the camera system was translated to observe the initial crack tip region. During loading, images were acquired of the crack tip region. This process continued, even during crack growth. To maintain focus on the crack tip region, the rigid bar was translated and rotated during crack growth so that COD and surface strain fields could be computed during the growth process.

IV.1.3 Fracture Surface Measurements

Inspection of the fracture surfaces from the tension-torsion tests indicated that the initially flat fatigue crack rapidly transitioned to a slant fracture surface. Since the goal of these studies is to develop an improved understanding of the fracture process in the tension-torsion specimens, the shape of the fracture surface was measured accurately for each S_T/S_P . Once measured, the data for the actual crack surface shape will be used in detailed finite element analyses to provide critical insight into the evolution of the stress and strain fields in the crack tip region prior to, and during, the crack propagation process.

To obtain these measurements, a novel, high accuracy, fringe projection system [57] was used to obtain full-field (X,Y,Z) positions for the entire fracture surface. To optimize the accuracy of the measurements across the entire fracture surface, two overlapping regions of the fracture surface were measured independently. The overlap regions were used to combine two measurement sets into a single data cloud for the entire fracture surface. The estimated standard deviation for the spatial position measurements at each point in the measurement field is approximately 10 microns.

The resulting surface profiles for the complete fracture surface after combining two separate data sets using the procedures described above are shown in Figure 56 for $S_T/S_P = 0.0, 1.66$ and 6.64 .

Figure 57 graphically presents the evolution of crack slant angle with crack growth $S_T/S_P = 0.0, 1.66$ and 6.64 . In each case, slant angle was determined by performing linear regression on the height data (approximately 30 points per line) every 0.20 mm along the fracture surface.

IV.1.4 COD Measurements

COD was measured throughout the crack growth process for all S_T/S_P values by computing the relative, three-dimensional displacement vector for subsets above and below the crack line that are located approximately one millimeter behind the current crack tip. Figure 58 presents all of the COD measurements from the tension-torsion tests, along with a horizontal line representing the mean value for the COD data for all $\Delta a > 10$ mm.

IV.1.5 Crack Tunneling Measurements

As slant crack growth progresses, crack tunneling is occurring simultaneously. To assess the level of crack tunneling, the procedure outline by Dawicke et al [7] was used to obtain trends in through-thickness crack extension. Fatigue pre-cracking was performed to obtain a sharp crack with minimal crack tip plasticity. Using baseline tests to determine when crack growth initiated for each S_T/S_P ratio, each specimen was loaded under combined tension-torsion until either interior stable tearing was predicted to occur or a pre-specified amount of surface crack growth was observed. At this point, a change in loading mode was performed and tensile fatigue loading was applied to mark the stable tearing crack front. Metallographic analysis of the fracture surface in a scanning electron microscope was performed to measure crack front shape. A total of eight separate specimens were tested to increasing levels of tension and torsion so that trends in crack tunneling could be measured.

Figure 59 presents crack front data for $S_T/S_P = 0.0, 1.66$ and 6.64 . Figure 60 presents a non-dimensional measure of crack tunneling for each ratio S_T/S_P as a function of the amount of crack growth.

IV.1.6 Concluding Remarks

It is noted that previous Mode I/II [2-6] results and our Mode I/III results are consistent with experimental observation of the active micro-mechanisms during mixed mode fracture [58-61] and results from previous numerical simulations of the fracture process [62,63]. In essence, the processes of micro-void growth and shear band formation compete to dominate the fracture process. For local tensile conditions, void nucleation and growth from large particles is generally recognized as being a primary mechanism for fracture. In this case, the void growth region is under locally Mode I conditions, opening deformation controls crack tip opening and the COD_{\perp} component of COD is dominant [2-6]. For local shear conditions, nucleation and growth from small particles that result in void sheeting and shear localization has been identified as the primary mechanism for fracture. In this case, the process zone is under Mode II or Mode I/III conditions and the shear component of COD is the dominant crack tip opening deformation.

Recent fracture experiments of riveted aluminum panels [64] performed at the FAA Technical Center under internal pressure loading exhibited both fatigue crack growth and stable tearing. In both modes of crack growth, slant fracture was observed throughout the crack growth process. Of primary significance in the FAA experiments was the observation that stable tearing between rivets in the panel occurred in a manner that was nearly identical to that seen in these tension-torsion experiments; the fracture surfaces tended to interfere during crack growth and mode III conditions appeared to be a significant part of the local deformations. Therefore, understanding the complex fracture behavior in the tension-torsion specimens should provide the foundation for predicting stable crack growth behavior in thin aircraft structures.

Finally, experimental evidence and initial finite element analyses suggests that a critical COD is a quantitative measure of the processes occurring in the crack tip region

that lead to fracture for mode I/II conditions. Due to the complexity of the mixed mode I/III crack growth process, accurate simulation of the fracture process requires the development of novel, robust simulation algorithms capable of predicting the evolution of complex, three-dimensional crack front shapes using general fracture criteria. Given the exponential growth of computational capabilities in recent years, it is simply a matter of time until the required simulation tools are developed. Once developed, the experimental data presented in this work will provide a basis for identifying and quantitatively verifying those fracture criteria capable of predicting ductile crack growth under complex loading conditions.

IV.2 Small specimen tests for void growth measurements

The goal of this work is to obtain a relationship between void formation and stress state for AL 2024-T3. As part of this work, finite element analyses have been completed to determine the range of constraint levels present in a small, notched cylindrical specimen. In addition, as described in the following section, a series of experiments have been performed to determine whether void growth processes can be observed in small, notched cylindrical specimens. In addition, an in-plane shear specimen has been developed and will be used to relate void growth to the applied shear stress state.

IV.2.1 Notched cylindrical specimen tests

Figure 61 shows the notched cylindrical tensile specimens that are being tested. Two of the specimens for each geometry and direction (longitudinal and transverse to the rolling direction) were loaded until failure and the load at failure recorded. As shown in Table 1, subsequent specimens have been loaded to different percentages of those failure loads.

Table 1

Specimen	Failure Load (lbs)	Maximum Load (lbs)	Percentage
F Transverse	2315	2189	94.6
F Longitudinal	2345	2110	90.0
H Transverse	1962	1754	89.4
H Longitudinal	1945	1762	90.6

Figure 62 shows an optical micrograph for a polished specimen taken from the transverse F specimen. There is clear evidence of particle fracture and micro-void initiation in Figure 62, but no large micro-voids were detected in these specimens. Since the fracture and debonding of inter-metallic particles are precursors to full-scale void formation, the specimens will also be examined using a scanning electron microscope to check for evidence of de-bonding between the aluminum matrix and the inter-metallic particles.

Since Table 1 shows that the maximum tensile load for void growth studies in specimens F and H is considerably below the failure load, and the void growth process is known to be exponential in nature near maximum load, a 5000 pound load cell has been purchased to replace the previously-used 20,000 pound load cell. Together with modifications to the control software, the load resolution is increased by 20-fold with a goal of improving ability to stop an experiment at 99.5% of the maximum load so that sectioning can be performed and voids clearly identified.

IV.2.2 Development of a shear specimen

To obtain voids under nominally shear loading, a new shear specimen has been designed to allow examination of regions just ahead of crack tip as crack extension occurs. Figure 63 shows a diagram of the new specimen. The groove depth of the 9.5mm 2024 plate is 3mm, and the 6.35mm thick, 2524 plate has a groove depth of 1.9mm. The specimens were designed to fail by shear in the grooves before yielding in the tongues.

Like the notched cylindrical tensile specimens, shear specimens were made in both directions (transverse and longitudinal to the rolling direction) from both materials. Initial testing shows a fracture surface with some shear features, but also some tensile features. Some minor design changes are being considered to increase the prevalence of the shear mode in the groove region. The experimental plan for the shear specimens is also similar to the tensile specimens.

V Summary

The broad objectives of this project are to (a) develop the theoretical foundation for the development of a continuum-based, general stable crack growth criterion in ductile materials, (b) develop a computational methodology for implementing the criterion to predict stable tearing along a general path in three-dimensions, (c) develop an initial experimental data base for validation of the predictive methodology and (d) develop and validate a mixed mode fracture criterion using the initial experimental data base and completed computational methodology.

First, detailed theoretical and computational studies of void growth have been completed that show (a) for each initial void volume, a functional relationship exists between the mean stress σ_{mean} and effective stress σ_{eff} at the instant of void link-up and crack growth, demonstrating that a two-parameter fracture criterion is viable for predicting stable tearing and (b) the experimentally observed link between plastic strain

and mean stress further indicates that there is the basis for obtaining a critical crack opening displacement (COD) as a function of mean stress, that is, $COD(\sigma_{mean})$.

Second, a fully functional three-dimensional crack growth algorithm has been developed that is capable of predicting crack growth along a general, three-dimensional surface. The algorithm, designated CRACK3D, utilizes the Pre and Post processing capabilities of Ansys while performing all of the crack-front calculations internally. As part of the development process, (a) improved methods for crack tip re-meshing have been developed and implemented which only re-mesh a region around the current crack tip and (b) new approaches for volumetric and surface optimization have been developed and implemented. As part of the development process, detailed simulations have been performed to complete the debugging process.

Third, a set of controlled mode I, mixed mode I/II and mixed mode I/III experiments have been completed for aluminum 2024-T3. These experiments included (a) fatigue marking to identify the surface crack front, (b) three-dimensional non-contacting measurements to quantify the shape of a complex, slanted fracture surface and (c) measurements of surface COD during stable tearing. In addition to these experiments, a set of experiments have been attempted to related the combination of stresses, σ_{mean} and σ_{eff} , in a region to the presence of actively growing voids. Here, the goal of the experiments is to provide quantitative evidence for defining a portion of the relationship between σ_{mean} and σ_{eff} for 2024-T3 aluminum

VI. REFERENCES

1. Committee on Aging of U.S. Air Force Aircraft, National Materials Advisory Board, "Aging of U.S. Air Force Aircraft: Final Report", 1997, Publication No. NMAB-488-2, National Academy Press.
2. Amstutz, B.E., Sutton, M.A., Newman, J.C., Jr. and Dawicke, D.S., "Effects of Mixed Mode I/II Loading and Grain Orientation on Crack Initiation and Stable Tearing in 2024-T3 Aluminum", ASTM STP 1296, 27, 105-126 (1997).
3. Sutton, M.A., Zhao, W., Boone, M.L., Reynolds, A.P. and Dawicke, D.S., "Prediction of Crack Growth Direction for Mode I/II Loading Using Small-Scale Yielding and Void Initiation/Growth Concepts", International Journal of Fracture, 83, 275-290 (1997).
4. Amstutz, B. E., Sutton, M. A., Dawicke, D. S. and Newman, J. C., Jr., An Experimental Study of CTOD for Mode I/ II Stable Crack Growth in Thin 2024-T3 Aluminum Specimens, *Fracture Mechanics*, ASTM STP 1256, 256-271 (1995a).
5. Amstutz, B. E., Sutton, M. A., Dawicke, D. S. and Newman, J. C., Jr., Effects of mixed mode I/II loading and grain orientation on crack initiation and stable tearing in 2024-T3 aluminum specimens, *Fatigue and Fracture*, ASTM STP 1296, 105-125 (1995).
6. Dawicke, D.S., Newman, J.C., III, Sutton, M.A. and Bigelow, C., "Orientation Effects on the Measurement and Analysis of Critical CTOA in an Aluminum Alloy", ASTM STP 1256, 26, 243-256 (1995).
7. Dawicke, D.S. and Sutton, M.A., "CTOA and Crack Tunneling Measurements in Thin Sheet 2024-T3 Aluminum Alloy", *Experimental Mechanics*, 34 (4), 357-369 (1994).
8. Wells, A. A. "Unstable crack propagation in metals: Cleavage and fast fracture," in *Proceedings of the Cranfield Crack Propagation Symposium*, 1,, 210-230 (1961).
9. Wells, A. A. "Application of fracture mechanics at and beyond general yielding," *British Welding Journal*, 11, 563-570 (1963).
10. Andersson, H. "A finite element representation of stable crack growth," *Journal of the Mechanics and Physics of Solids* 21, 1973, pp. 337-356.

11. de Koning, A. U. "A contribution to the analysis of quasi-static crack growth in sheet materials," in *Fracture 1977, Proceedings of the 4th International Conference on Fracture*, 3, 25-31 (1977).
12. Kanninen, M. F., Popelar, C. H., and Broek, D. *Nuclear Engineering and Design* 67, 27-55 (1981).
13. Rice, J. R. and Sorensen, E. P. "Continuing crack-tip deformation and fracture for plane strain crack growth in elastic-plastic solids," *Journal of the Mechanics and Physics of Solids* 26, 163-186 (1978).
14. Newman, J. C., Jr., Booth, B. C., and Shivakumar, K. N. "An elastic-plastic finite element analysis of the J-resistance curve using a CTOD criterion," *Fracture Mechanics: 18th Symposium*, ASTM STP 945, 665-685 (1985).
15. Dawicke, D. S., Sutton, M. A., Newman, J. C., Jr., and Bigelow, C. A. "Measurement and analysis of critical CTOA for thin-sheet aluminum alloy materials," presented at the 25th National Symposium on Fracture Mechanics, Bethlehem, PA, June (1993).
16. Bakuckas, J. B. and Newman, J. C., Jr. "Prediction of stable tearing of 2024-T3 aluminum alloy using the crack-tip opening angle approach," NASA Technical Memorandum 109023, NASA Langley Research Center, September (1993).
17. Deng, X. and Newman, J. C., Jr. "ZIP2DL – An elastic-plastic, large-rotation finite-element stress analysis and crack-growth simulation program," NASA Technical Memorandum 110332, NASA Langley Research Center, April (1997).
18. Deng, X. and Newman, J. C., Jr. "Implementation and application of a large-rotation finite element formulation in NASA code ZIP2DL," *Proceedings of the FAA-NASA Symposium on Continued Airworthiness of Aircraft Structures* (Atlanta, Georgia, August 28-30, 1996), DOT/FAA/AR-97/2, II, 377-390 (1997).
19. Sutton, M. A., Zhao, W., Deng, X., Dawicke, D. S., and Newman, J. C., Jr. "Numerical investigations into the viability of CTOD as a fracture parameter for mixed-mode I/II tearing of thin aluminum sheets," *Proceedings of the FAA-NASA Symposium on Continued Airworthiness of Aircraft Structures* (Atlanta, Georgia, August 28-30, 1996), DOT/FAA/AR-97/2, II, 461-472 (1997).
20. Deng, X. and Newman, J. C., Jr. "ZIP2DL: A finite element code for stress analysis and crack growth simulation," *invited presentation* at the NASA Airframe Structural

Integrity Program Meeting, NASA Langley Research Center, Hampton, Virginia, April 17-18, (1997).

21. Dawicke, D. S. "Residual strength prediction using a CTOA criterion," Proceedings of the FAA-NASA Symposium on Continued Airworthiness of Aircraft Structures (Atlanta, Georgia, August 28-30, 1996), DOT/FAA/AR-97/2, II, 555-566 (1997).
22. Deng, X., Sutton, M. A., and Newman, J. C., Jr. "Simulation and analysis of mixed-mode stable crack growth in elastic-plastic thin sheets," Joint ASME/ASCE/SES Summer Meeting, 1997, Northwestern University, Evanston, Illinois, June 29-July 2 (1997).
23. Deng, X. and Newman, J.C. Jr., "Crack growth simulation with a mixed-state-of-stress approach: A comparison of effects of moving and fixed plane strain cores," presented at the Fourth US National Congress on Computational Mechanics, San Francisco, California, Aug. 6 - 8 (1997).
24. Thomason, P.F., "A view on ductile fracture modeling", *Fatigue and Fracture of Engineering Materials*, 21 1105-1122 (1998).
25. Ma F, Sutton MA, Deng X, "Plane Strain Mixed Mode Crack-Tip Stress Fields Characterized by A Triaxial Stress Parameter and A Plastic Deformation Extent Based Characteristic Length", *J. Mech. Phys. Solids*, 49 2921-2953 (2001).
26. Thomason, P.F., *Ductile fracture of metals*, Pergamon Press (1990)
27. McClintock, FA, "A criterion for ductile fracture by the growth of holes", *ASME J. Appl. Mech.*, 35, 363-371 (1968).
28. Goods, S. H. and Brown, L.M., *The Nucleation of Cavities by Plastic Deformation*, *Acta Metallurgica*, 27,1-15 (1979).
29. Gurson, A. L., *Continuum theory of ductile rupture by void nucleation and growth*, *J. Engng. Mater. Tech.* 99, 3-15 (1977).
30. Argon, A.S. and Im, J. and Safoglu, R., *Cavity formation from inclusions in ductile fracture*, *Metall. Trans.* 6A, 825-837 (1975).
31. Argon, A.S. and Im, J., *Separation of second phase particles in spheroidized 1045 steel, Cu-0.6%Cr alloy, and maraging steel in plastic straining*, *Metall. Trans.* 6A, 839- 851 (1975).

32. Rice, J. R. and Tracey, D. M, On the ductile enlargement of voids in triaxial stress fields, *J. Mech. Phys. Solids*, 17, 210-217 (1969).
33. ABAQUS Users Manual 5.8, 1998, Hibbitt, Karlsson and Sorensen Inc, Providence, Rhode Island.
34. Larsson, S. G., Carlsson, A. J., Influence of Non-singular Stress Terms and Specimen Geometry on Small-Scale Yielding at Crack Tip in Elastic-Plastic Materials, *J. Mech. Phys. Solids*, 21, 263-278 (1973)
35. Du. Z. Z., Betegon, C. and Hancock, J. W., J-dominance in mixed mode loading, *Int. J. Fract.*, 52, pp191-206 (1991)
36. Ma, F., Deng, X., Sutton, M. A. and Newman, J.C., Jr., A CTOD Based Mixed Mode Fracture Criterion, *Mixed Mode Crack Behavior, ASTM STP 1359*, pp-86-110 (1999)
37. Bose, K. and Ponte Castaneda, P., Stable Crack growth under Mixed-Mode Conditions *J. Mech. Phys. Solids*, 40, 1053-1103 (1992).
38. Sutton, M. A., Deng, X., Ma, F., Newman, J. C. Jr, and James, M., 1999, Development and Application of a Crack Tip Opening Displacement-Based Mixed Mode Fracture Criterion, *Int. J. Solids & Structures*, 37 3591-3618 (2000).
39. McClintock, F. A., Plasticity aspects of fracture, in *Fracture*, vol.3, (ed. H. Liebowitz), Academic Press, New York, 47-225 (1971).
40. Zuo, ZS, Deng X and Sutton, MA, Basic studies of ductile failure processes and implications for fracture prediction, *Proc. of ASME/IUTAM Conference for IM Daniels*, June 26-31 at Virginia Tech (2002)
41. Hancock, J.W. and Mackenzie, A.C. On the mechanisms of ductile failure in high-strength steels subjected to multi-axial stress-states, *J. Mech. Phys. Solids*, Vol. 24, pp.147-169 (1976).
42. Walsh, J.A., Jata, K.V. and Starke, E.A. Jr., The influence of Mn dispersoid content and stress state on ductile fracture of 2134 type Al alloys. *Acta. Metall.*, Vol. 37, pp.2861-2871 (1989).
43. Gao, X., Shih, C.F., Tvergaard, V. and Needleman, A. Constraint effects on the ductile-brittle transition in small scale yielding. *J. Mech. Phys. Solids*, Vol. 44, pp.1255-1282 (1996).

44. Bishop, J.F.W. and Hill, R. A theory of the plastic distortion of a polycrystalline aggregate under combined stresses, *Phil. Mag.*, Vol. 42, pp414-427, 1951.
45. Kuna, M. and Sun, D.Z. Three-dimensional cell model analyses of void growth in ductile materials, *Int. J. Fracture*, Vol. 81, pp.235-258, 1996.
46. Randolph, L.W., Piascik, R.S. Three-Dimensional crack growth assessment by micro-topographic examination. *Fracture Mechanics ASTM STP 1256*; 303-318 (1995).
47. Manoharan, M., Development of a mixed-mode fracture mechanism map and its extension to mixed-mode impact Fracture. Recent advances in fracture, proceedings of a symposium held at the Annual Meeting of the Minerals, Metals & Materials Society, 373-384 (1997).
48. Deng, X., Newman Jr., J.C. A study of some issues in stable tearing crack growth simulations. *Engineering Fracture Mechanics*, 64: 291-304 (1999).
49. Sutton MA, Helm, JD and Boone, ML, "Experimental study of crack growth in thin sheet 2024-T3 aluminum under tension-torsion loading", *Intl J. Fracture* 109 285-301 (2001).
50. Hinton E and Campbell JS, "Local and Global Smoothing of Discontinuous Finite Element Functions Using a Least Squares Method, *International Journal for Numerical Methods in Engineering*, 8 461-480 (1974).
51. Cavalcante JB et al, An algorithm for Three-dimensional mesh generation for arbitrary regions with cracks, *Engineering with Computers*, Vol. 17, pp.75-91 (2001).
52. Lewis RH, Zheng Y and Gethin DT, "Three-dimensional unstructured mesh generation: Part3. Volume meshes", *Computer Methods in Applied Mechanics*, 134, 285-310 (1996).
53. Helm, J.D., Sutton, M.A., Dawicke, D.S. and Boone, M.L., "3D Computer Vision Applications for Aircraft Fuselage Materials and Structures", 1st Joint DoD/FAA/NASA Conference on Aging Aircraft in Ogden,Utah, 1327-1341 (1997).
54. Sutton, M.A., Helm, J.D. and Boone, M.L., "COD Measurements in 2024-T3 Aluminum for Residual Strength Modeling", 1st Joint DoD/FAA/NASA Conference on Aging Aircraft in Ogden,Utah, 1803-1817 (1997)

55. Helm, J.D., " Use of Three-Dimensional Digital Image Correlation for the Experimental Characterization of Buckling in Large, Thin, 2024-T3 Aluminum, Middle-Cracked Tension Specimens", Ph.D. Thesis, Department of Mechanical Engineering, University of South Carolina (1999)
56. Helm, J.D., McNeill, S.R. and Sutton, M.A., "Improved Three-Dimensional Image Correlation for Surface Displacement Measurement", *Optical Engineering*, 36 (7), 1911-1920 (1996).
57. Zhao, W, Sutton, MA, Schreier, H and Chao, YJ, "Development and Assessment of a Single Image Fringe Projection Method for Dynamic Applications", *Experimental Mechanics*, 41 (3), 205-218 (2001).
58. Maccagno, T.M. and Knott, J. F., "The Mixed Mode I/II Fracture Behavior of Lightly Tempered HY130 Steel at Room Temperature," *Engng. Fract. Mechanics*, 41, 805-820(1992).
59. Richie, R. O. and Thompson, A. W., "On Macroscopic and microscopic Analysis for Crack Initiation and Crack Growth in Ductile Alloys," *Metallurgical Transactions*, 16A, 233-248(1985).
60. Goods, S. H. and Brown, L.M., "The Nucleation of Cavities by Plastic Deformation," *Acta Metallurgica*, 27,1-15(1979).
61. Cox, T. B. and Low, J.R., "An Investigation of the Plastic Fracture of AISI 4340 and Nickel-200 Grade Maraging Steel," *Metallurgical Transactions* 5A, 1457-1470(1974).
62. Aoki, S., Kishimoto, K., Yoshida, T. and Sakata, M., "A Finite Element Study of the Near Crack Tip Deformation of a Ductile Material under Mixed Mode Loading," *J. Mech. Phys. Solids*, 35, 431-455 (1987).
63. Ghosal, A.K. and Narasimhan, R., "Numerical Simulations of Hole and Growth and Ductile Fracture Initiation under Mixed Mode Loading," *Intl J. Fracture*, 77, 281-304 (1996).
64. J.G. Bakuckas, Jr., C.A. Bigelow and P.W. Tan, "Full-scale Aircraft Structural Test and Evaluation Research (FASTER) Facility", Joint NASA/FAA/AFRL Conference on Aging Aircraft Albuquerque, NM (September, 1999).

VII. Appendix - List of Project-based Publications

Fully Refereed Papers

1. E. Mahgoub, X. Deng, and M. A. Sutton, "Three-dimensional Stress and Deformation Fields Around Flat and Slant Cracks Under Remote Mode I Loading Conditions," *Engineering Fracture Mechanics* (submitted).
2. M. A. Sutton, F. Ma, and X. Deng, "Mixed mode I/II crack-tip stress fields characterized by a triaxial stress parameter and a plastic deformation extent based characteristic length," *Fatigue and Fracture Mechanics: 33rd Volume, ASTM STP 1417*, W. G. Reuter and R. S. Piascik, Eds., American Society for Testing and Materials, West Conshohocken, PA, 2002.
3. F. Ma, M. A. Sutton, and X. Deng, "Plane strain mixed mode crack-tip stress fields characterized by a triaxial stress parameter and a plastic deformation extent based characteristic length," *Journal of Mechanics and Physics of Solids* 49 (2001) 2921-2953.
4. M. A. Sutton, X. Deng, F. Ma, J. C. Newman, Jr., and M. James, "Development and application of a crack tip opening displacement-based mixed mode fracture criterion," *International Journal of Solids and Structures* 37 (2000) 3591-3618.
5. J.D. Helm, M.A. Sutton and M.L. Boone, "Experimental Study of Crack Growth in Thin Sheet Material under Tension-Torsion Loading", International Journal of Fracture, 109, 285-301 (2001).
6. Helm, J.D. Helm, M.A. Sutton and M.L. Boone, "Characterizing Crack Growth in Thin Aluminum Panels Under Tension-Torsion Loading with Three-Dimensional Digital Image Correlation", *Nontraditional Methods of Sensing Stress, Strain and Damage in Materials and Structure*, G. F. Lucas, P. C. McKeighan and J. S. Ransom, Eds, ASTM STP 1323 3-14 (2001).

Partially Refereed Papers

1. J. Zuo, M. A. Sutton, and X. Deng, "A model for failure initiation in ductile materials," Proceedings of the 14th U.S. National Congress of Theoretical and Applied Mechanics, Virginia Tech, Blacksburg, VA, June 23-28, 2002.

2. E. Mahgoub, X. Deng, and M. A. Sutton, "Stress and deformation fields around a slant crack," CD-ROM Proceedings of the 21st Southeastern Conference on Theoretical and Applied Mechanics (SECTAM XXI), Orlando, Florida, May 19-21, 2002.
3. J. Zuo, M. A. Sutton, and X. Deng, "A unit-cell based micro-mechanics study of ductile failure by void growth," Proceedings of the 2002 Society for Experimental Mechanics Annual Conference & Exposition on Experimental and Applied Mechanics, Milwaukee, Wisconsin, June 10-12, 2002.
4. X. Deng, E. Mahgoub, and M. A. Sutton, "A three-dimensional analysis of slant fracture in ductile materials," Proceedings of the 2002 Society for Experimental Mechanics Annual Conference & Exposition on Experimental and Applied Mechanics, Milwaukee, Wisconsin, June 10-12, 2002.
5. X. Deng, M. A. Sutton, J. Zuo, and L. Wang, "Mixed-mode fracture analysis of airframe materials," Proceedings of the 5th Joint NASA/FAA/DoD Conference on Aging Aircraft, Kissimmee, FL, Sept. 10-13, 2001.
6. X. Deng, M. A. Sutton, and F. Ma, "Recent advances in mixed mode fracture characterization of airframe materials," Proceedings of the 2001 Society for Experimental Mechanics Annual Conference & Exposition on Experimental and Applied Mechanics, Portland, Oregon, June 4-6, 2001.
7. M. A. Sutton, F. Ma, X. Deng and S. Fawaz, "The basis of crack opening displacement fracture criteria for predicting mixed mode I/II crack initiation and growth in thin sheet materials," Proceedings of the 4th Joint DoD/FAA/NASA Conference on Aging Aircraft (CAA00), St. Louis, Missouri, May 15-18, 2000.

Conference/Seminar Presentations

1. M. A. Sutton, X. Deng, J. Zuo, and E. Mahgoub, "Recent progress in 3D modeling of stable tearing crack growth," to be presented at the 6th Joint FAA/DoD/NASA Aging Aircraft Conference, San Francisco, CA, Sept. 16-19, 2002. X. Deng, E. Mahgoub, and M. A. Sutton, "Analysis of slant fracture in specimens under nominal Mode I loading conditions," presentation at the 14th U.S. National Congress of Theoretical and Applied Mechanics, Virginia Tech,

- Blacksburg, VA, June 23-28, 2002. J. Zuo, M. A. Sutton, and X. Deng, "A model for failure initiation in ductile materials," presentation at the 14th U.S. National Congress of Theoretical and Applied Mechanics, Virginia Tech, Blacksburg, VA, June 23-28, 2002. J. Zuo, M. A. Sutton, and X. Deng, "A unit-cell based micro-mechanics study of ductile failure by void growth," presentation at the 2002 Society for Experimental Mechanics Annual Conference & Exposition on Experimental and Applied Mechanics, Milwaukee, Wisconsin, June 10-12, 2002. X. Deng, E. Mahgoub, and M. A. Sutton, "A three-dimensional analysis of slant fracture in ductile materials," presentation at the 2002 Society for Experimental Mechanics Annual Conference & Exposition on Experimental and Applied Mechanics, Milwaukee, Wisconsin, June 10-12, 2002. E. Mahgoub, X. Deng, and M. A. Sutton, "Stress and deformation fields around a slant crack," presentation at the 21st Southeastern Conference on Theoretical and Applied Mechanics (SECTAM XXI), Orlando, Florida, May 19-21, 2002. X. Deng, "Mixed-mode characterization and crack growth simulation" seminar presentation at Zhejiang University, P. R. China, December 18, 2001. X. Deng, "Mixed-mode characterization and crack growth simulation" seminar presentation at Shanghai Jiaotong University, P. R. China, December 14, 2001.
9. X. Deng, M. A. Sutton, L. Wang, and J. Zuo, "Mixed-mode fracture analysis of airframe materials," presented at the 5th Joint NASA/FAA/DoD Conference on Aging Aircraft, Kissimmee, FL, Sept. 10-13, 2001. X. Deng, "Mixed-Mode Fracture, Crack-Tip Fields, and Stable Crack Growth Simulation" seminar presentation at General Motors R & D Center, Dearborn, Michigan, August 1, 2001
 11. X. Deng, L. Wang, and M. A. Sutton, "Mixed-mode crack growth simulation," presented at the 6th U. S. National Congress on Computational Mechanics, Dearborn, Michigan, August 1-3, 2001.
 12. M. A. Sutton, F. Ma, X. Deng, and J. C. Newman, Jr., "Mixed mode I/II crack-tip stress fields characterized by a triaxial stress parameter and a plastic deformation extent based characteristic length," presented at the 33rd

Symposium on Fatigue and Fracture Mechanics, Jackson Lake Lodge, Jackson Hole, WY, Jun 26-29, 2001.

13. X. Deng, M. A. Sutton, and F. Ma, "Recent advances in mixed mode fracture characterization of airframe materials," presented at the 2001 Society for Experimental Mechanics Annual Conference & Exposition on Experimental and Applied Mechanics, Portland, Oregon, June 4-6, 2001.
14. M. A. Sutton, F. Ma, and X. Deng, "Mixed Mode I/II Crack-Tip Stress Fields," presented at the 37th Society of Engineering Science Annual Technical Meeting (SES 2000), University of South Carolina, Columbia, SC, Oct. 23-25, 2000.
15. F. Ma, M. A. Sutton, and X. Deng, "Mixed mode I/II crack-tip stress fields," presented at the 20th International Congress of Theoretical and Applied Mechanics (ICTAM 2000), Chicago, August 27-September 2, 2000.

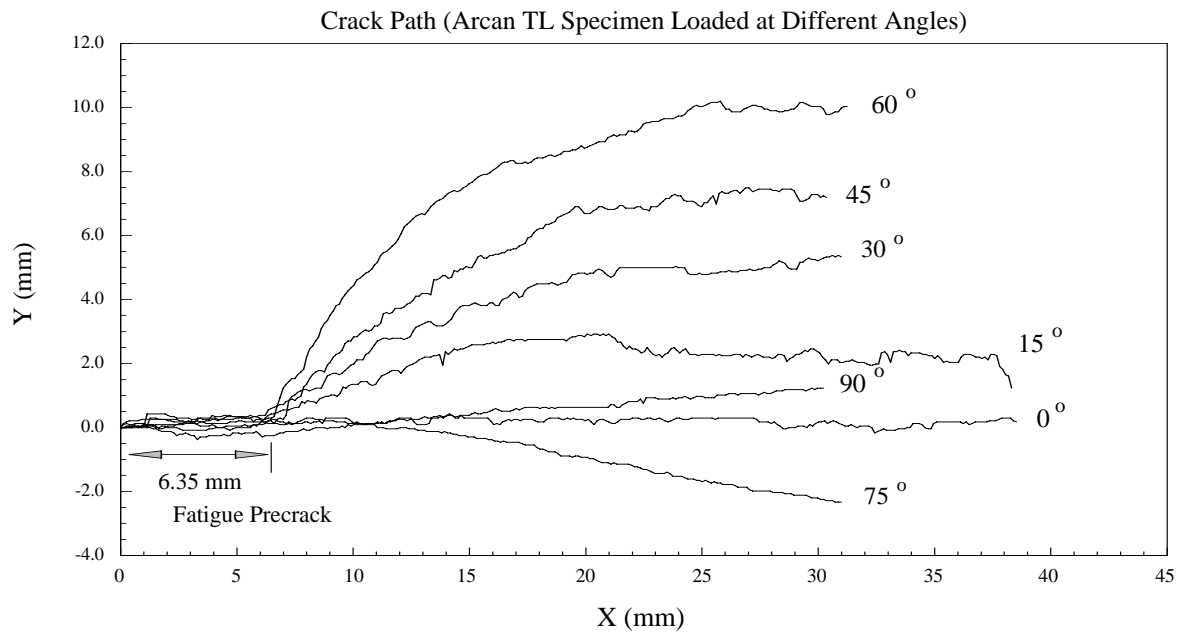


Figure 1: Crack-growth paths in Arcan specimens for various loading angles

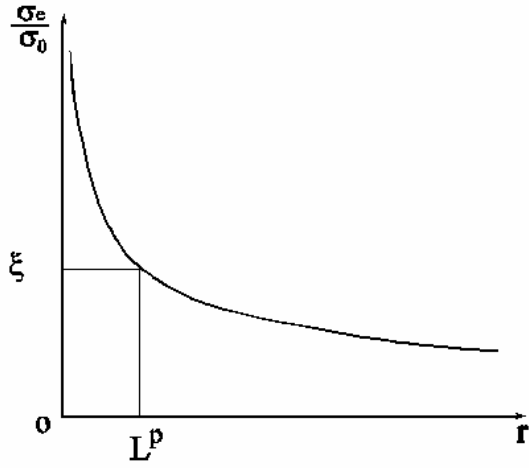


Figure 2a

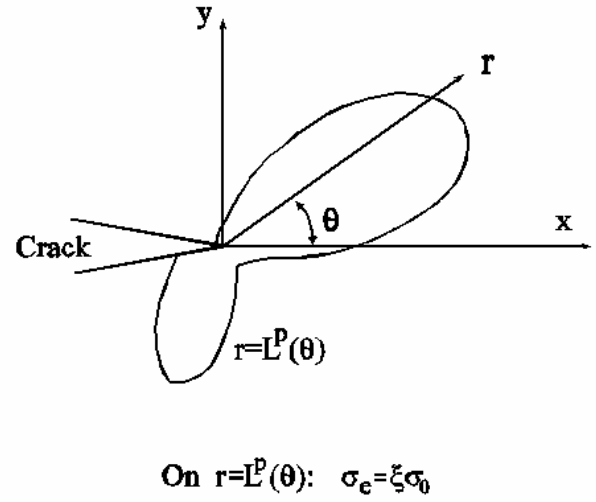


Figure 2b

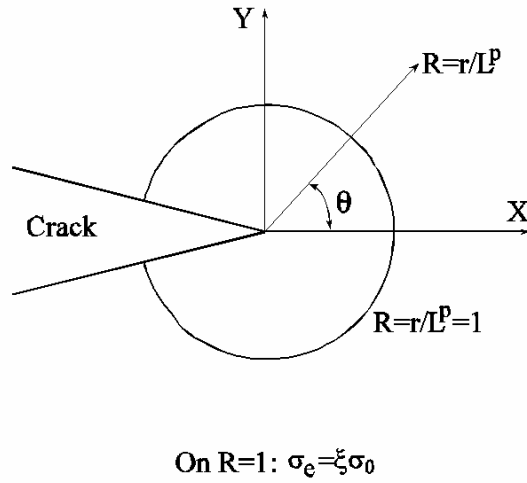


Figure 2c

Figure 2: (a) Schematic representation for L^p definition; (b) Mixed mode I/II crack tip plastic zone shape defined by $\sigma_e = \xi \sigma_0$; (c) A normalized mixed mode I/II crack tip plastic zone shape in Figure 2b

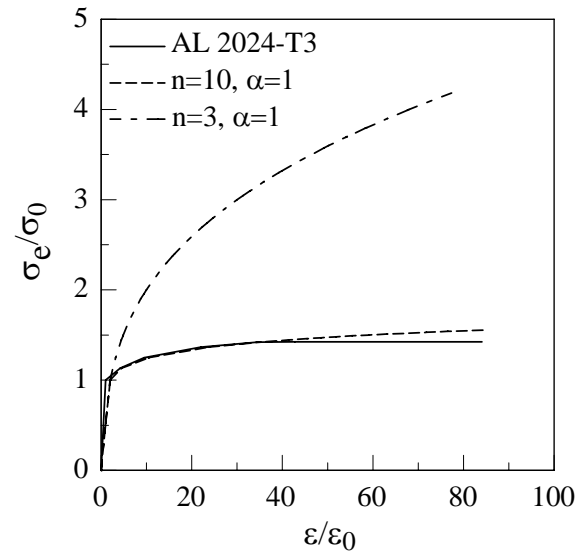


Figure 3: The hardening rules for AL-2024T3 and power-laws, $n=10$ and $n=3$

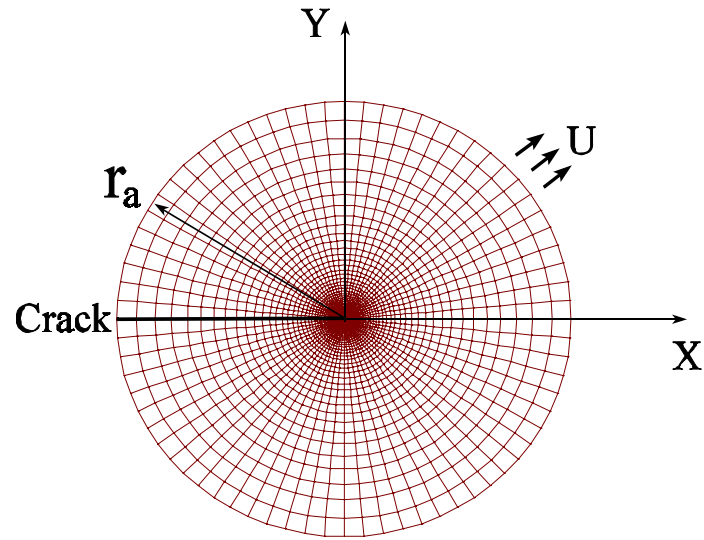


Figure 4: Finite element mesh for small scale yielding (SSY) model

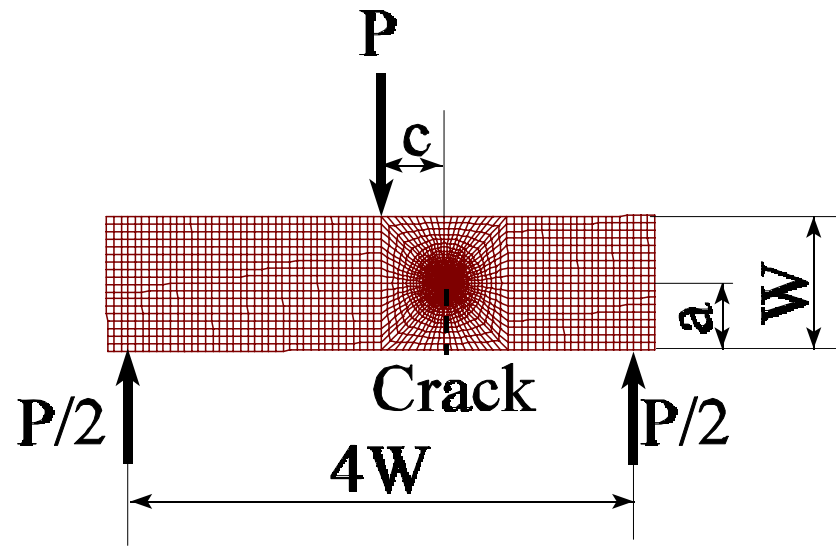


Figure 5a

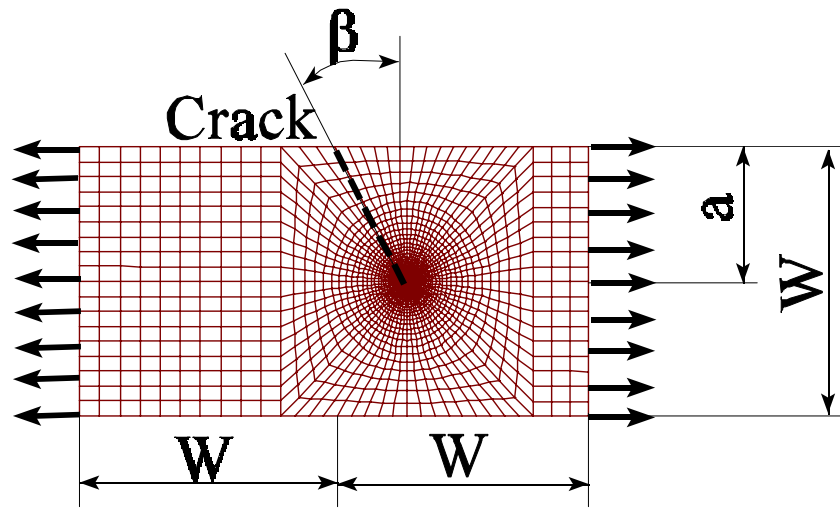


Figure 5b

Figure 5: Typical geometry and finite element meshes, (a) TPB, $c/w=0.5$, and (b) TB, $\beta=30^\circ$

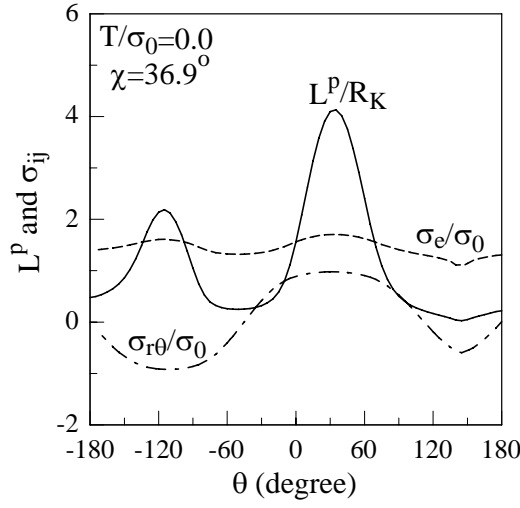


Figure 6(a)

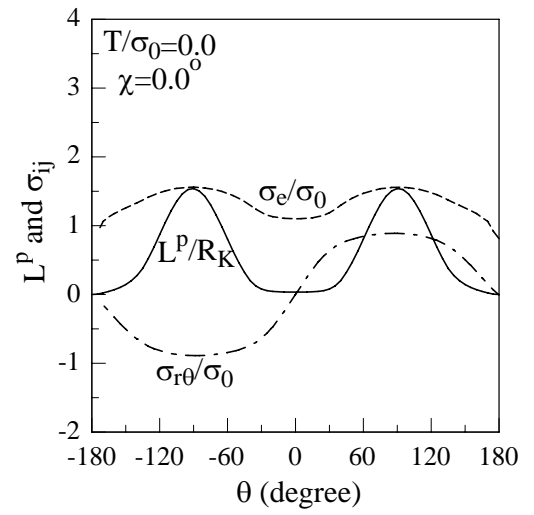


Figure 6(b)

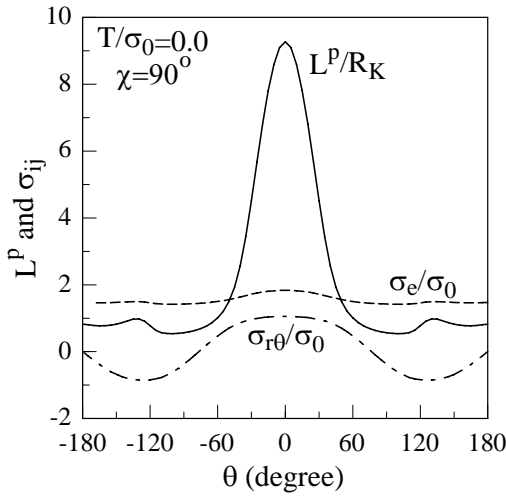


Figure 6(c)

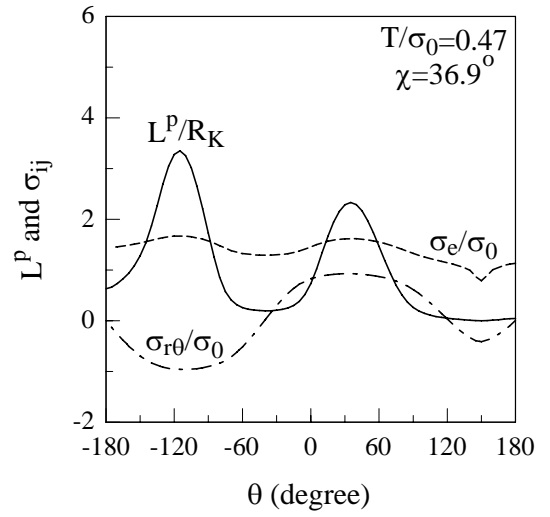


Figure 6(d)

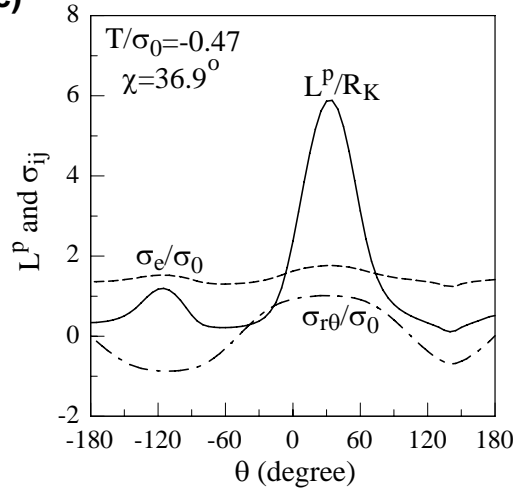


Figure 6(e)

Figure 6: Angular variations of L^P/R_K , von-Mises stress σ_e/σ_0 and shear stress $\sigma_{r\theta}/\sigma_0$ at $r/R_K=0.0865$, SSY model, (a) $T/\sigma_0=0$, $\chi=0^\circ$, (b) $T/\sigma_0=0$, $\chi=36.9^\circ$, (c) $T/\sigma_0=0$, $\chi=90^\circ$, (d) $T/\sigma_0=0.47$, $\chi=36.9^\circ$, and (e) $T/\sigma_0=-0.47$, $\chi=36.9^\circ$

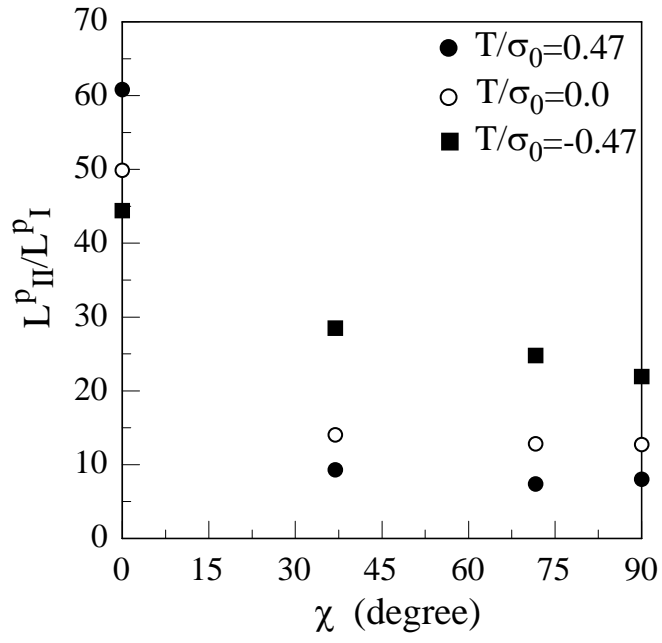


Figure 7: L_{II}^p / L_I^p for SSY model, $n=10$

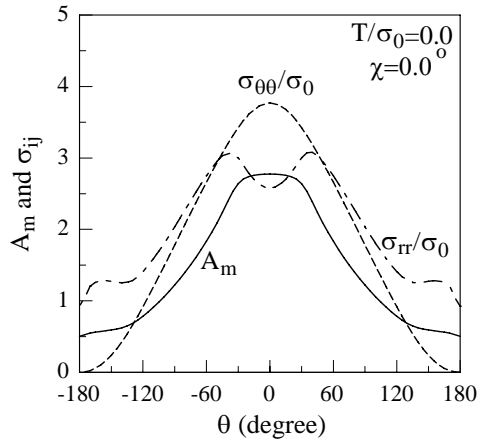


Figure 8(a)

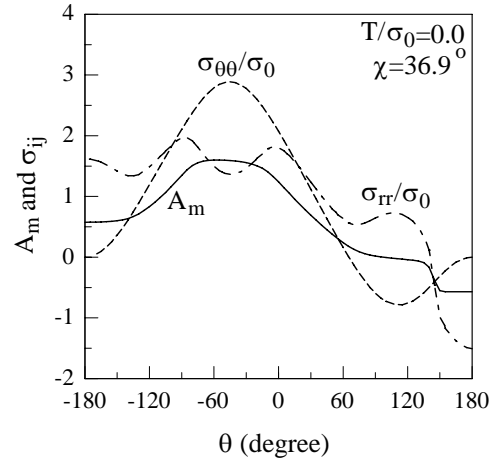


Figure 8(b)

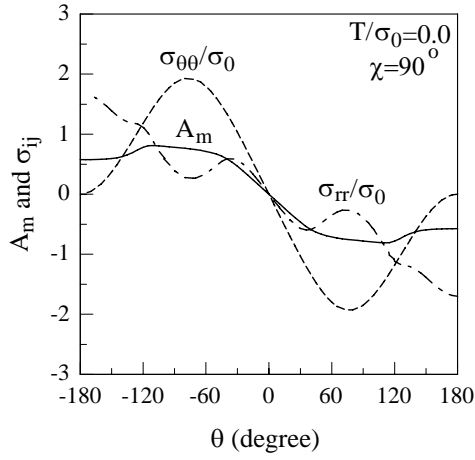


Figure 8(c)

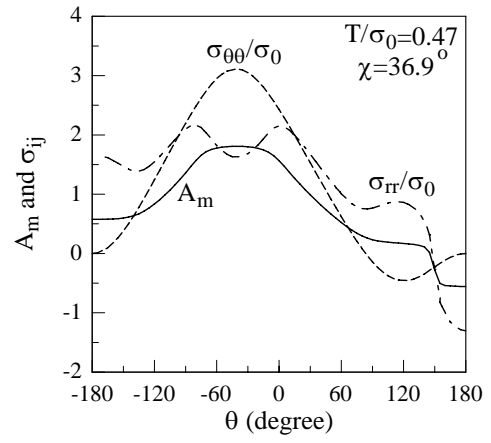


Figure 8(d)

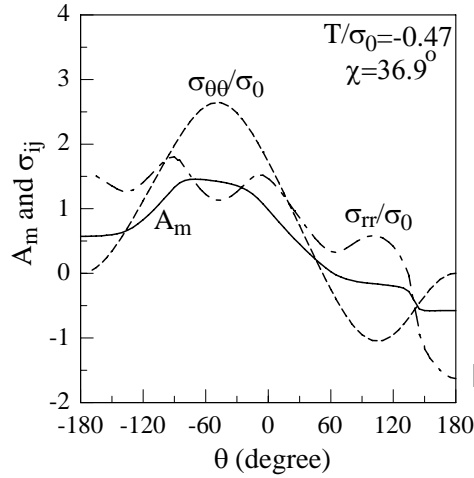


Figure 8(e)

Figure 8: Angular variations of A_m , normal stresses σ_{rr}/σ_0 and $\sigma_{\theta\theta}/\sigma_0$ at $r/R_K=0.0865$, SSY model, (a) $T/\sigma_0=0$, $\chi=0^\circ$, (b) $T/\sigma_0=0$, $\chi=36.9^\circ$, (c) $T/\sigma_0=0$, $\chi=90^\circ$, (d) $T/\sigma_0=0.47$, $\chi=36.9^\circ$, and (e) $T/\sigma_0=-0.47$, $\chi=36.9^\circ$

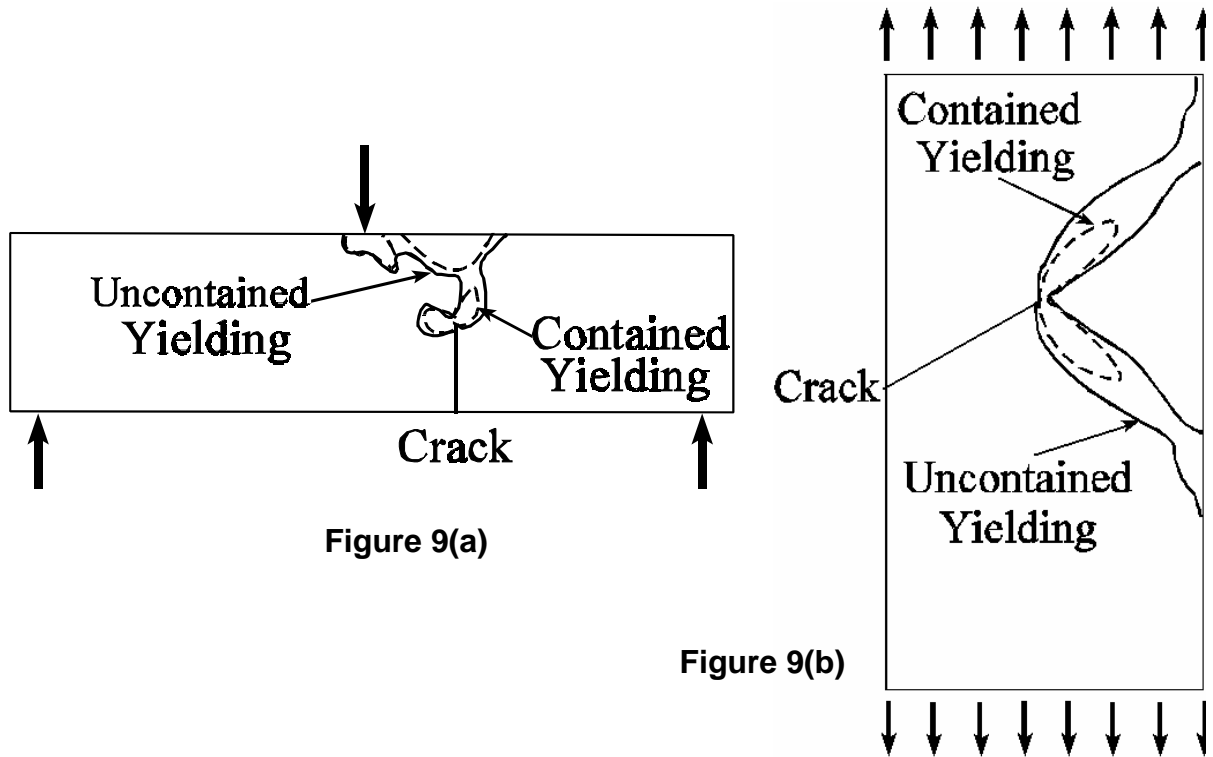


Figure 9: Contained and uncontained yielding shapes of (a) TPB specimens, $c/w=0.5$ and (b) TB specimen, $\beta=30$

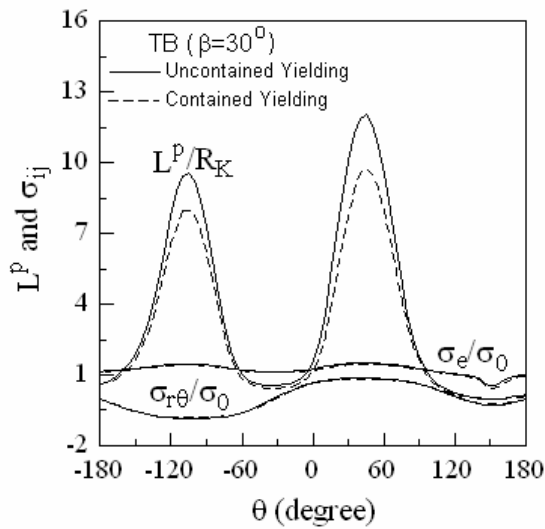


Figure 10(a)

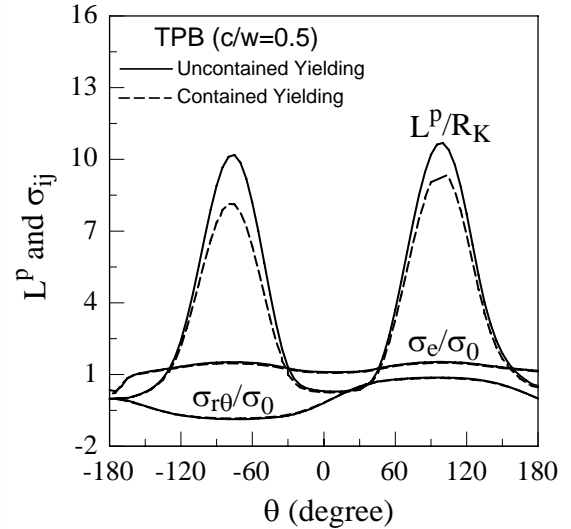


Figure 10(b)

Figure 10: Angular variations of L^p/R_K , effective stress σ_e/σ_0 and shear stress $\sigma_{r\theta}/\sigma_0$ for (a) TB specimen, $\beta=30^\circ$, and (b) TPB specimens, $c/w=0.5$

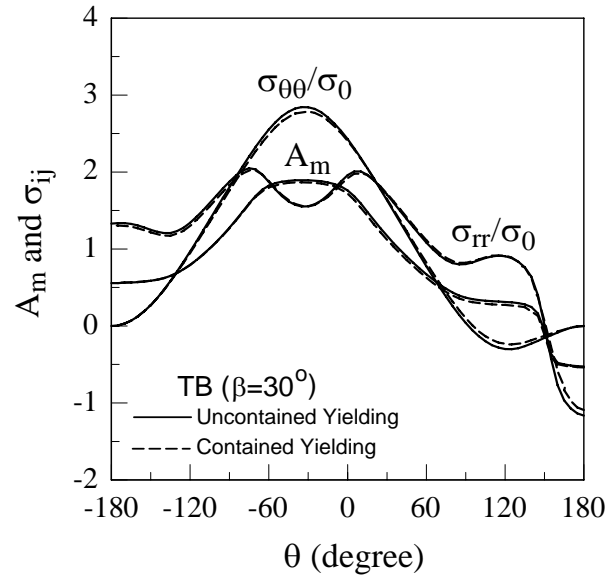


Figure 11(a)

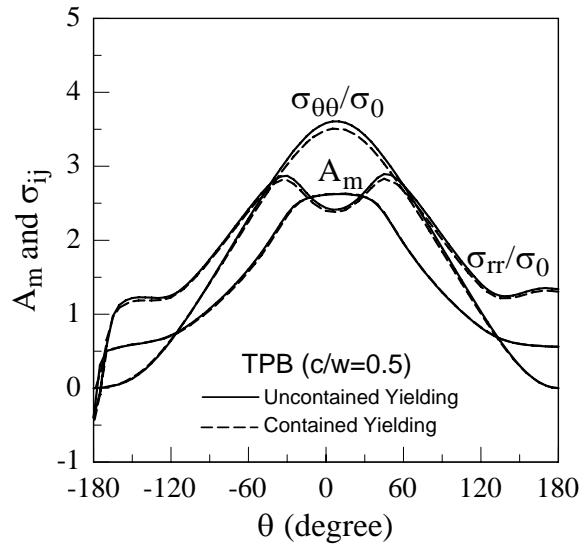


Figure 11(b)

Figure 11: Angular variations of A_m and normal stresses (σ_{rr}/σ_0 and $\sigma_{\theta\theta}/\sigma_0$) for (a) TB specimen, $\beta = 30^\circ$, and (b) TPB specimens, $c/w = 0.5$

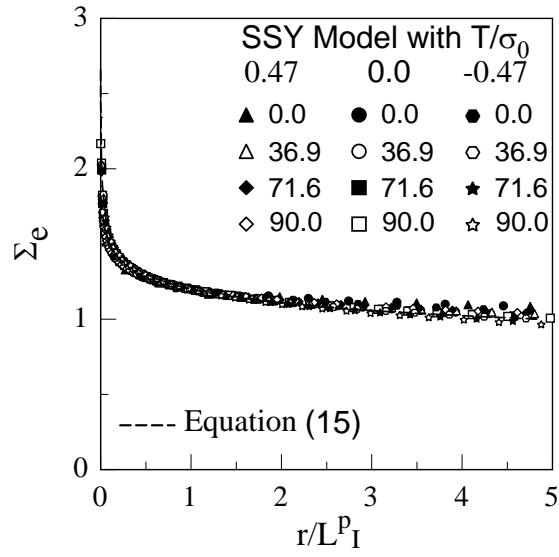


Figure 12a

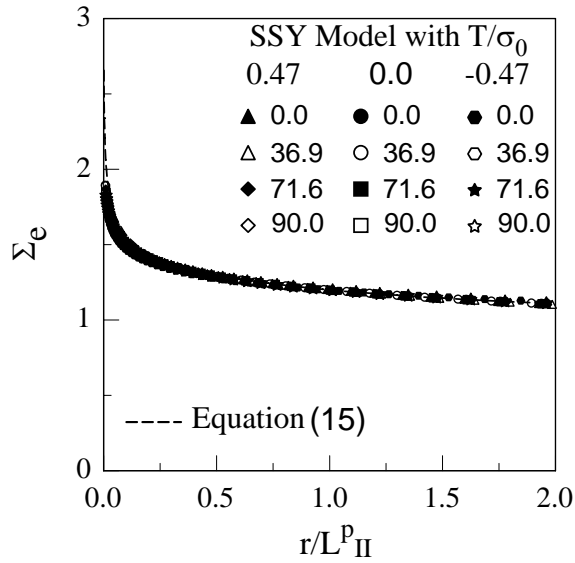


Figure 12b

Figure 12: The variation of $\Sigma_e = \sigma_e/\sigma_0$ with normalized distance, r/L^P , in (a) mode I and (b) mode II directions, respectively, for SSY model, power law material ($n=10$).

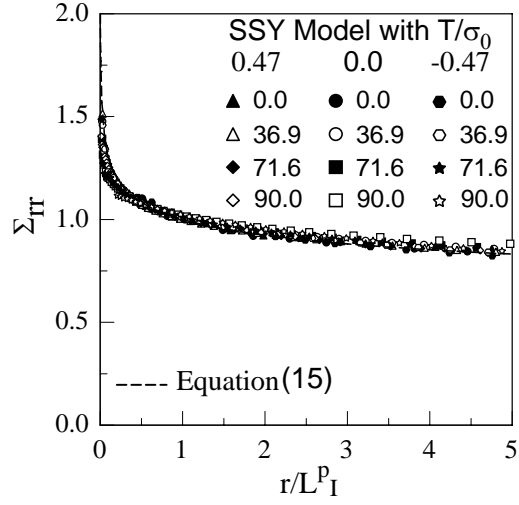


Figure 13a

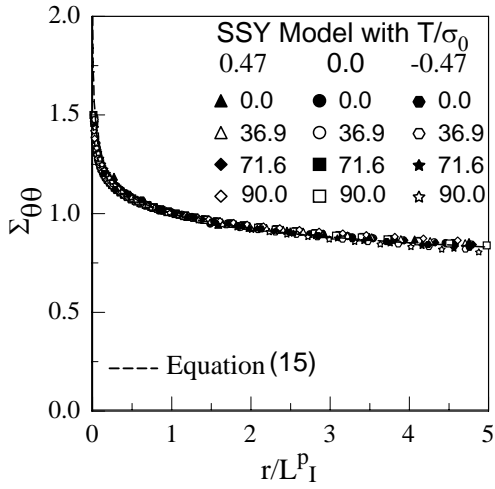


Figure 13b

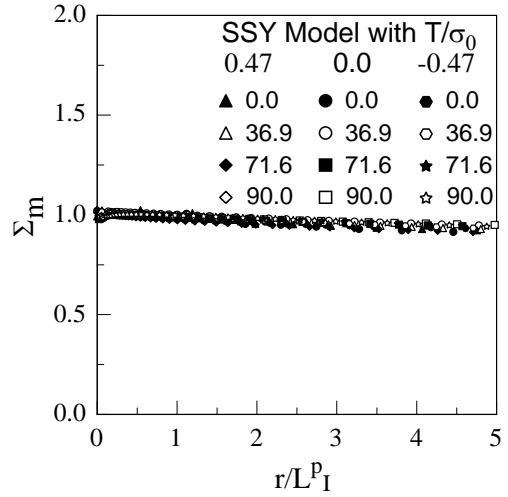


Figure 13c

Figure 13: The variation of (a) $\Sigma_{rr}=\sigma_{rr}/A_{rr}\sigma_0$, (b) $\Sigma_{\theta\theta}=\sigma_{\theta\theta}/A_{\theta\theta}\sigma_0$ and (c) $\Sigma_m=\sigma_m/A_m\sigma_e$ with normalized distance, r/L_I^P , in mode I direction, respectively, for SSY model and power law material ($n=10$).

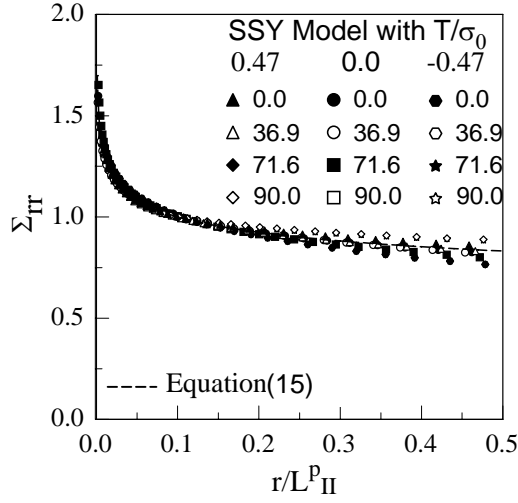


Figure 14a

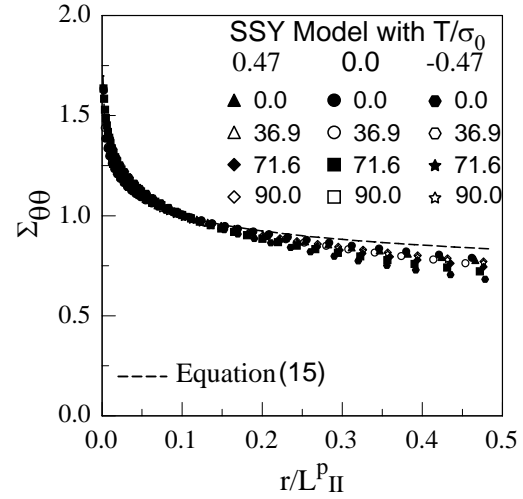


Figure 14b

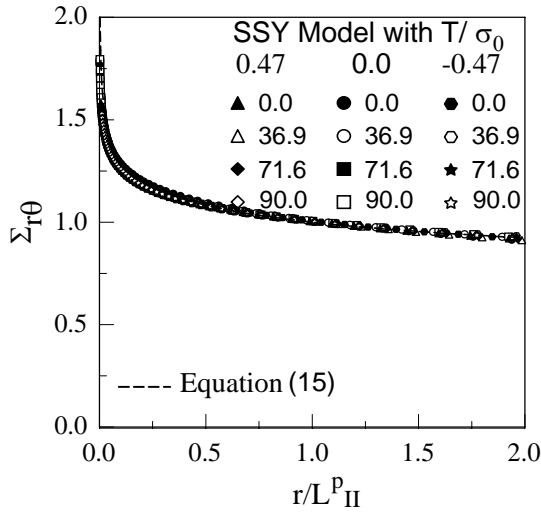


Figure 14c

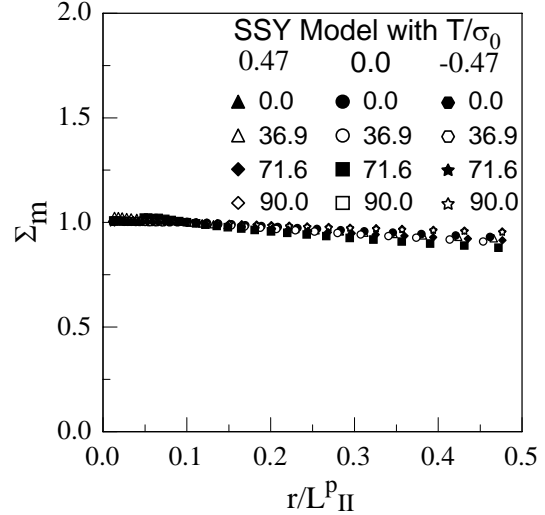


Figure 14d

Figure 14: The variation of (a) $\Sigma_{rr} = \sigma_{rr}/A_{rr}\sigma_0$, (b) $\Sigma_{\theta\theta} = \sigma_{\theta\theta}/A_{\theta\theta}\sigma_0$, (c) $\Sigma_{r\theta} = \sigma_{r\theta}/A_{r\theta}\sigma_0$ and (d) $\Sigma_m = \sigma_m/A_m\sigma_e$ with normalized distance, r/L^p , in mode II direction, respectively, for SSY model, power law material ($n=10$).

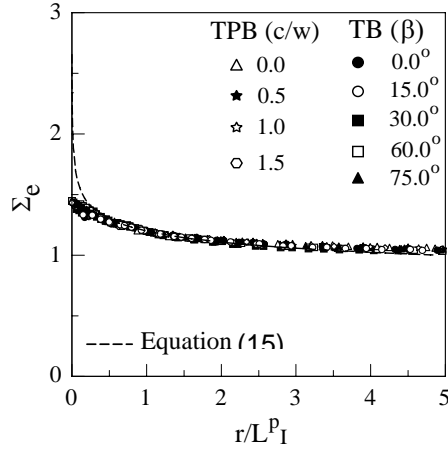


Figure 15 (a)

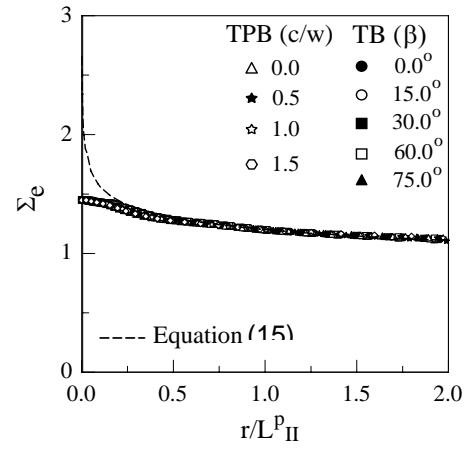


Figure 15 (b)

Figure 15: The variation of $\Sigma_e = \sigma_e/\sigma_0$ with normalized distance, r/L^P , in (a) mode I and (b) mode II directions, respectively, for Al-2024T3 TB and TPB specimens

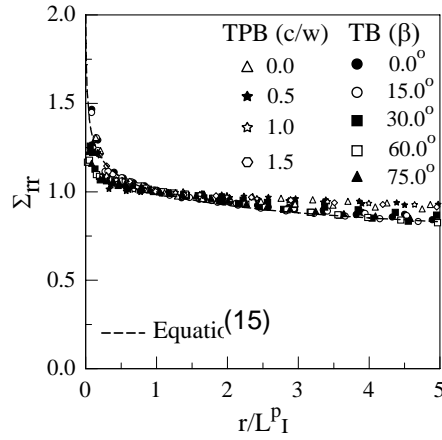


Figure 16 (a)

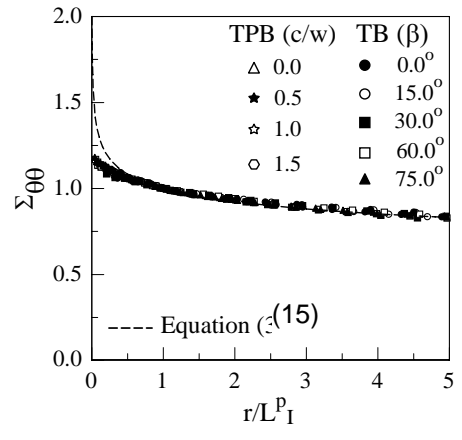


Figure 16 (b)

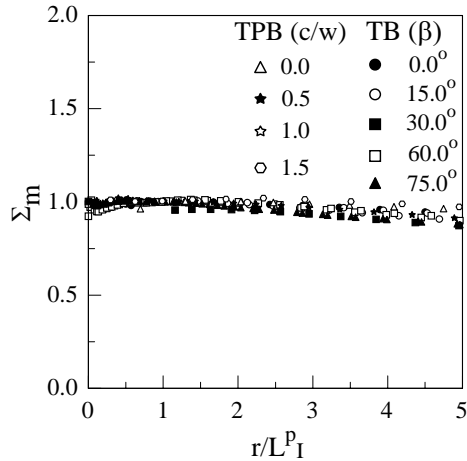


Figure 16 (c)

Figure 16: The Variation of (a) $\Sigma_{rr} = \sigma_{rr}/A_{rr}\sigma_0$, (b) $\Sigma_{\theta\theta} = \sigma_{\theta\theta}/A_{\theta\theta}\sigma_0$ and (c) $\Sigma_{mm} = \sigma_{mm}/A_{mm}\sigma_0$ with normalized distance, r/L^P , in Mode I direction, respectively, for Al-2024T3 TB and TPB specimens

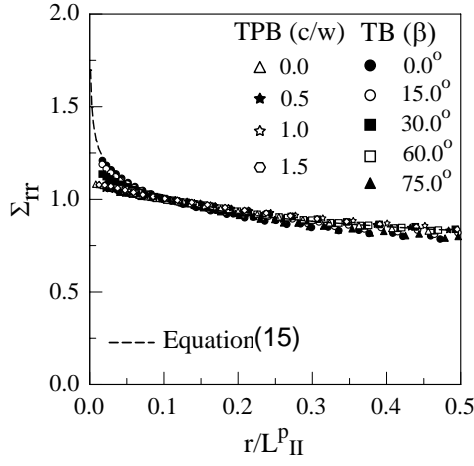


Figure 17(a)

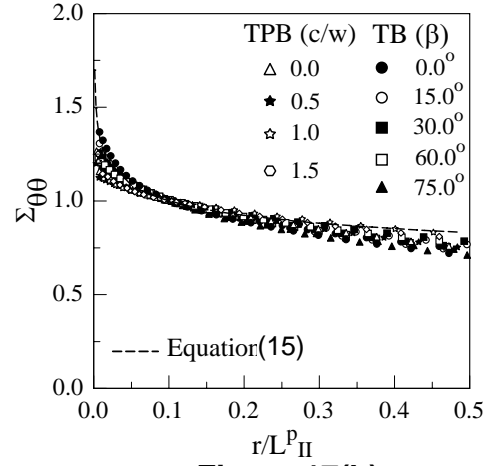


Figure 17(b)

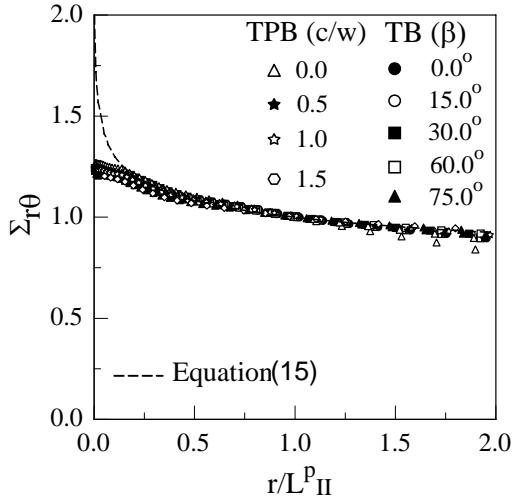


Figure 17(c)

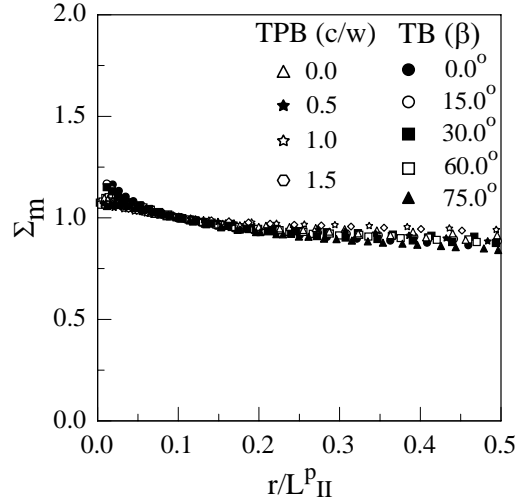


Figure 17(d)

Figure 17: The variation of (a) $\Sigma_{rr} = \sigma_{rr}/A_{rr}\sigma_0$, (b) $\Sigma_{\theta\theta} = \sigma_{\theta\theta}/A_{\theta\theta}\sigma_0$, (c) $\Sigma_{r\theta} = \sigma_{r\theta}/A_{r\theta}\sigma_0$ and (d) $\Sigma_m = \sigma_m/A_m\sigma_e$ with normalized distance, r/L^P , in mode II direction, respectively, for Al-2024T3 TB and TPB specimens

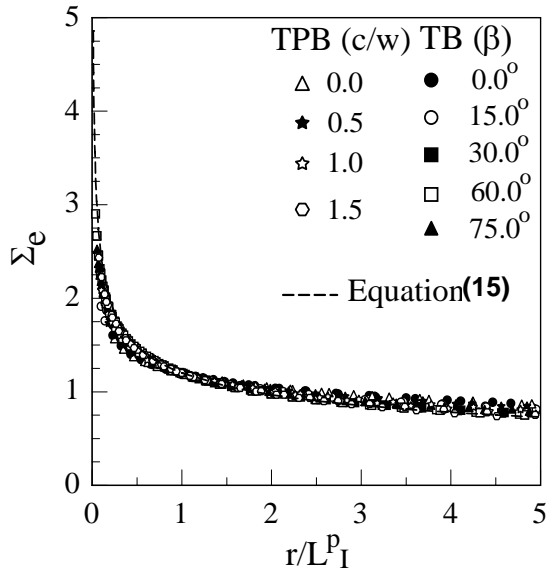


Figure 18(a)

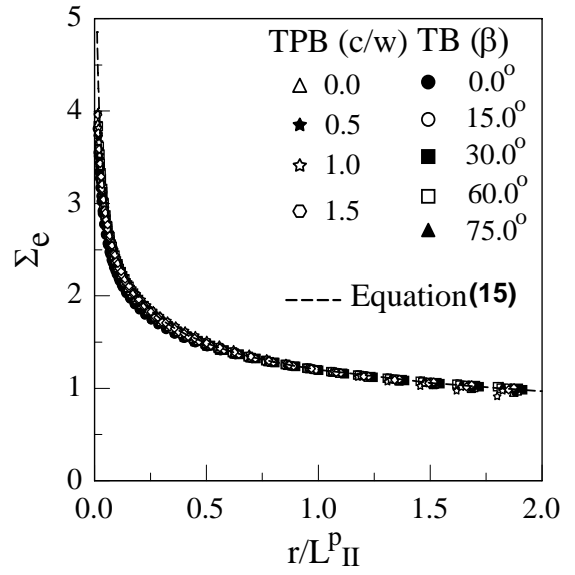


Figure 18(b)

Figure 18: The variation of $\Sigma_e = \sigma_e / \sigma_0$ with normalized distance, r/L^p , in (a) mode I and (b) mode II directions, respectively, for TB and TPB specimens, power law material ($n=3$)

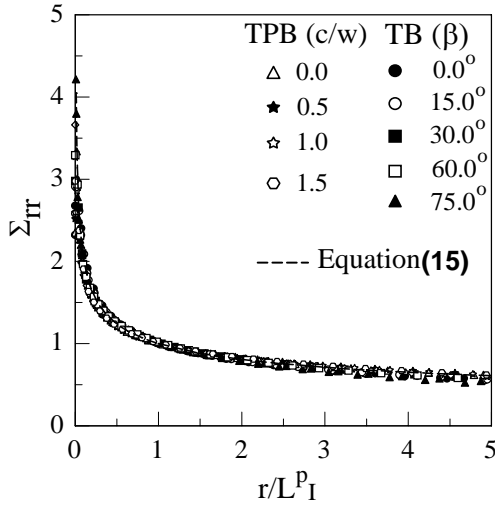


Figure 19(a)

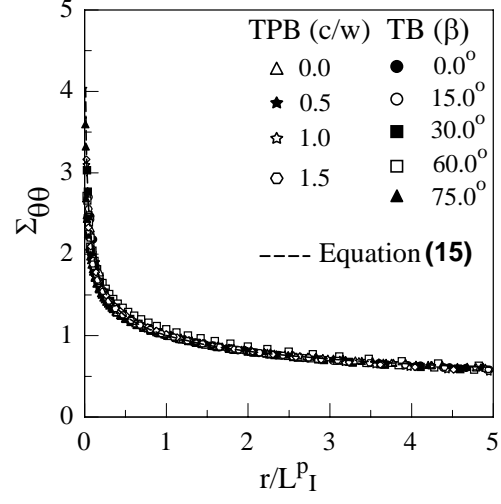


Figure 19(b)

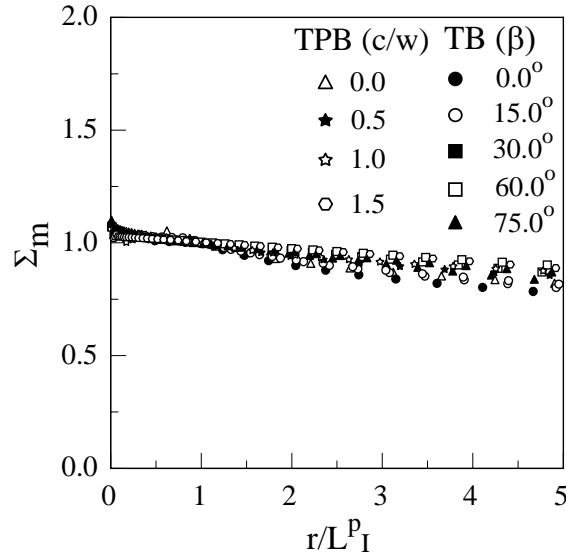


Figure 19(c)

Figure 19: The variation of (a) $\Sigma_{rr} = \sigma_{rr}/A_{rr}\sigma_0$, (b) $\Sigma_{\theta\theta} = \sigma_{\theta\theta}/A_{\theta\theta}\sigma_0$ and (c) $\Sigma_m = \sigma_m/A_m\sigma_e$ with normalized distance, r/L_I^P , in mode I direction, respectively, for TB and TPB specimens, power law material ($n=3$)

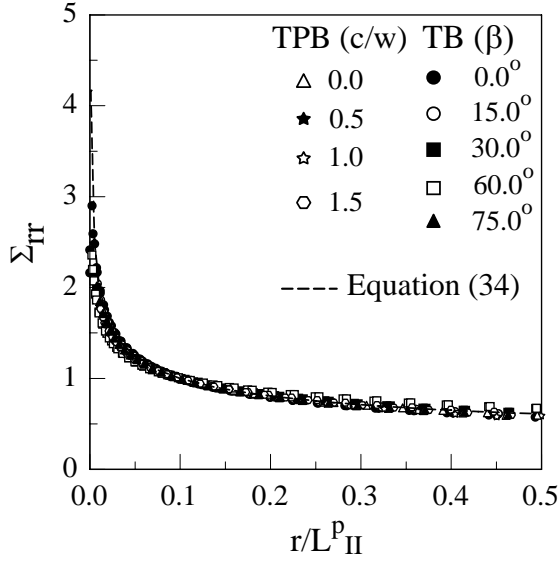


Figure 20a

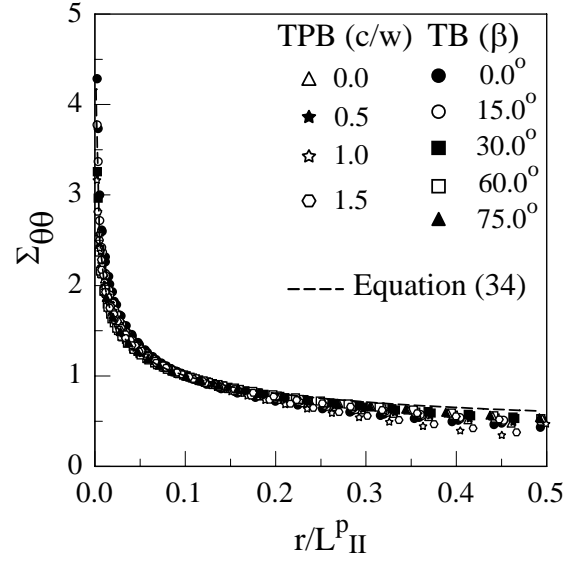


Figure 20b

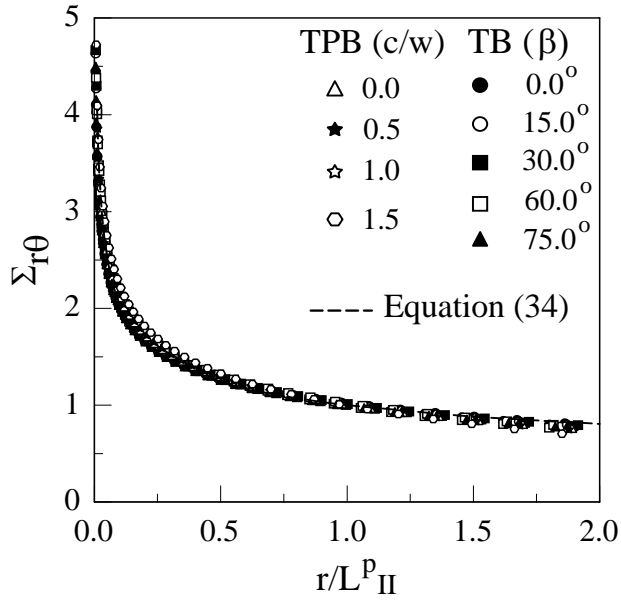


Figure 20c

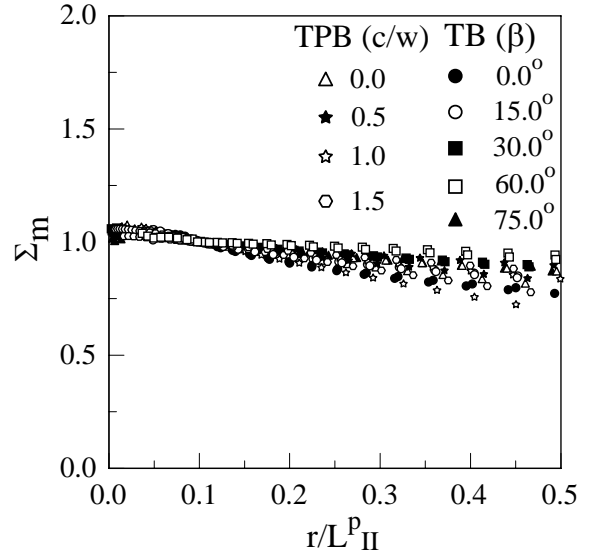


Figure 20d

Figure 20: The variation of (a) $\Sigma_{rr} = \sigma_{rr}/A_{rr}\sigma_0$, (b) $\Sigma_{\theta\theta} = \sigma_{\theta\theta}/A_{\theta\theta}\sigma_0$, (c) $\Sigma_{r\theta} = \sigma_{r\theta}/A_{r\theta}\sigma_0$, and (d) $\Sigma_m = \sigma_m/A_m\sigma_e$ with normalized distance, r/L^p , in mode II direction, respectively, for TB and TPB specimens, power law material ($n=3$)

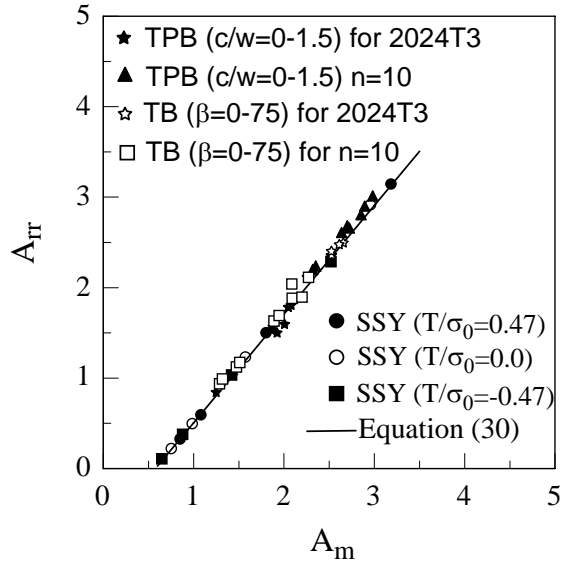


Figure 21a

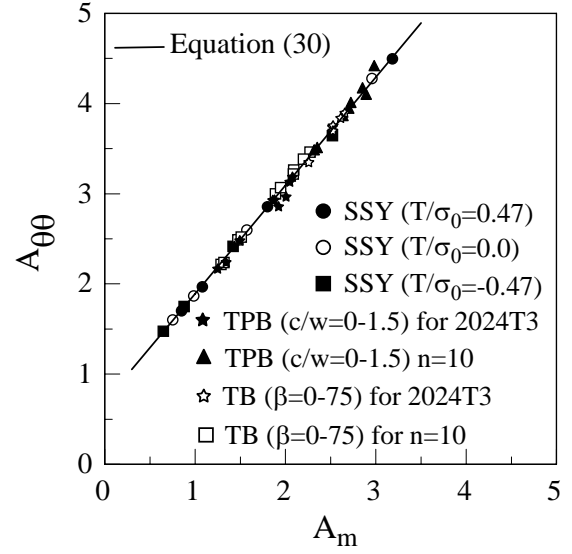


Figure 21b

Figure 21: The functions $A_{ij}(A_m)$ in mode I direction for SSY model, TP and TPB specimens, power law material ($n=10$) and Al-2024T3. (a) $A_{rr}(A_m)$ and (b) $A_{\theta\theta}(A_m)$

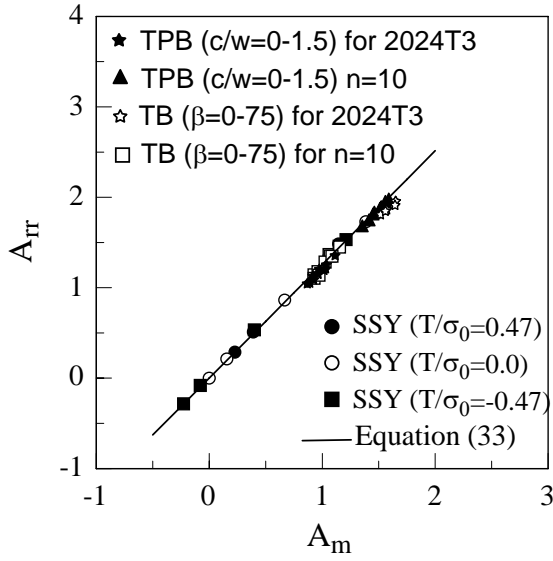


Figure 22a

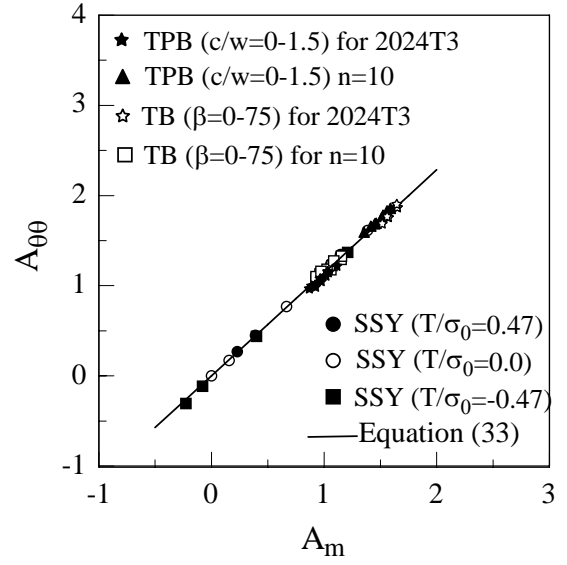


Figure 22b

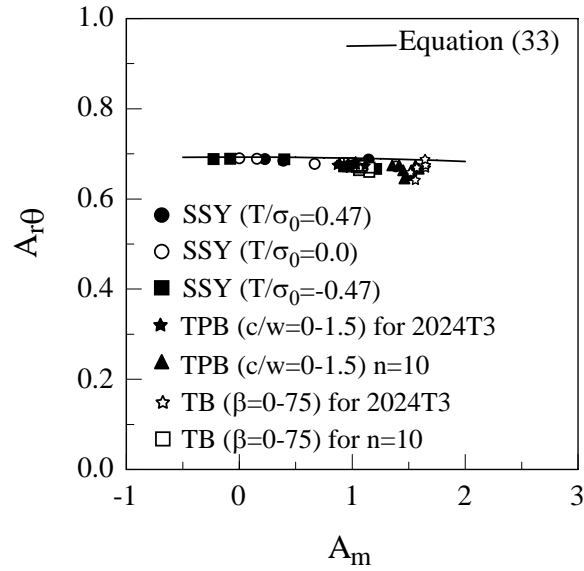


Figure 22c

Figure 22: The functions $A_{ij}(A_m)$ in mode II direction for SSY model, TP and TPB specimens, power law material ($n=10$) and Al-2024T3. (a) $A_{rr}(A_m)$, (b) $A_{\theta\theta}(A_m)$, and $A_{r\theta}(A_m)$

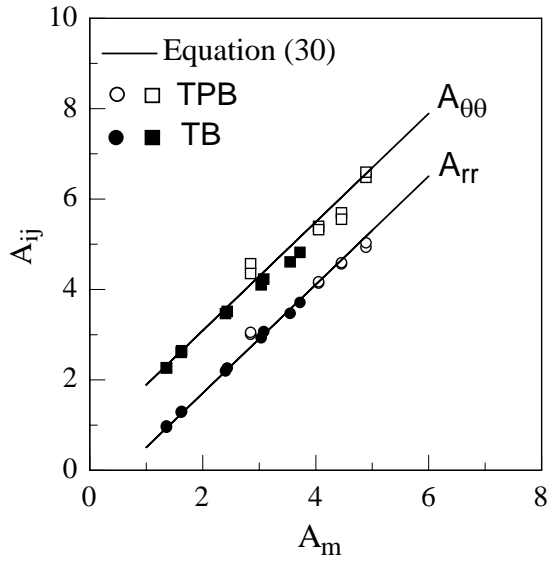


Figure 23a

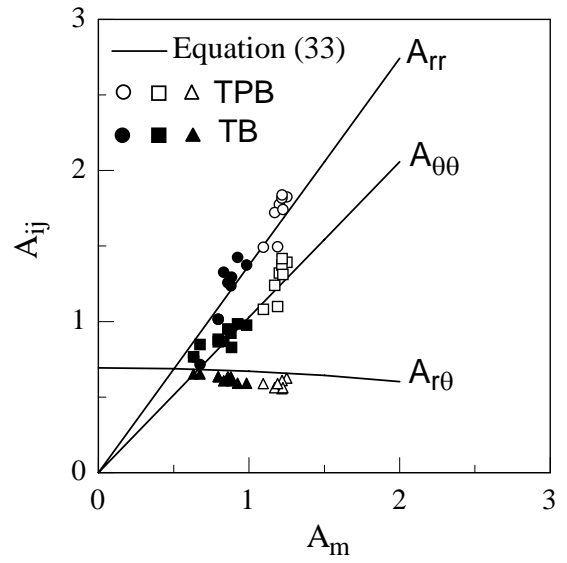


Figure 23b

Figure 23: The functions $A_{ij}(A_m)$ for TP and TPB specimens, power law material ($n=3$). (a) in mode I direction, (b) in mode II direction

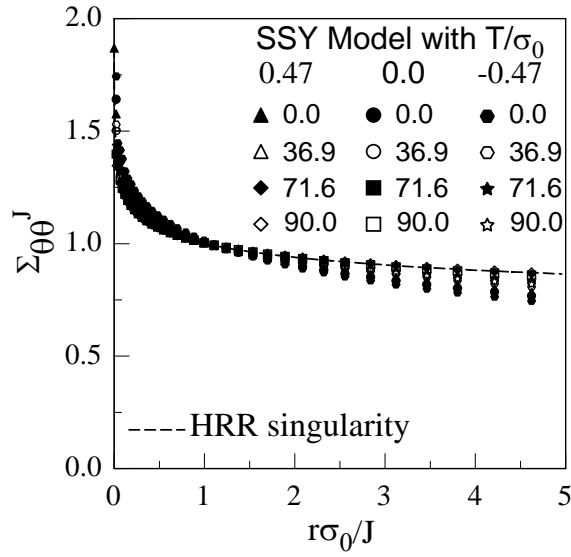
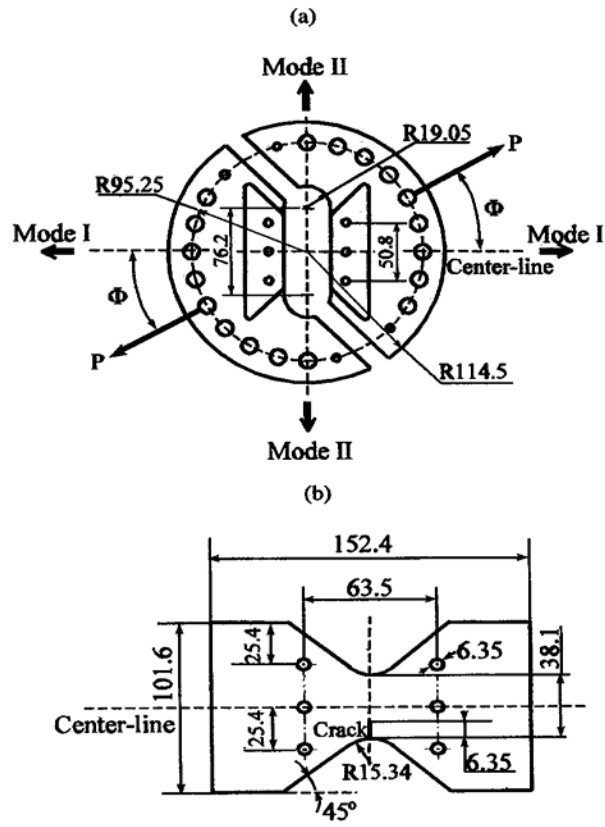


Figure 24: Variation of $\Sigma_{\theta\theta} = \sigma_{\theta\theta} / \sigma^A_{\theta\theta}$ with normalized distance $r\sigma_0/J$ in mode I direction, for SSY mode, power law material ($n=10$)



All dimensions in mm

Figure 25: Modified Arcan fixture-specimen system and finite element model

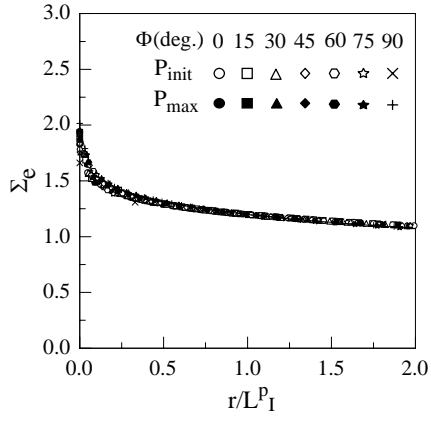


Figure 26(a)

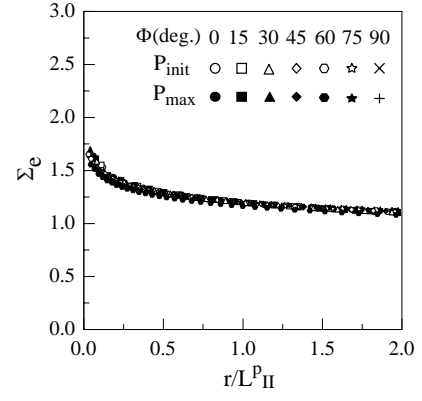


Figure 26(b)

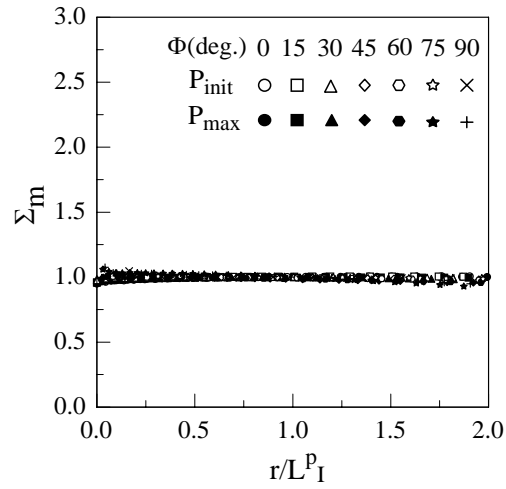


Figure 26(c)

Figure 26: The variations of $\Sigma_e = \sigma_e / \sigma_0$ and Σ_m with normalized distance, r/L^P , in the mode I and mode II direction, Arcan specimen

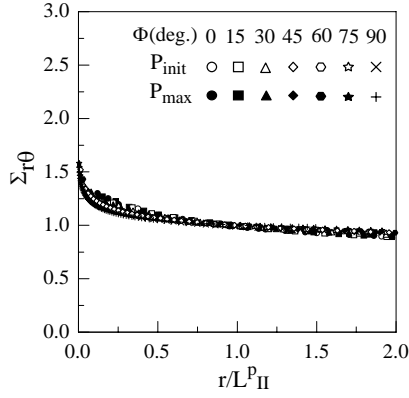


Figure 27(a)

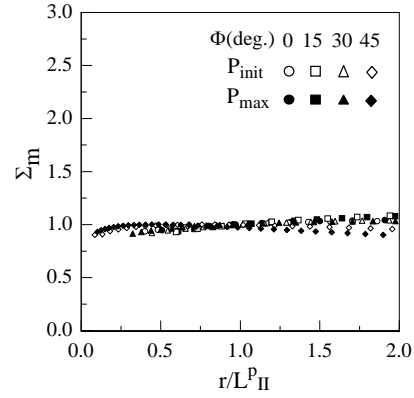
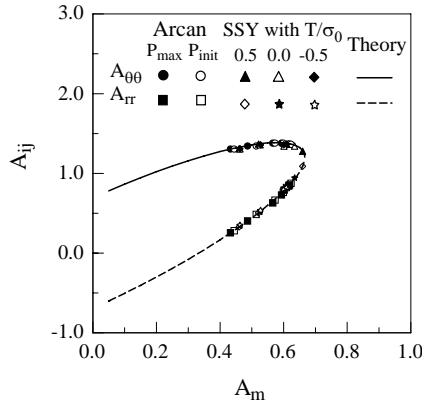
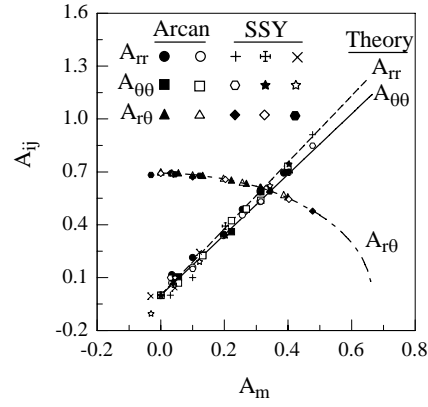


Figure 27(b)

Figure 27: The variation of $\Sigma_{ij} = \sigma_{ij} / (A_{ij} \sigma_0)$ with normalized distance, r/L^P_{II} , in mode II direction, Arcan specimen



(a)
Figure 28(a)



(b)
Figure 28(b)

Figure 28: A_{ij} as function of A_m in (a) mode I and (b) mode II directions, respectively

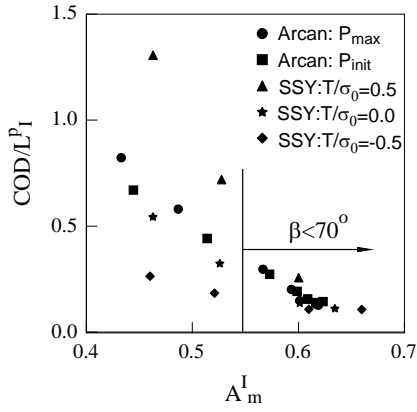


Figure 29(a)

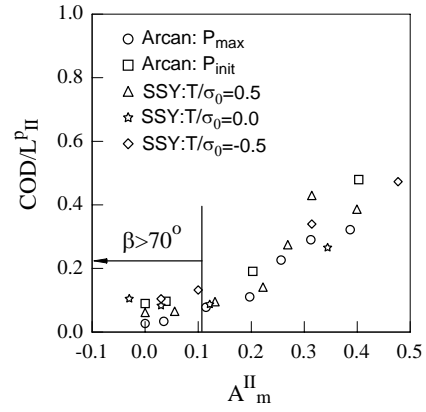


Figure 29(b)

Figure 29: Correlation of COD to A_m and L^P in (a) mode I , and (a) mode II directions, respectively

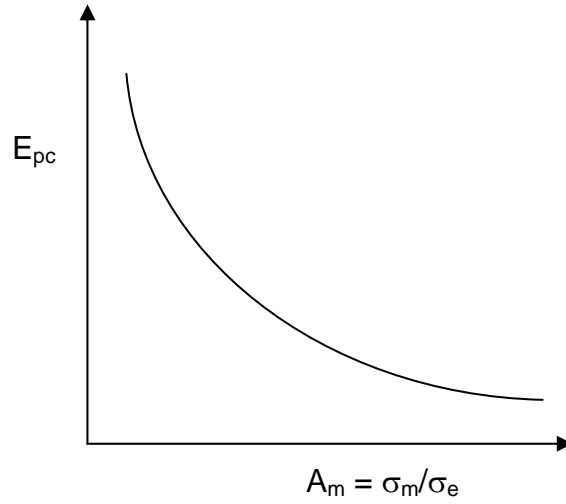


Figure 30: Typical experimentally observed relationship between plastic strain and constraint

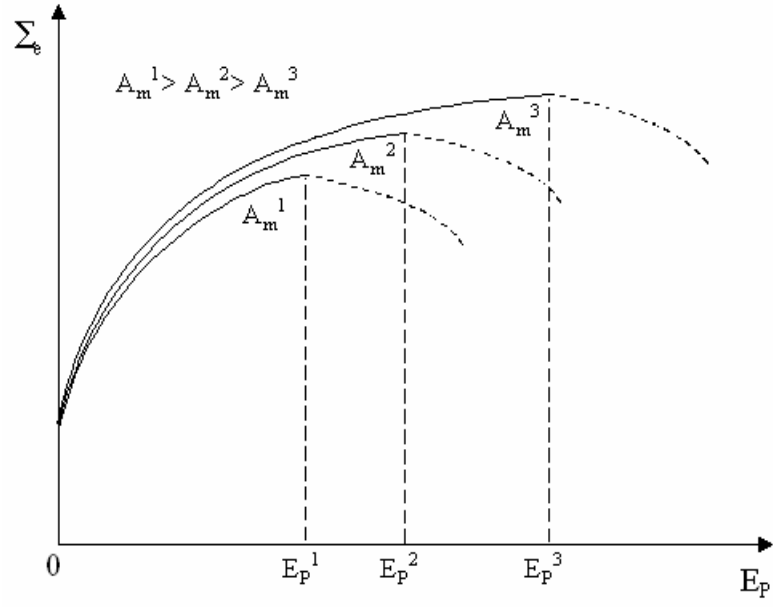


Figure 31: Curves of σ_e versus E_p under different stress constraint levels

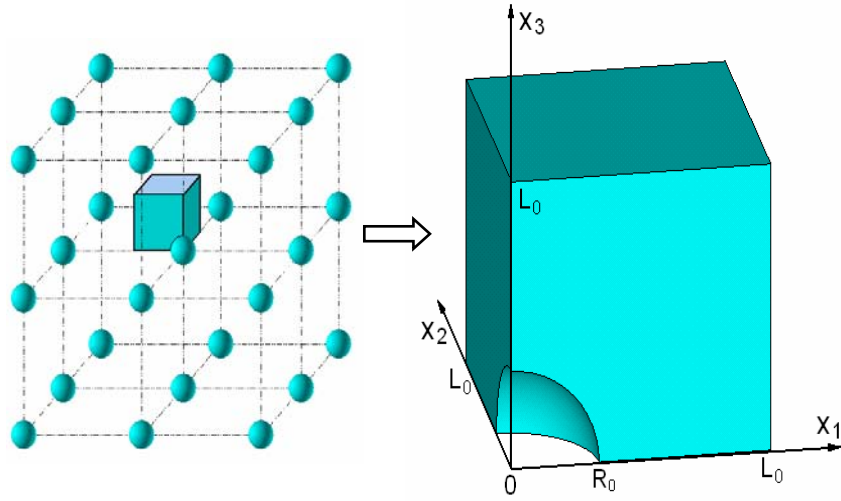


Figure 32: Three-dimensional periodic array of spherical voids and unit cell model

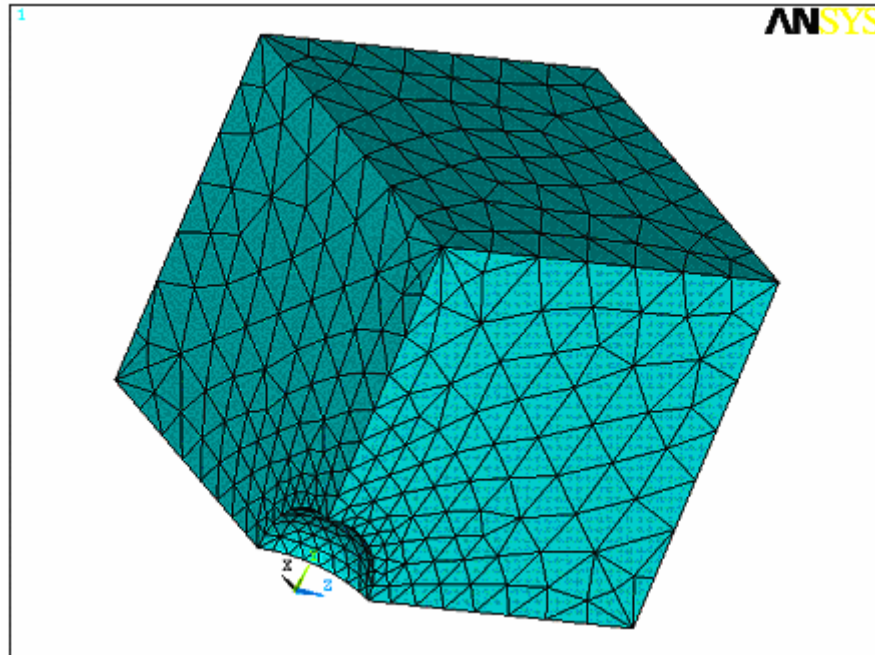


Figure 33: Typical FE mesh for 3D simulations of void region utilizing symmetry boundary conditions

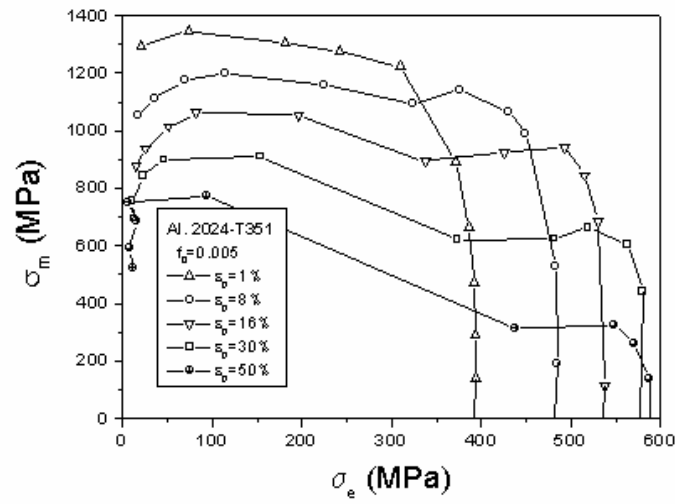


Figure 34(a)

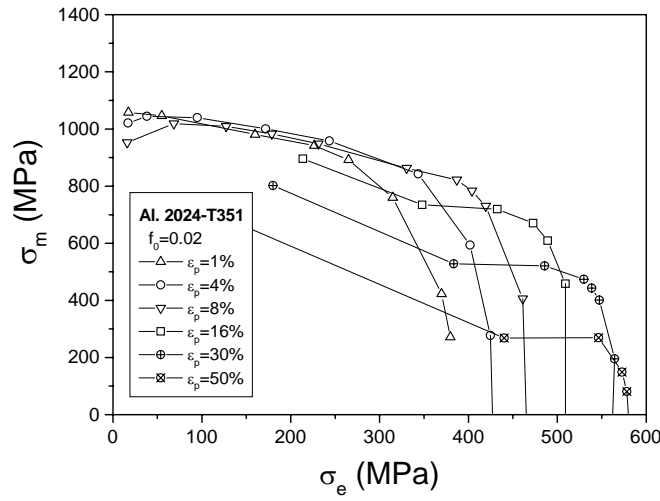


Figure 34(b)

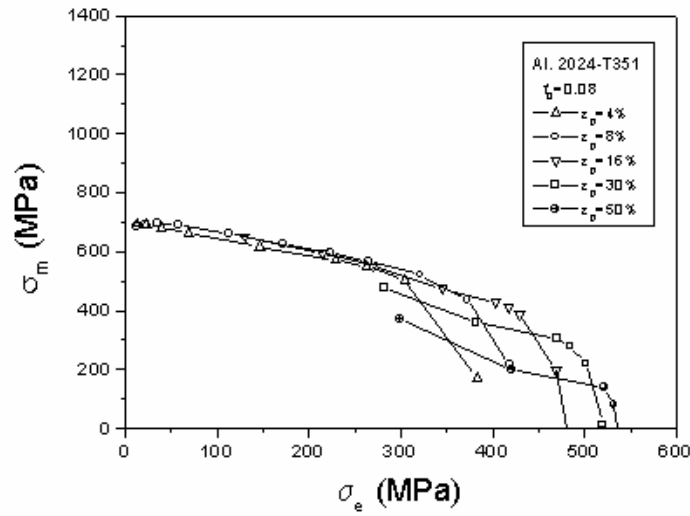


Figure 34(c)

Figure 34: 3D Simulation results at void link-up for $f_0 = 0.005$, 0.020 , and 0.080

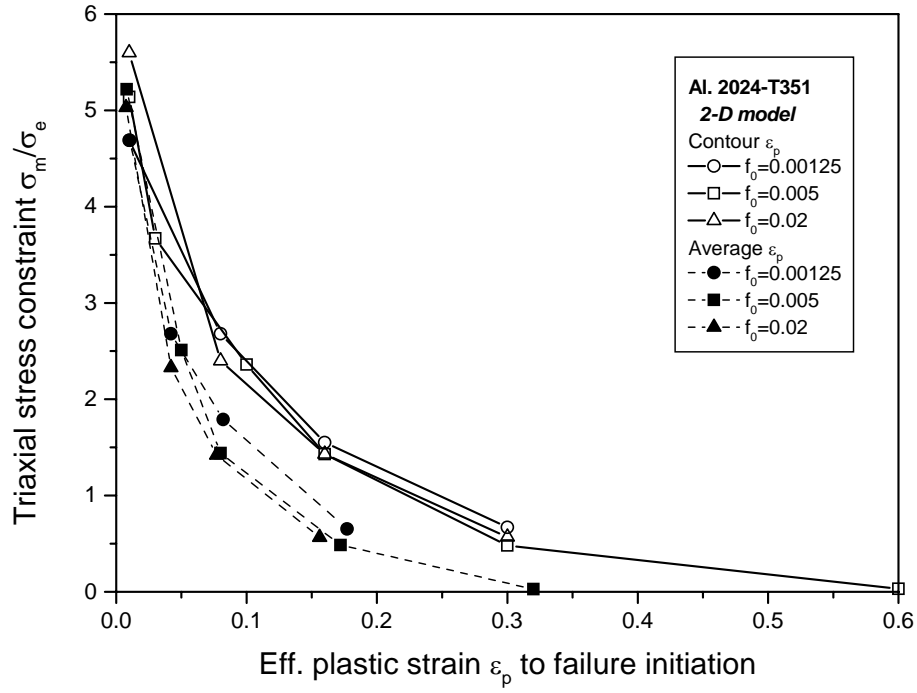


Figure 35: 3D Simulation results for (σ_m, E_p) at void link-up for $f_0 = 0.005, 0.020$, and 0.080

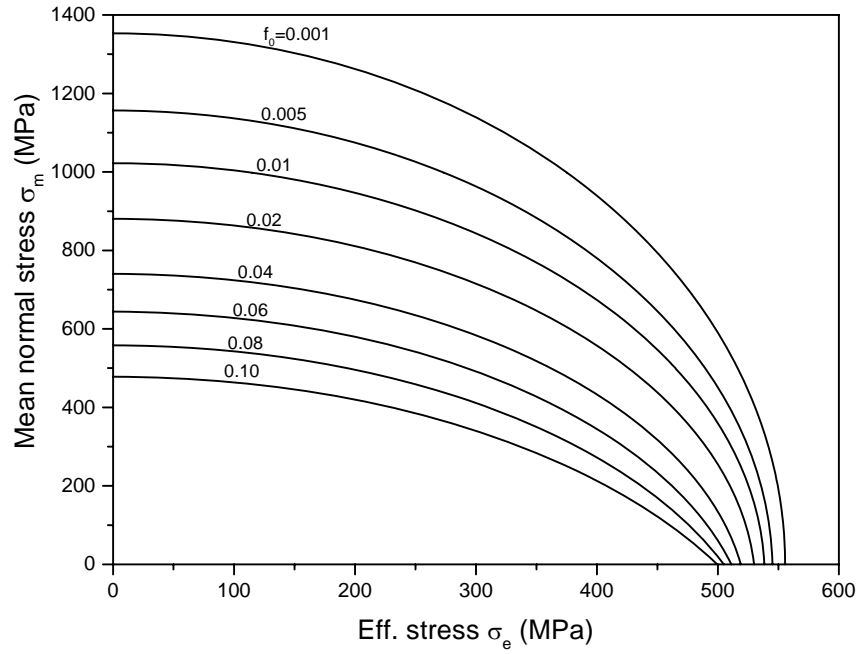


Figure 36: Best fit results for (σ_m, σ_e) at void link-up for $0.001 < f_0 \leq 0.10$

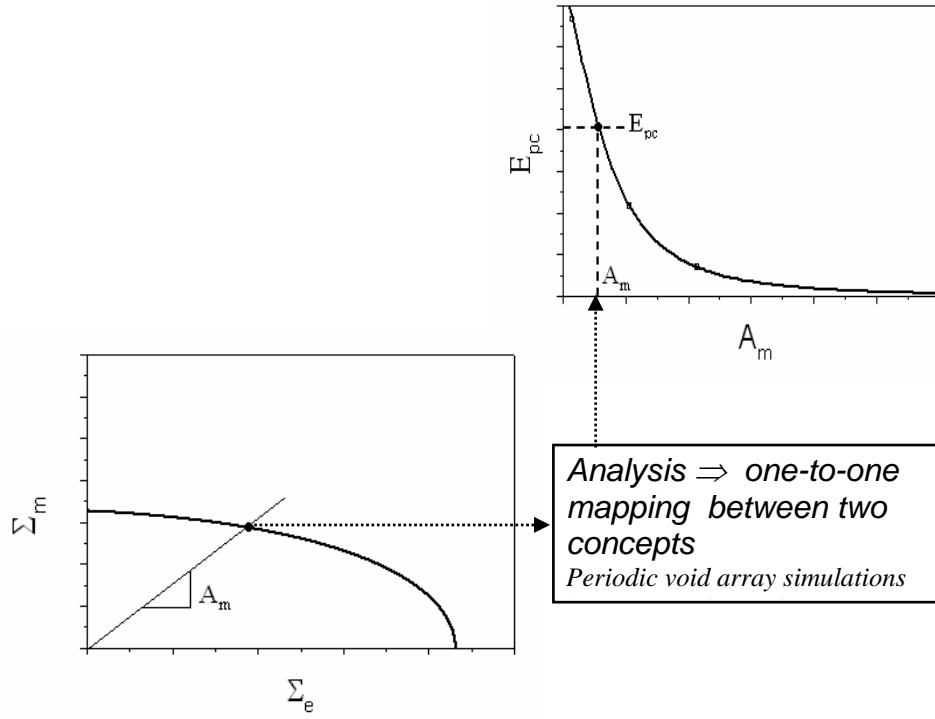


Figure 37: Schematic of relationship between (σ_m, σ_e) and (E_{pc}, A_m) for a given f_0

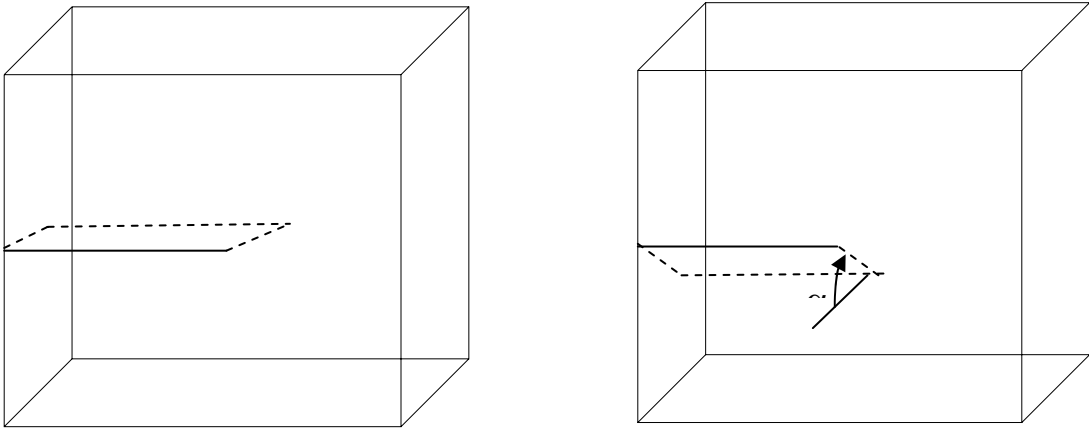


Figure 38: Schematic of flat and slant crack geometries

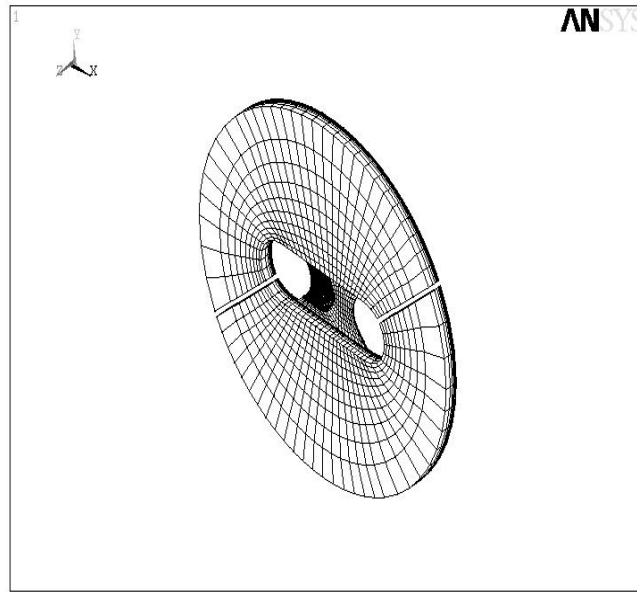


Figure 39(a) Flat Crack Arcan Specimen Mesh

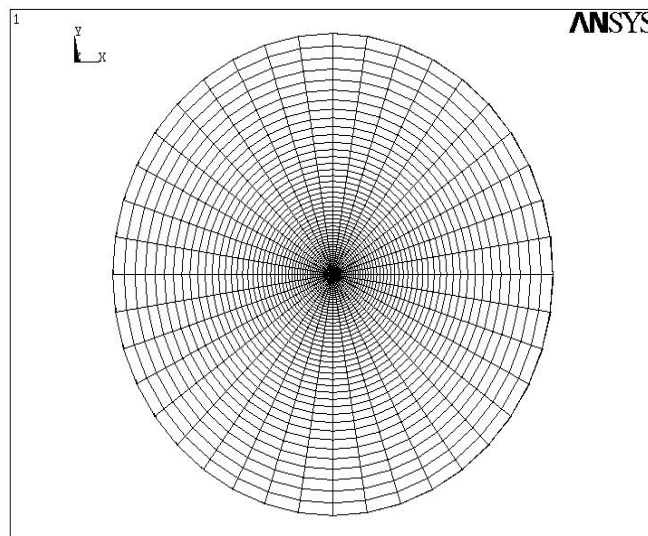


Figure 39(b) Focused Mesh at Crack Tip for Flat Crack

Figure 39: Finite element meshes for the Arcan fixture-specimen system with a flat crack

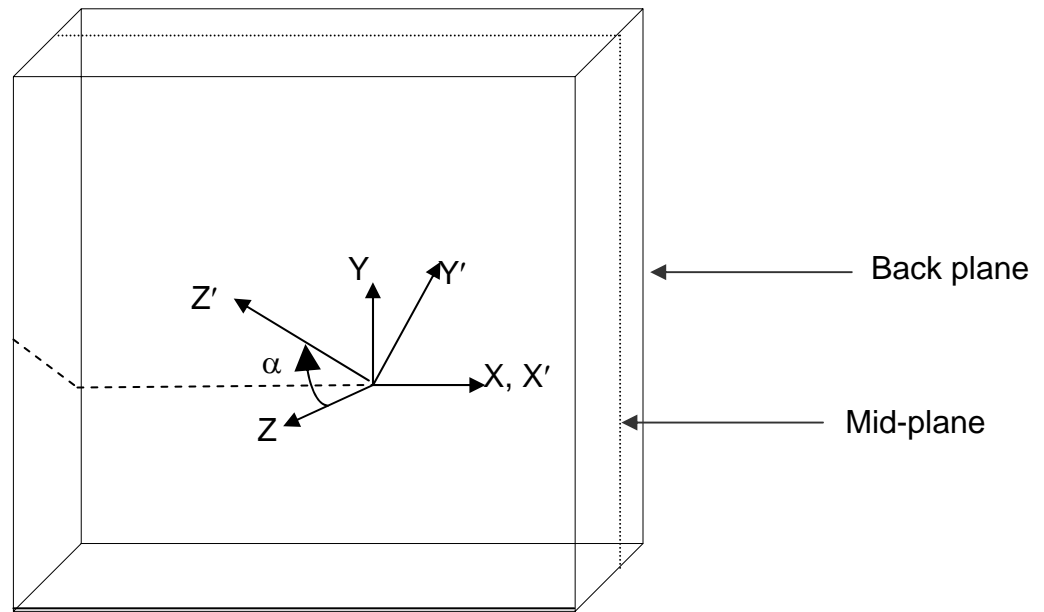


Figure 40: and global coordinate systems for slant crack

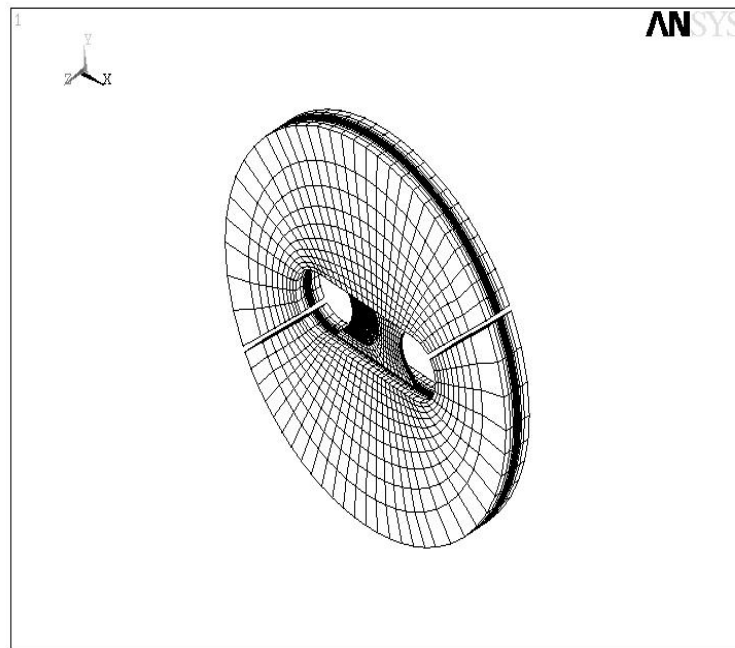
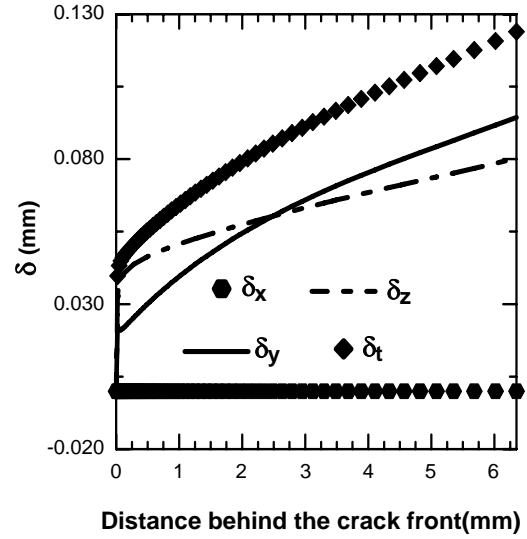
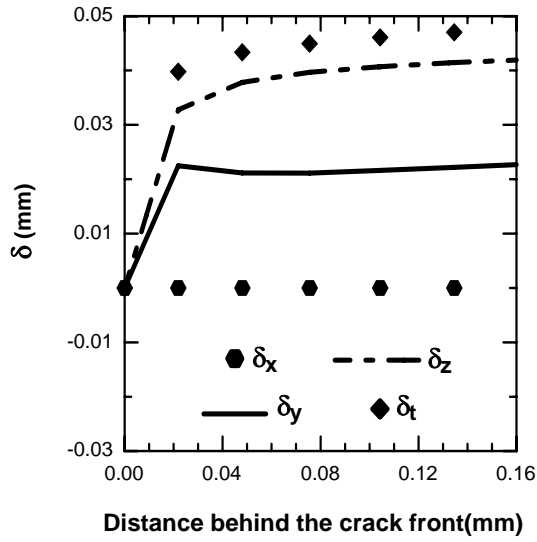
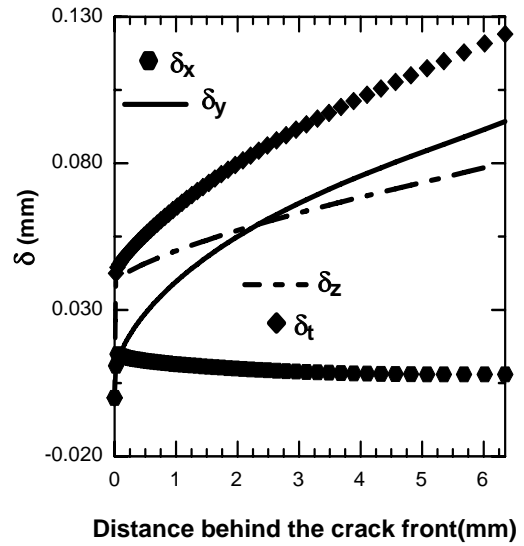
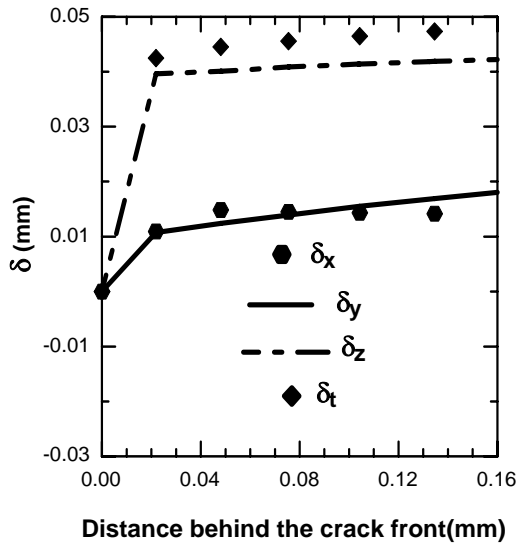


Figure 41: Finite element mesh for the Arcan fixture-specimen with a slant crack



Mid-plane Slant Crack



Front-plane Slant Crack

Figure 42: COD variations at mid-plane and front surfaces for slant crack specimen

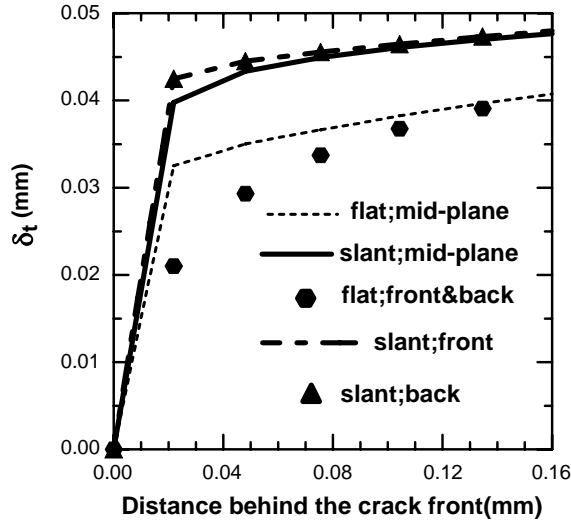


Figure 43(a)

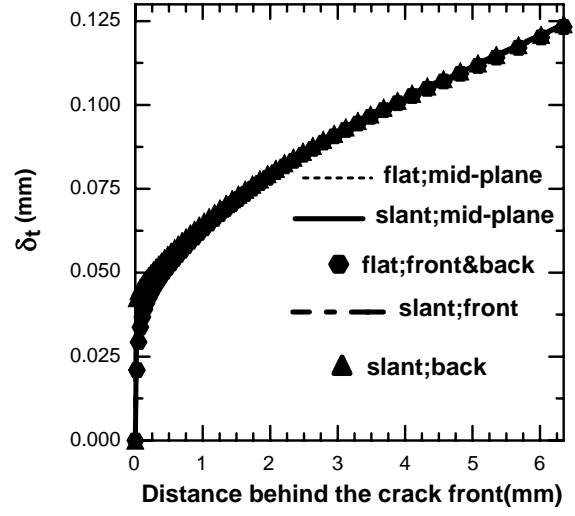


Figure 43(b)

Figure 43: Comparison of total COD for flat and slant cracks

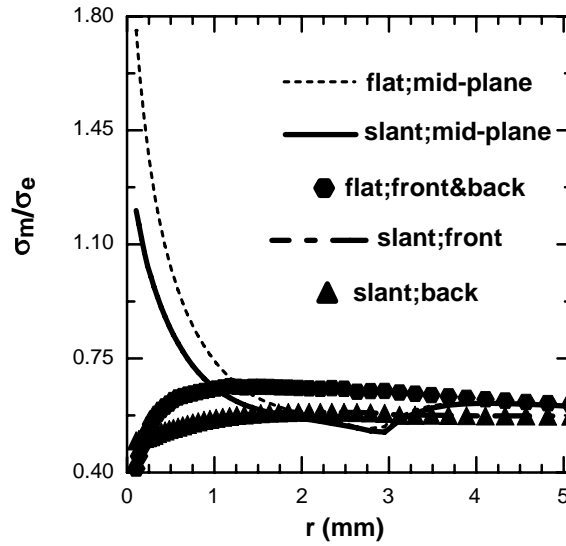


Figure 44: Constraint radial comparison between the flat crack and the slant crack along an angle $\theta = 0^\circ$ with the crack front

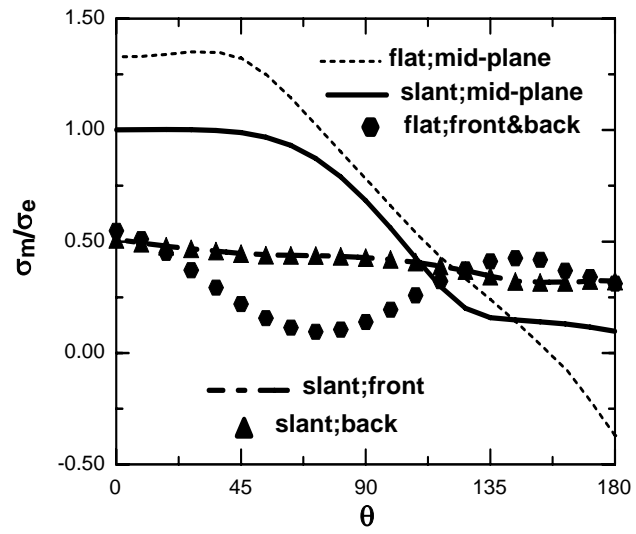


Figure 45: Constraint angular comparison between the flat crack and the slant

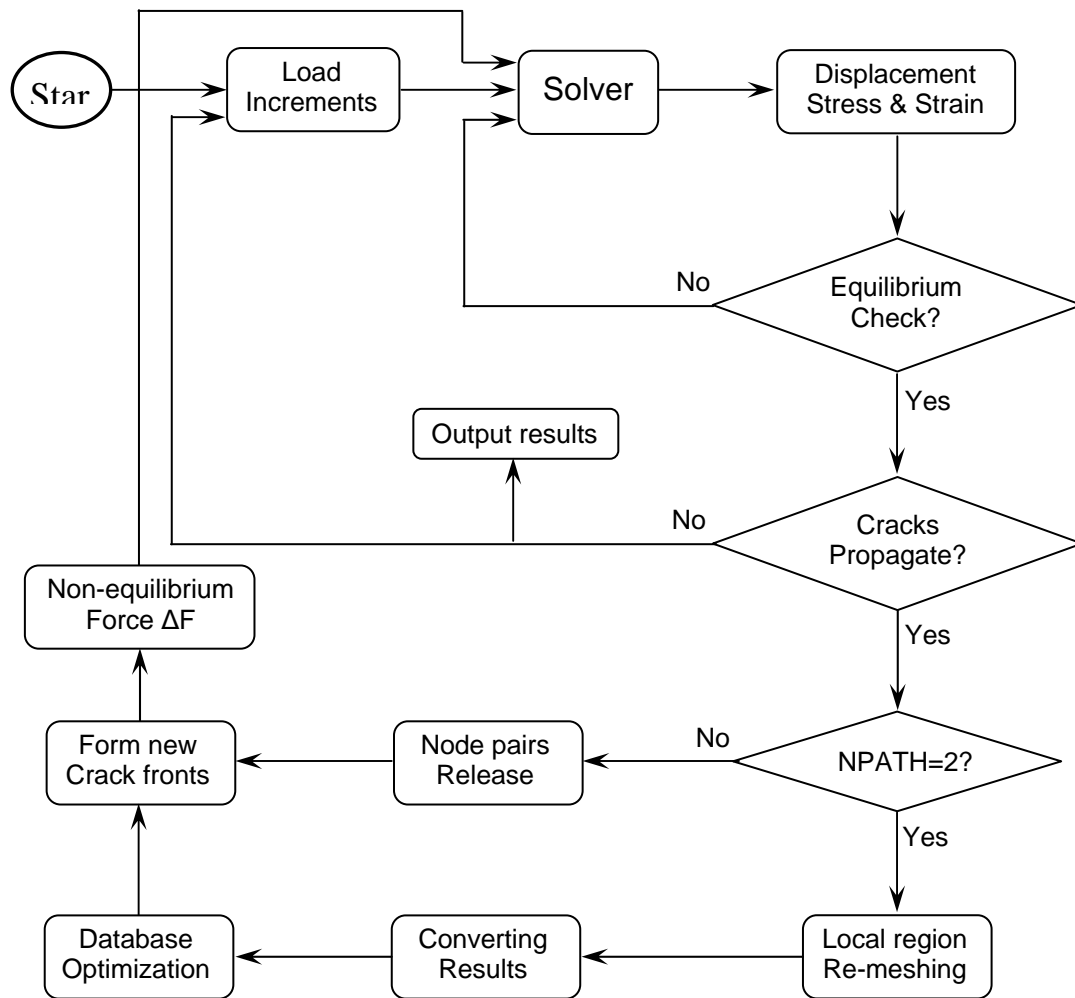


Figure 46: Flow chart for 3D crack growth code, CRACK3D



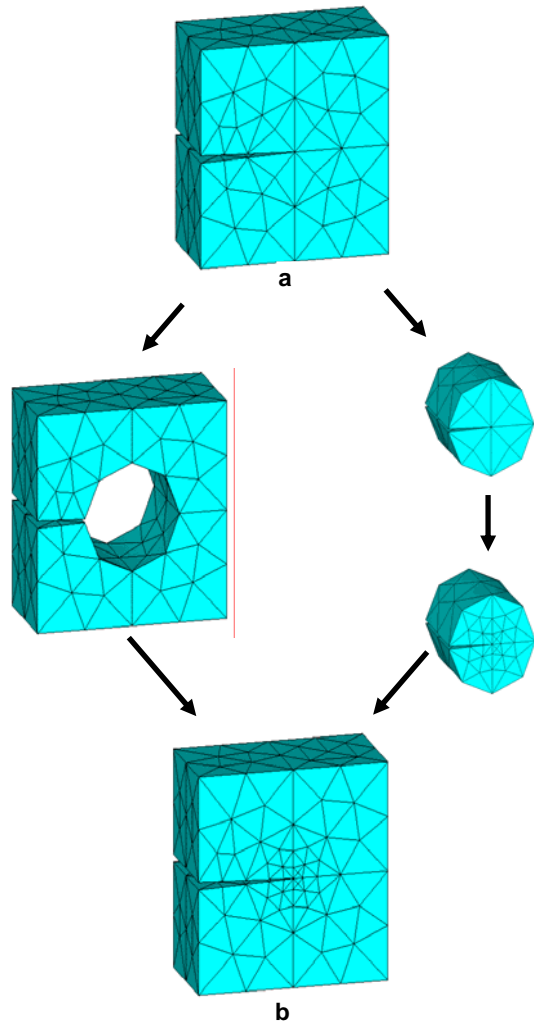


Figure 49: Example of 3D re-meshing results

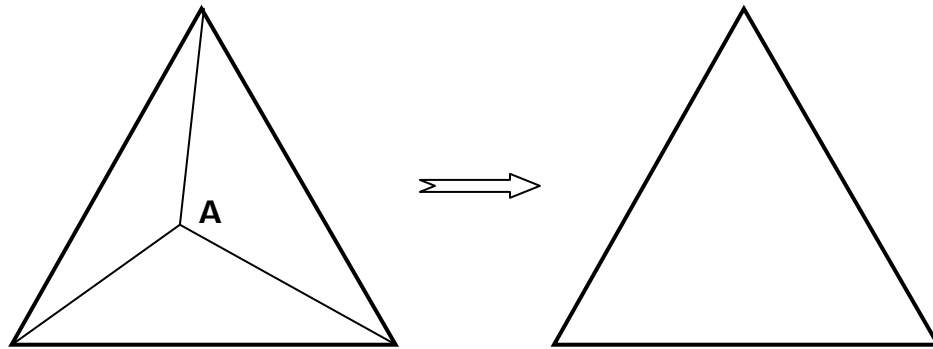


Figure 50: Schematic of nodal points and elements for node identification and element condensation during surface optimization

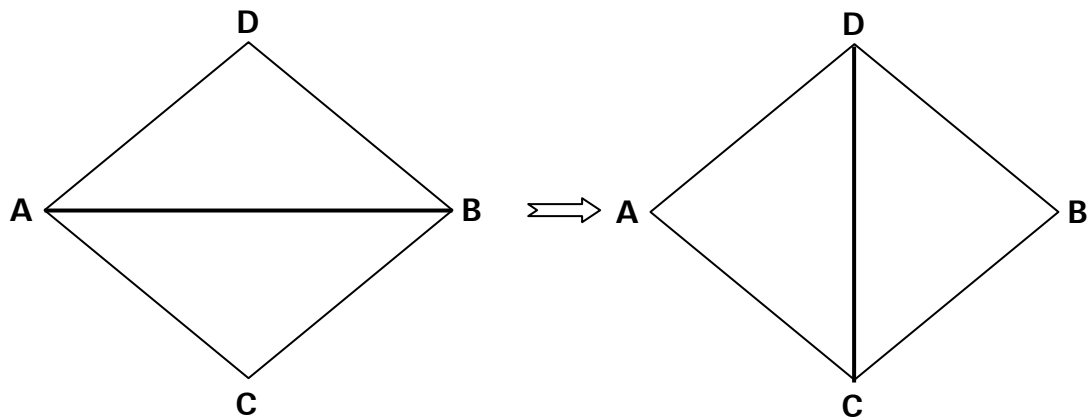


Figure 51: Schematic of lines and elements for line identification and element modification during surface optimization

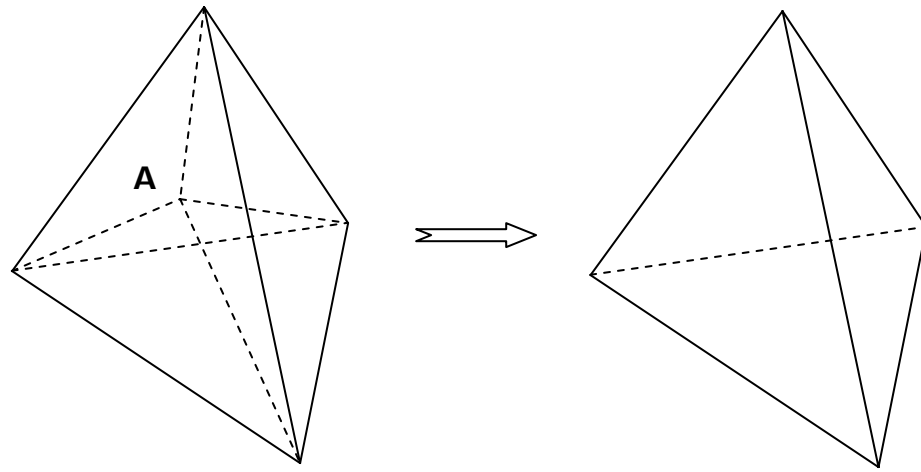
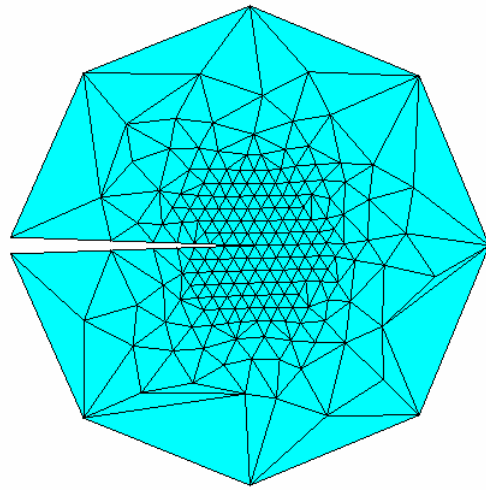
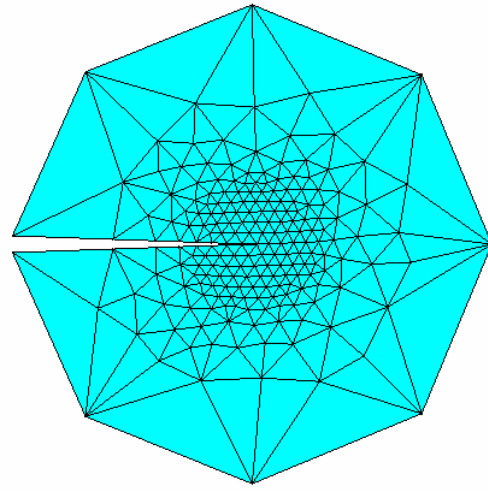


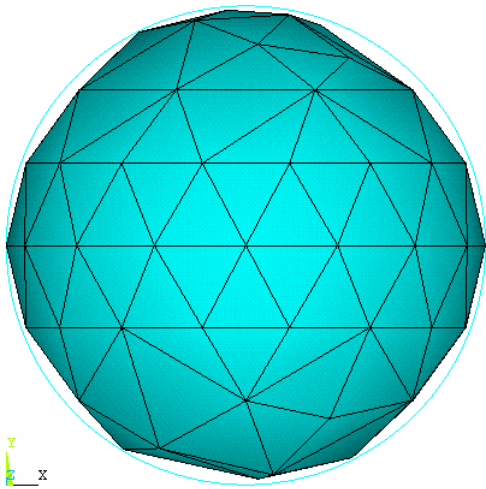
Figure 52: Schematic of nodal points and 3D elements for element condensation during volumetric optimization



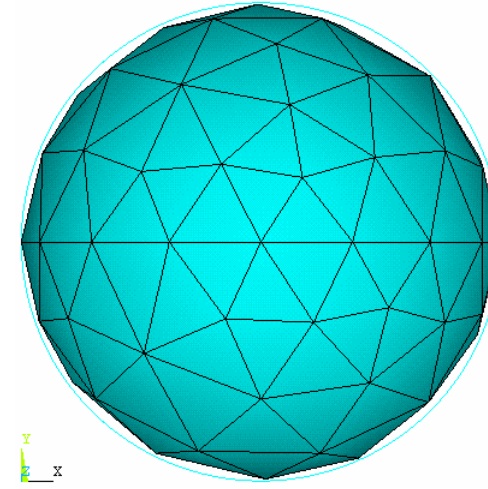
(a) Before optimization



(b) After optimization



(c) Before optimization



(d) After optimization

Figure 53: Comparison of surface and volume meshes before and after mesh optimization

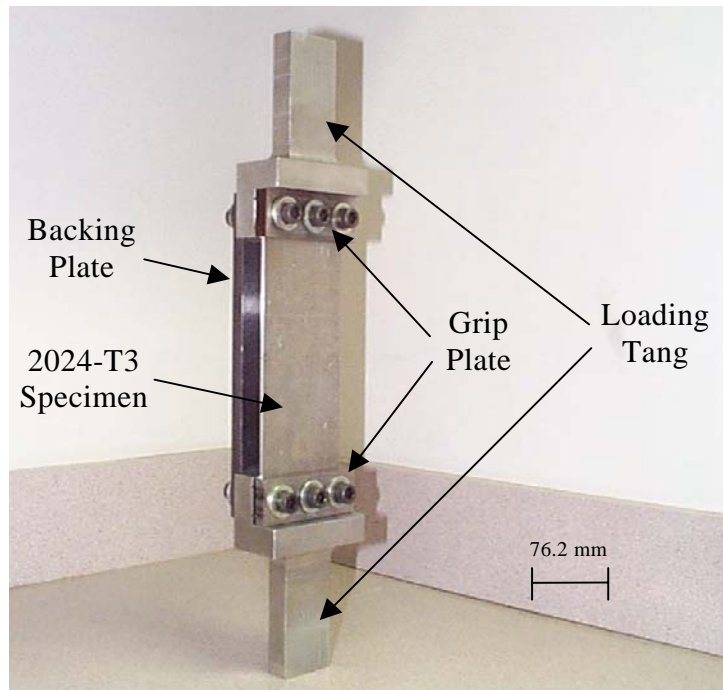


Figure 54(a)

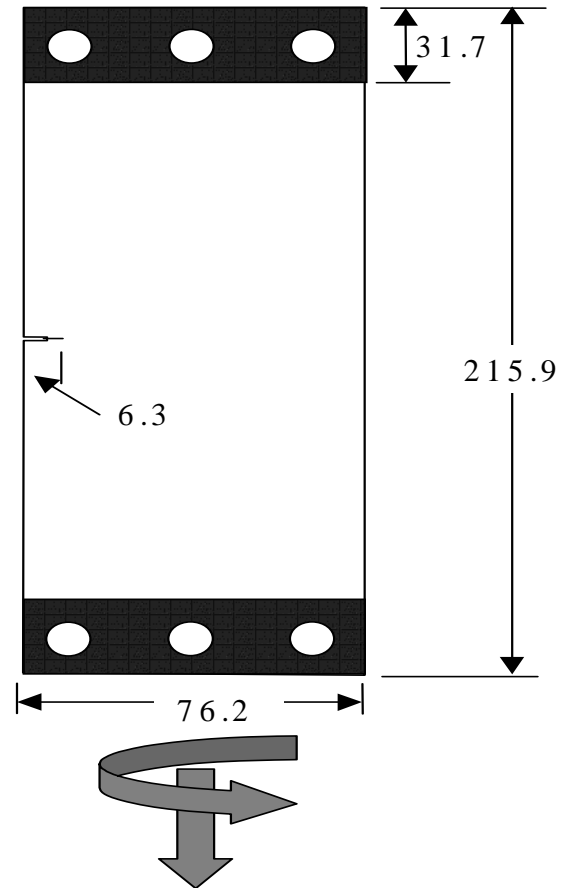


Figure 54(b)

Figure 54: Tension torsion specimen with schematic of loading process

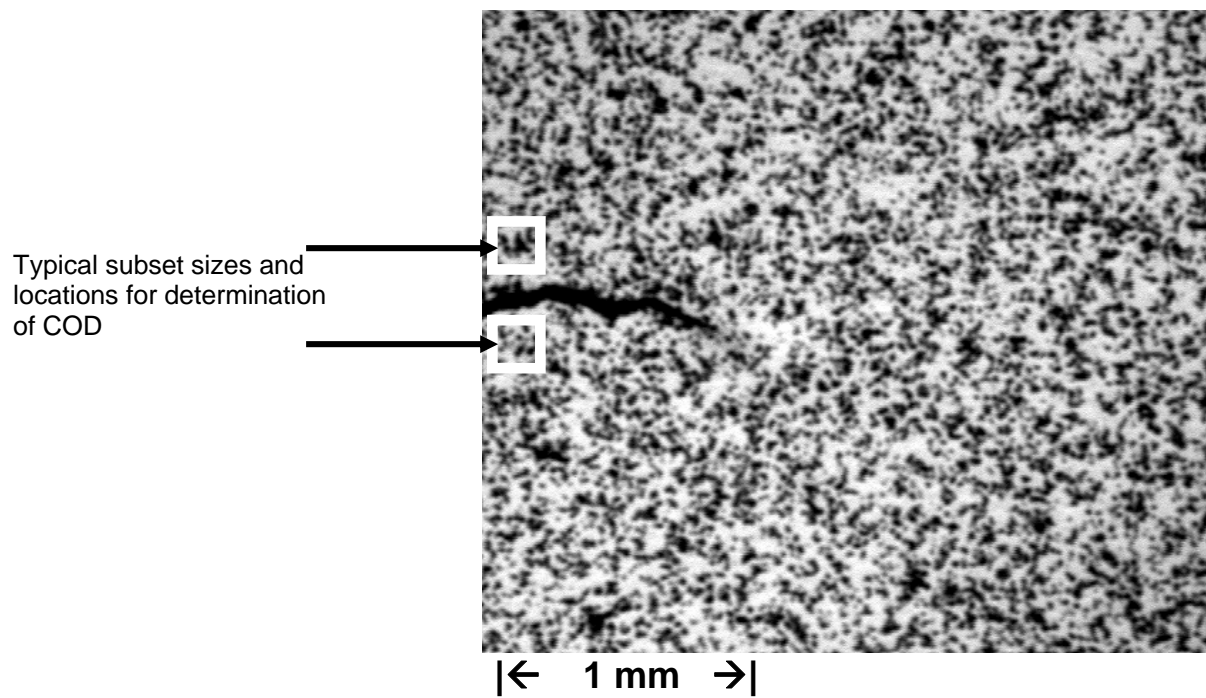
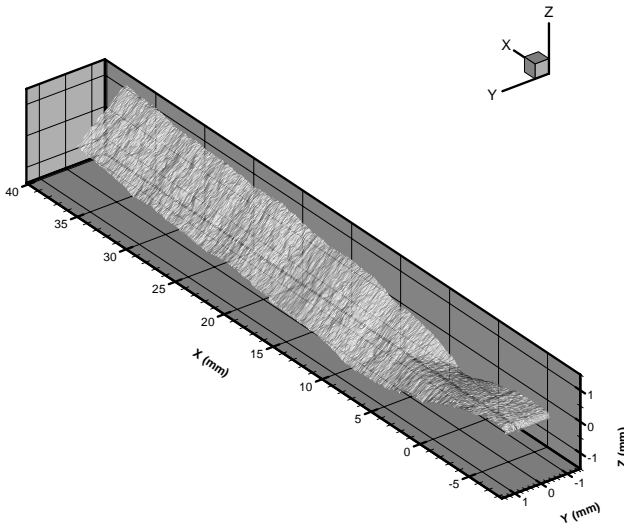
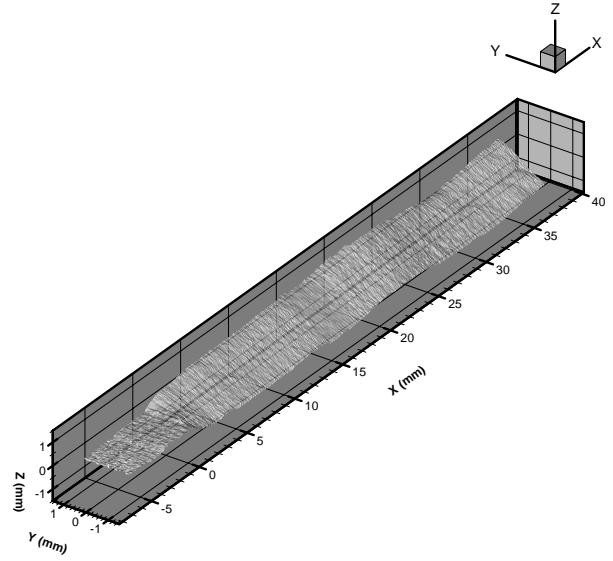


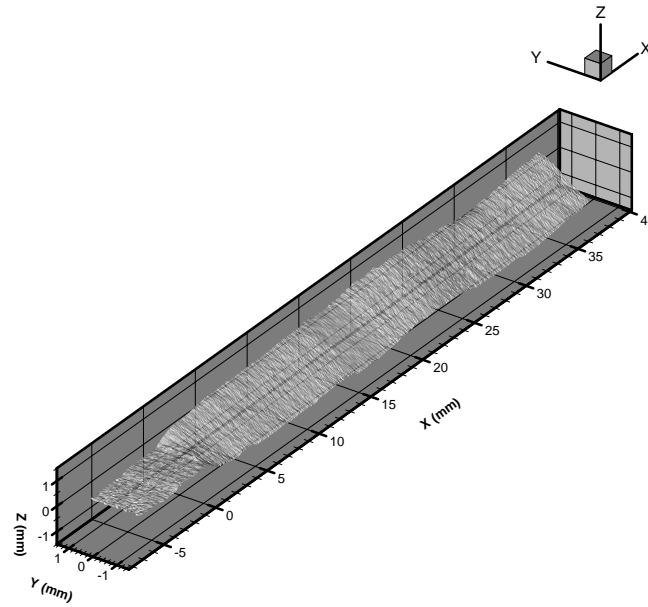
Figure 55: Close-up of crack tip region imaged during crack growth under tension-torsion loading



(a) $S_T/S_P = 0.00$



(b) $S_T/S_P = 1.66$



(c) $S_T/S_P = 6.64$

Figure 56: Profiles of fracture surface of 2024-T3 aluminum specimen for various combinations of tension and torsion loading

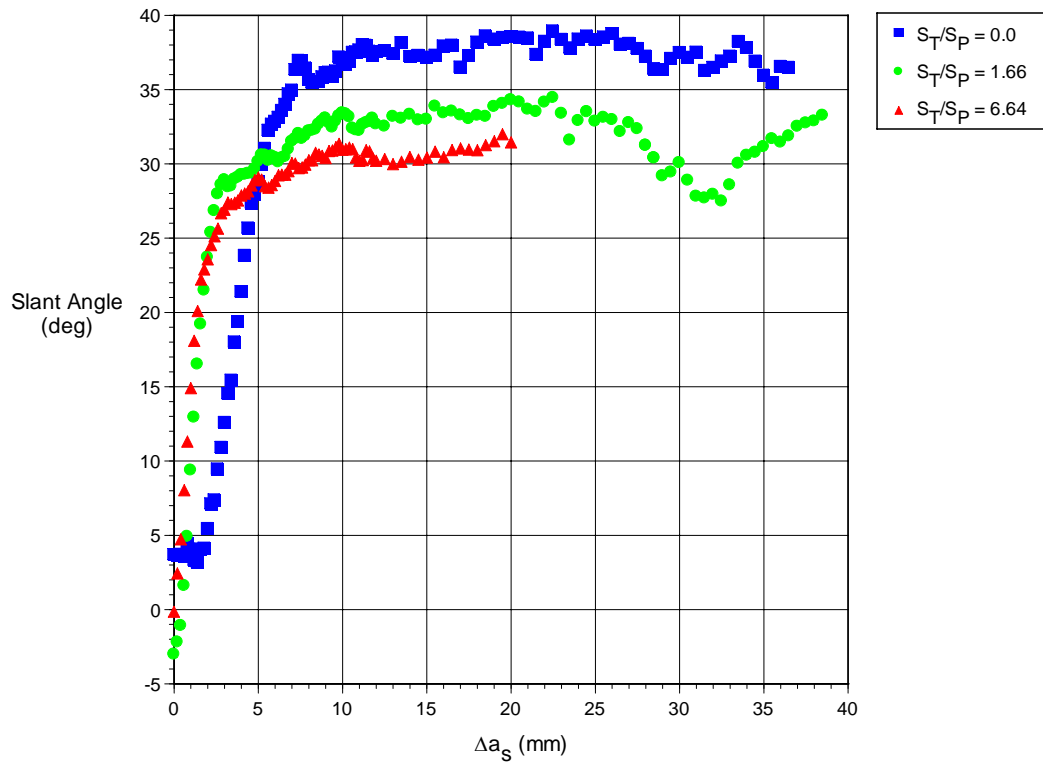


Figure 57: Evolution of slant crack growth angle during tension-torsion loading of 2.3 mm thick, 2024-T3 aluminum specimens

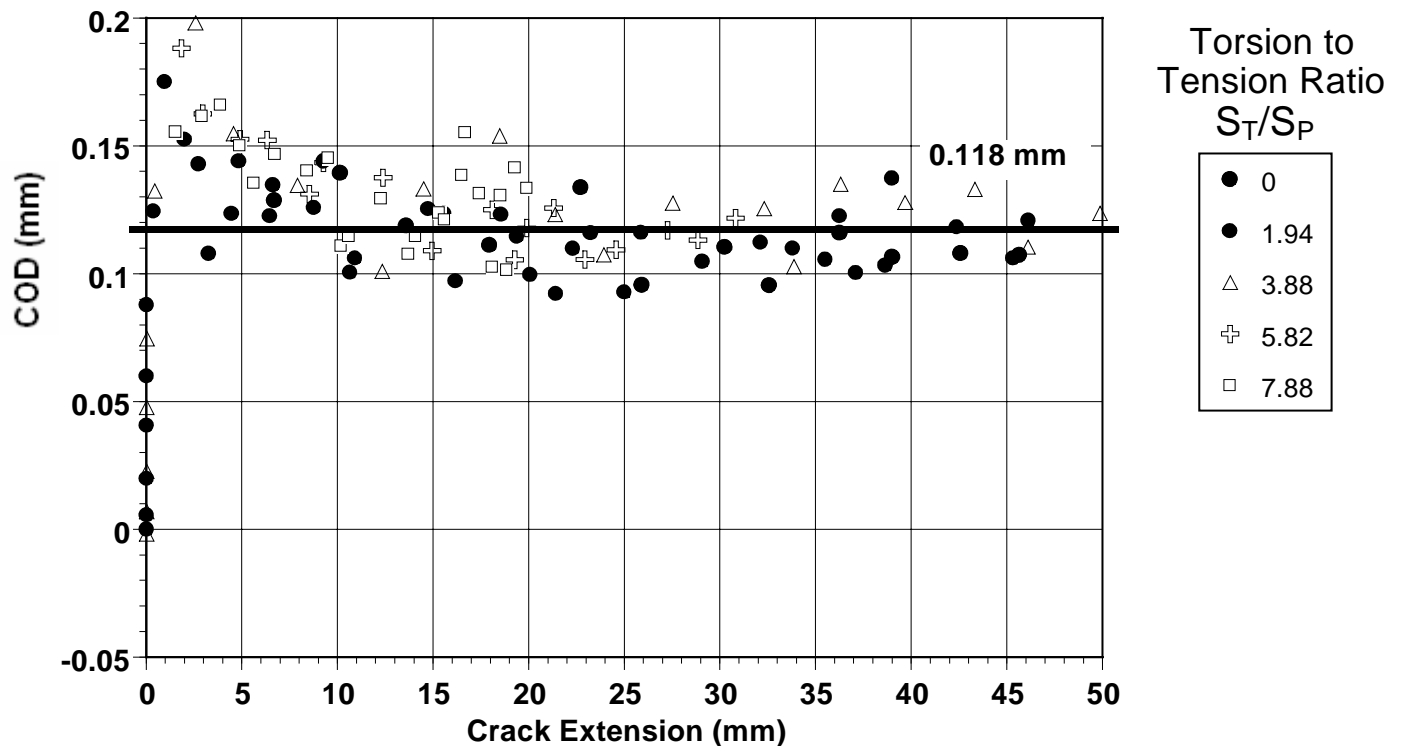


Figure 58: COD versus crack extension for various ratios of torsion and tension

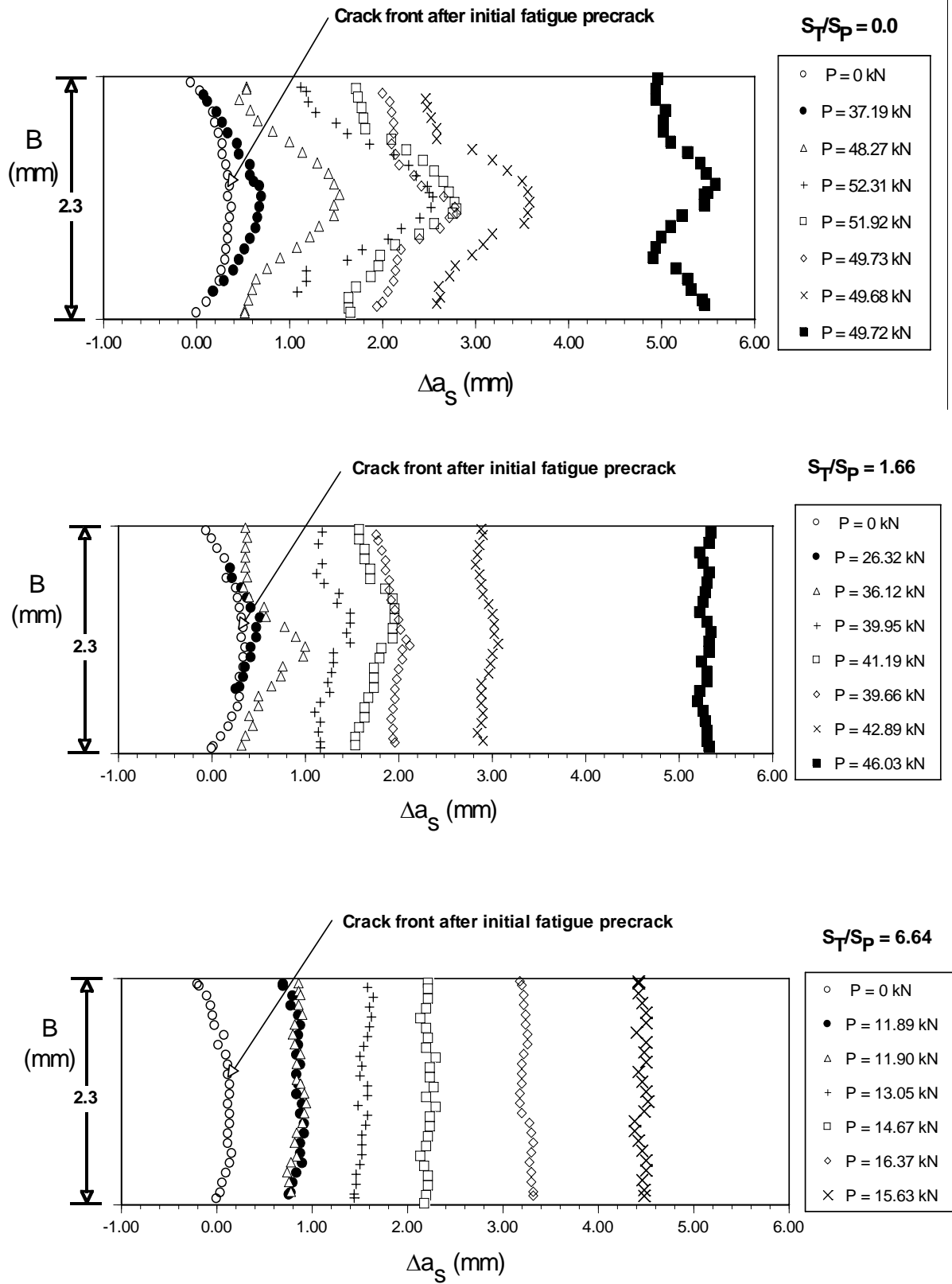


Figure 59: Tunneling during slant crack growth under tension-torsion loading

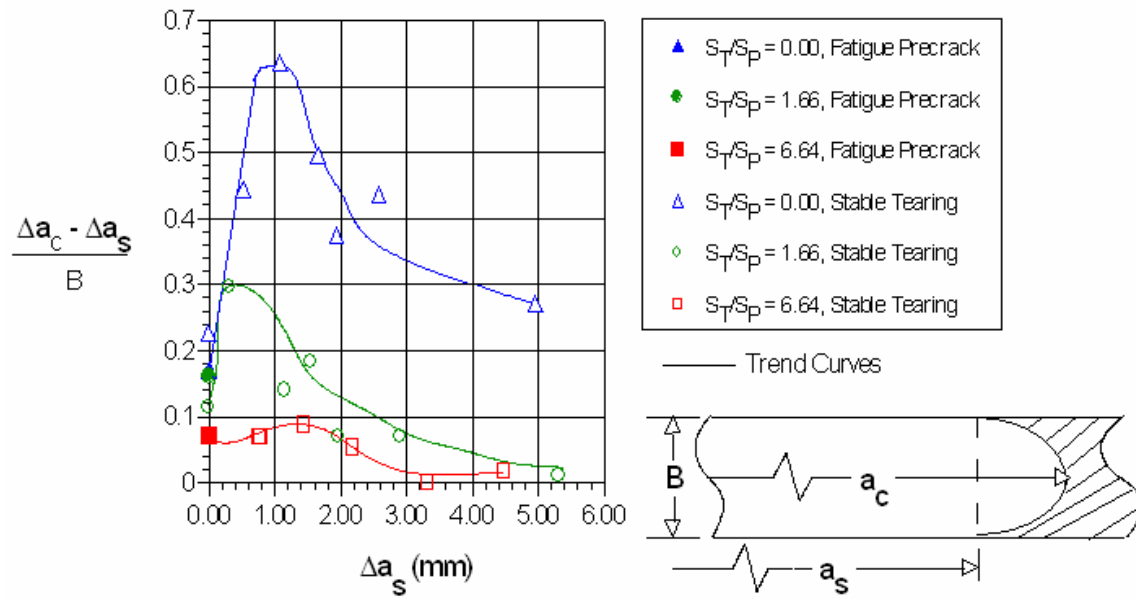


Figure 60: Non-dimensional measure of tunneling during initial stages of crack growth

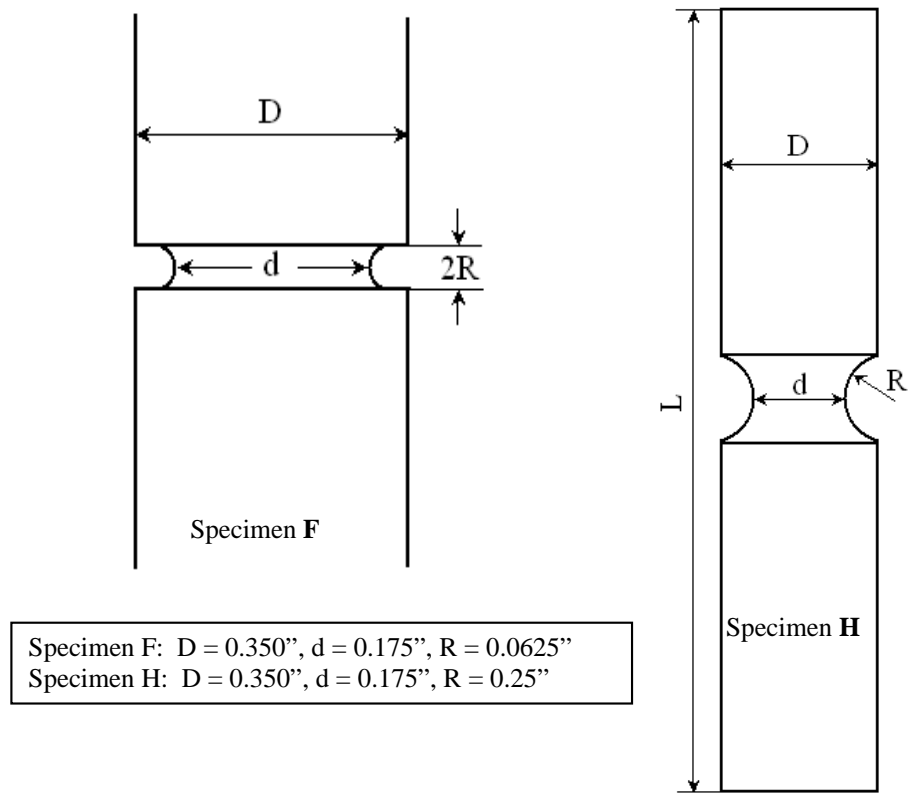


Figure 61: Notched cylindrical specimens (units in inches)

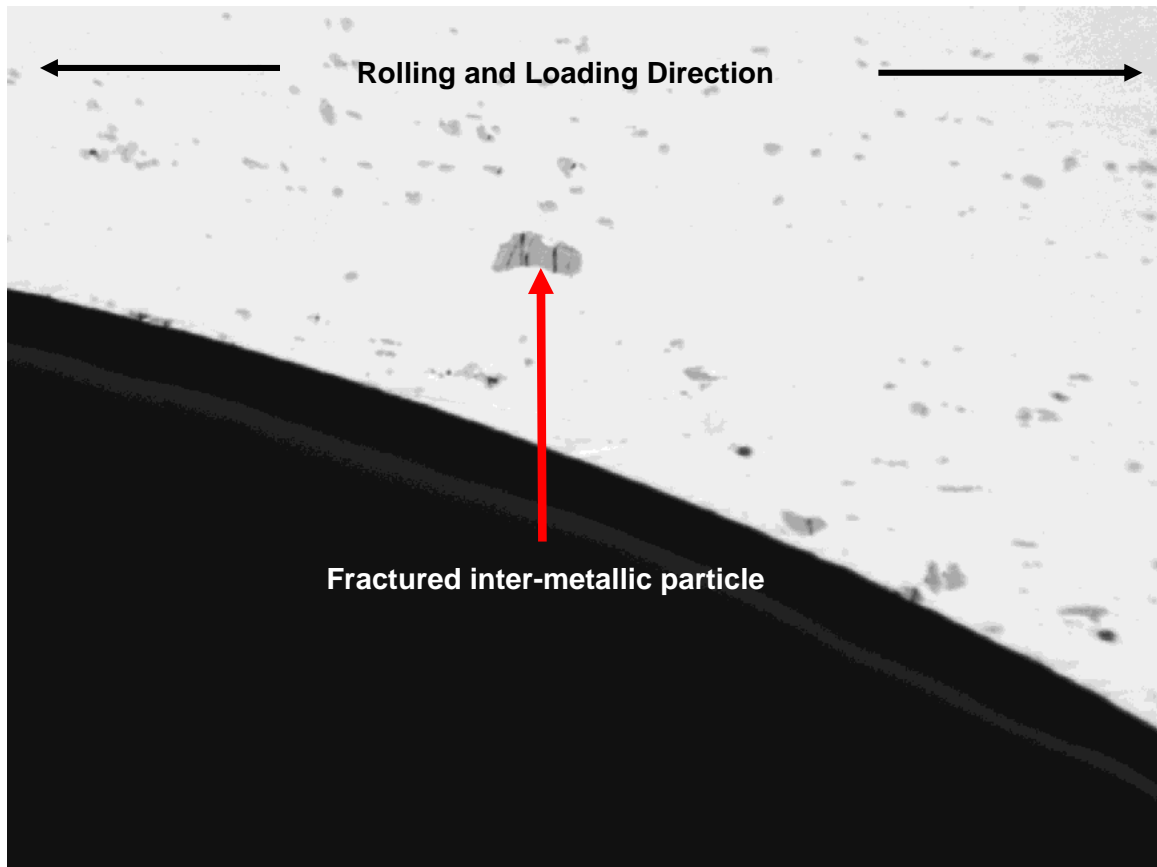


Figure 62: Optical microscope image near notch for specimen F (Light color is aluminum, dark particles are inter-metallic)

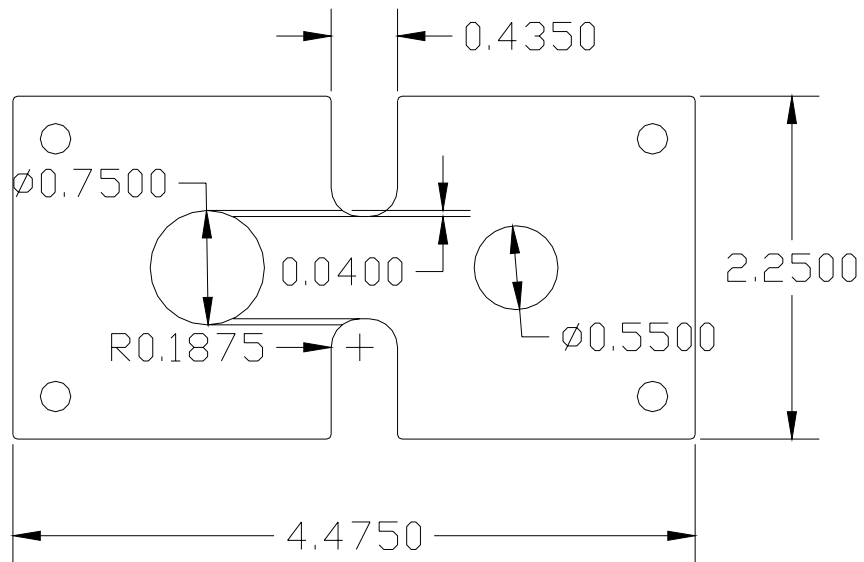


Figure 63: Shear specimen for void-growth studies (units in inches)